

**Effect of Temperature, Oxygen Partial Pressure and Current on the
Kinetics of the Noble-Metal / YSZ Interfacial Exchange Reaction**

by

Sridhar Seetharaman

M.S., Metallurgy and Materials Technology
Royal Institute of Technology, 1994

SUBMITTED TO THE DEPARTMENT OF MATERIALS SCIENCE AND
ENGINEERING IN PARTIAL FULFILLMENT OF THE REQUIREMENT
FOR THE DEGREE OF

DOCTOR OF PHILOSOPHY

AT THE

MASSACHUSETTS INSTITUTE OF TECHNOLOGY

JANUARY 1998

[February, 1998]

Copyright © Massachusetts Institute of Technology 1998

Signature of Author _____

Department of Materials Science and Engineering
January 9, 1998

Certified by _____

Uday B. Pal
John Chipman Associate Professor of
Chemical Processing of Materials
Thesis Supervisor

Accepted by _____

Linn W. Hobbs
John F. Elliott Professor of Materials
Chairman, Departmental Committee on Graduate Students

DEC 24 1997

ARCHIVES

LIBRARIES

Effect of Temperature, Oxygen Partial Pressure and Current on the Kinetics of the Noble-Metal / YSZ Interfacial Exchange Reaction

by

Sridhar Seetharaman

Submitted to the Department of Materials Science and Engineering,
January 9, 1998, in Partial Fulfillment of the Requirements for the
Degree of Doctor of Philosophy in Metallurgy

ABSTRACT

Fast oxygen-transfer kinetics across Pt/(Y₂O₃)_{0.08}(ZrO₂)_{0.92} and Pd/(Y₂O₃)_{0.08}(ZrO₂)_{0.92} interfaces is desired in many solid-state electrochemical devices. This work shows for the first time that the oxygen-transfer process is inhibited by the presence of oxygen-containing species (OCS) at the charge-transfer sites. The OCS constitute various compounds resulting from oxygen reacting with the metal-electrode surface. Their presence under static conditions is determined by the temperature and oxygen partial pressure (*P*O₂). A direct current changes the local oxygen potential and therefore also the stability of the OCS. Thus, under anodic currents, noble metals that are generally assumed to be inert towards oxidation, may form OCS and thereby decrease the exchange-reaction rate.

Near-equilibrium experiments show that at the Pt/(Y₂O₃)_{0.08}(ZrO₂)_{0.92} interface, the charge-transfer reaction obeys a *P*O₂ dependence which is in agreement with the Langmuir adsorption isotherm. In the temperature range 850°C to 1050°C, two parallel reaction paths for oxygen-transfer across Pt/(Y₂O₃)_{0.08}(ZrO₂)_{0.92} interfaces have been identified. One of these paths is slower and involves the participation of oxygen-containing species at the gas/Pt/YSZ interface. The other path involves a fast oxygen transfer at the three-phase boundary (gas/Pt/YSZ) sites that are free of OCS. The concentration of the OCS increases when oxygen is supplied by an anodic current and decreases when oxygen is extracted by a cathodic current. A heat treatment at 1050°C cleans the interface free of the OCS. The results are in conformity with available information in catalysis literature on high-temperature oxygen interaction with Pt.

At the Pd/(Y₂O₃)_{0.08}(ZrO₂)_{0.92} interface, lateral diffusion in the Pd/YSZ two-phase boundary is rate limiting for the oxygen-transfer reaction. The effect of anodic and cathodic currents on the exchange reaction through the formation/depletion of OCS is observable only when PdO is thermodynamically stable. It suggests that, PdO may be a major constituent of the OCS in the Pd/(Y₂O₃)_{0.08}(ZrO₂)_{0.92} interface. The oxygen-transfer reaction is slow in the presence of OCS and a pretreatment to strip the interface of OCS improves the electrode kinetics.

Thesis Supervisor: Uday B. Pal

Title: John Chipman Associate Professor of Chemical Processing of Materials

Table of Contents

Abstract	2
Table of Contents	3
List of Figures	5
List of Tables	10
List of Symbols and Abbreviations	11
Acknowledgments	13
1. Introduction	14
1.1. Background to Solid-State-Electrochemical Cells and their Applications.....	15
1.1.1. Stabilized Zirconia-based Electrolytes.....	16
1.1.2. Solid Oxide Fuel Cells (SOFC).....	18
1.1.3. Potentiometric and Amperometric Sensors.....	20
1.1.4 . Oxygen Pumps.....	23
1.2. The Importance of Studying the Oxygen-Transfer Reaction.....	24
1.3. Objective.....	25
1.4. Layout of the Thesis.....	27
2. The Complexity of the Oxygen-Charge-Transfer Reaction	29
2.1. Two Basic types of Interfaces.....	30
2.2. The Metal/YSZ Interface.....	32
2.2.1. Pt/YSZ.....	33
2.2.2. The Electrical Analogs of Physical and Chemical Processes at YSZ/Metal Interfaces.....	35
2.2.2.1. Charge-Transfer Resistance R_{ct}	38
2.2.2.2. Mass-transport Impedance Z_{mt}	42
2.3. The Effect of Oxygen on Platinum.....	50
2.4. The effect of Oxygen on Palladium.....	54
2.5. Role of Interfacial Oxygen Containing Species in the Oxygen Exchange process at the Metal/YSZ Interface.....	55
3. Experimental Approach and Data Analysis	57
3.1. Experimental Configuration for the study of Electrode reactions.....	58
3.1.1. Electrochemical Impedance Spectroscopy (EIS).....	61
3.1.1.1. The Experimental Procedure for the Study of Interfacial Reactions with EIS.....	63
3.1.1.2. Interpretation of the Impedance Spectra for the Metal/YSZ Interface.....	65
3.1.2. Gas Analysis.....	68
3.2. Experimental Configuration for Study Conducted under Fuel Cell Conditions.....	69
3.2.1. Electrochemical Impedance Spectroscopy.....	72
3.2.2. Current Interruption.....	73
3.2.3. Current vs. Voltage Characteristics.....	75

3.2.4. Gas Analysis.....	75
3.3. Electrode Preparation and Characterization.....	75
3.3.1. Pt-ink Electrodes.....	75
3.3.2. Ni/YSZ Electrodes.....	76
3.3.3. Electrolytes.....	76
4. Ni-YSZ/YSZ/Pt Cell-Steam Reforming Studies.....	77
4.1. Surface Area Characterization of the Ni-YSZ Cermets.....	78
4.2. Internal Steam Reforming and Overall Impedance.....	81
4.3. Cell-Impedance Change after Current Interruption.....	83
5. Platinum-YSZ Interface.....	86
5.1. Near-Equilibrium Conditions.....	86
5.2. Microstructure.....	88
5.3. Effect of Direct Current.....	90
5.3.1. The Time Dependent Behavior after Current Interruption.....	97
5.3.2. Physico-chemical Model.....	99
5.4. Chemical Cleaning.....	102
5.5. Two Different Processes for Oxygen and Charge-Transfer Reactions.....	105
5.5.1. Slow Path through OCS.....	108
5.5.2. Two Parallel Paths.....	114
5.6 Summary of the Results on the Pt/YSZ interface.....	120
6. Palladium-YSZ Interface.....	122
6.1. Steady-State Measurements.....	124
6.1.1. Effect of Oxygen Partial Pressure.....	126
6.1.2. Effect of Temperature.....	134
6.1.3. Reaction Model.....	138
6.1.3.1. Charge Transfer.....	140
6.1.3.2. Mass Transport.....	140
6.1.4. Microstructure.....	143
6.1.5. Oxidation in Air at 650°C.....	147
6.2. Effect of Direct Current.....	153
6.2.1. Effect of Temperature.....	154
6.2.2. Effect of Oxygen Partial Pressure at 700°C.....	156
6.3. Summary of the Results on the Pd/YSZ Interface.....	157
7. Conclusions.....	158
8. Implications for Electrochemical Devices and Future Work.....	161
8.1. Implications.....	161
8.2. Future Work.....	165
Appendix I-II.....	167
References.....	171
Biographical Note.....	175

List of Figures

Figure 1.1. Unit cell for Fluorite structure.....	17
Figure 1.2. Effect of dopant concentration on oxygen-ion conductivity for the ZrO_2 - Y_2O_3 system [Baumard 1984].....	18
Figure 1.3. Schematic diagram of SOFC.....	19
Figure 1.4. Potentiometric oxygen sensor.....	20
Figure 1.5 Amperometric sensor for measuring the limiting current.....	22
Figure 1.6 Limiting current evaluated from the polarization characteristics.....	22
Figure 1.7. Zirconia-based oxygen pump.....	23
Figure 2.1 The triple phase boundary (TPB).....	31
Figure 2.2 Reaction sites for type II interface (In a mixed conducting electrode, the TPB and the entire electrode surface are reaction sites).....	32
Figure 2.3 Schematic of the pathways of oxygen and charge transfer at the Pt/YSZ interfaces.....	34
Figure 2.4 The metal-YSZ Interface.....	36
Figure 2.5 Process wherein adsorption kinetics is rate controlling.....	44
Figure 2.6 Surface diffusion of atomic oxygen adsorbed on metal particle.....	45
Figure 2.7 Mass-transport rate is comparable to charge transfer rate. (a) Pile up at the interface, (b) Interfacial diffusion model by Wang and Nowick [Wang 1979] (dotted region represents the YSZ/metal interface).....	47
Figure 2.8. The two-phase reaction zone.....	48
Figure 2.9. ΔG of formation of PtO_n in 1 atm O_2 vs. T	50
Figure 2.10. ΔG of formation of PtO_x in 1 atm O_2 vs. T	53

Figure 2.11. ΔG of formation of PdO vs. temperature at various P_{O_2} . (calculated from <i>Thermochemical Data of Pure Substances</i>) [Barin 1993])	54
Figure 2.12. OCS formation a) from gaseous oxygen b) oxygen supplied through the electrolyte.....	55
Figure 2.13. The presence of OCS at the TPB.....	56
Figure 3.1. The experimental setup for 3-electrode impedance measurement of a YSZ/electrode interface.....	58
Figure 3.2. The electrode/YSZ/electrode cell.....	59
Figure 3.3. Cross section of the high-temperature cell assembly.....	60
Figure 3.4. The high-temperature cell and the connections of the electrodes to the terminals of the Solartron 1260.....	60
Figure 3.5. Phasor diagram representing the impedance.....	61
Figure 3.6. Link between an electrochemical halfcell and the complex impedance.....	62
Figure 3.7. Typical spectra of the Pt/YSZ interface.....	65
Figure 3.8. The ZARC element.....	67
Figure 3.9. The experimental setup for the laboratory-scale fuel cell.....	69
Figure 3.10. Separated compartments of the fuel cell.....	70
Figure 3.11. Electrode configuration.....	71
Figure 3.12. Electrical circuit for the impedance of the overall cell and leads.....	72
Figure 3.13. Principle of current interruption.....	74
Figure 3.14. Over potential decay after current interruption.....	74
Figure 4.1. Impedance spectra for cells using cermets A,B,D and E.....	82
Figure 4.2. Polarization measurements obtained through current interruption for type A cermet (80 wt. needle).....	83

Figure 4.3. Cell impedance before and after current interruption. 80 wt% spherical Ni grains. T=900°C.....	84
Figure 5.1. $\log R_p$ vs. $\log (P_{O_2})$	87
Figure 5.2. The Pt electrode and the Pt/YSZ interface.....	89
Figure 5.3. Effect of: (a) an anodic current (10 mA) passed for 10 minutes, (b) a cathodic current (10 mA) passed for 10 minutes.....	92
Figure 5.4. Effect of: (a) an anodic current (10 mA) passed for 10 minutes, (b) a cathodic current (10 mA) passed for 10 minutes.....	94
Figure 5.5. The transient behavior: 1. Initial equilibrium spectra 2. Spectrum taken 55 seconds after interruption of anodic current (10 mA/2.5 minutes) 3. New equilibrium after anodic current interruption. Spectra taken 55 seconds after interruption of cathodic current (10 mA/2.5 minutes). Inserts show transient behavior after current interruptions.....	98
Figure 5.6. Current-induced oxygen supply / depletion at the TPB.....	100
Figure 5.7. Impedance spectra before and after CO-CO ₂ gas mixture treatment. The roman numerals indicate the sequence of the spectra taken.....	104
Figure 5.8. Steady-state spectra between 1050°C and 900°C: (a) heating from room temperature, (b) cooling from 1050°C.....	106
Figure 5.9. Equilibration after heating from room temperature.....	107
Figure 5.10. Thermal conditions for current-induced effect; (a) heating from room temperature; (b) cooling from 1050°C.....	108
Figure 5.11. Time-dependent recovery after interruption of different current magnitudes.....	111
Figure 5.12. Rate of OCS equilibration with time.....	112
Figure 5.13. R_p , 55 seconds after current interruption.....	113
Figure 5.14. Physical-two-path model.....	114
Figure 5.15. Evolution of the impedance spectra of the Pt/YSZ interface during heat treatment at 1050°C. (a) total R_p ; (b) the R values from a $R-C$ element and from a distributed element. The last spectra are best fitted with a ZARC only; the $R-C$ element tends to become insignificant.....	117

Figure 5.16. Electrical model of figure 5.14.....	119
Figure 6.1 The Pd/PdO phase diagram and the 5 sets of steady-state measurements (each set represents discrete measurements in a range indicated by the lines and the general direction in which the measurements were made is indicated by the arrows).....	124
Figure 6.2. Representative impedance spectra of the Pd/YSZ interface.....	125
Figure 6.3 Impedance spectra of Pd/YSZ at 900°C under different P_{O_2}	127
Figure 6.4 The dependence of the polarization to $\log(P_{O_2})$ at 900°C.....	128
Figure 6.5. The dependence of the polarization to $\log(P_{O_2})$ at 850°C.....	129
Figure 6.6. The dependence of the polarization to $\log(P_{O_2})$ at 650°C.....	130
Figure 6.7. The time-dependent change in polarization observed above $P_{O_2} > 0.04$ atm at 650°C.	131
Figure 6.8 The time-dependent change in impedance.....	132
Figure 6.9 Impedance spectra of Pd/YSZ at $P_{O_2}=0.02$ atm and 650°C.....	133
Figure 6.10. Electrical models for the two states in figure 6.9: (a) unoxidized (b) oxidized.....	134
Figure 6.11 Spectra for the Pd/YSZ interface at different temperatures in Argon.....	135
Figure 6.12. Temperature dependency of $\ln(R_p)$ under Argon.....	136
Figure 6.13. Temperature dependency of $\ln(R_p)$ under Air.....	137
Figure 6.14 Basic equivalent circuit.....	139
Figure 6.15. Phase angle for arc II in Argon at 900°C.....	141
Figure 6.16. Simulated spectrum using equation 2.28 vs. real spectrum.....	142
Figure 6.17. Top view of the open porosity.....	144
Figure 6.18. Cross section of the Pd/YSZ interface, X 15000.....	145
Figure 6.19. Comparison of TPB lengths between: (a) a wetting grain and a (b) non-wetting grain.....	146

Figure 6.20. Polarization change with time after subjecting the electrode to air at 650°C.....	147
Figure 6.21. Thermogravimetric data of Pd in air at 650°C. Solid line shows weight change with time and dashed line shows rate of weight change with time.....	148
Figure 6.22. Pd coating subjected to air at 650°C for 1 hour.....	151
Figure 6.23. Pd coating subjected to air at 650°C for 24 hours.....	152
Figure 6.24. Effect of an anodic current of 10 mA passed for 5 minutes on the impedance spectra of the Pd/YSZ interface in air. (a) 850°C (b) 800°C.....	155
Figure 6.25. Effect of an anodic current of 10 mA passed for 5 minutes on the impedance spectra of the Pd/YSZ interface.....	156
Figure 8.1 NiO formation near at the Ni/YSZ interface within the dotted region.....	162
Figure 8.2. Exchange reaction at the LMN electrode (a) near-equilibrium conditions (b) dynamic (cathodic) conditions.....	163
Figure A1. The viscosity and powder/liquid ratio region were final cermet structure was optimized with respect to the electrolyte coverage and adherence.....	167
Figure A2. The temperature-dependency of R_p for the Pt/YSZ interface.....	170

List of Tables

Table 2.1 Reaction schemes for oxygen transfer (a)-(b) : No charged intermediates. (c)-(f) : Charged intermediates are formed.....	41-42
Table 3.1. Conditions for time-domain measurements.....	64
Table 3.2 Conditions for measurements in the current-control mode under dc bias.....	65
Table 4.1. Ni-YSZ cermet samples.....	78
Table 4.2. Results of surface area measurements.....	79
Table 4.2 Results of gas composition analysis of the outlet gas at 900°C when the inlet gas had a CH ₄ /H ₂ O ratio of 1/4.....	81
Table 5.1. Summary of near-equilibrium-impedance measurements of the Pt/YSZ interface.....	88
Table 5.2. Characteristics of the steady-state spectra established after current interruption.....	95
Table 5.3. Values for the CPE fitted to the spectra in figure 5.14b.....	118
Table 6.1 Resistive elements.....	138
Table 6.2 Capacitive elements.....	138

List of Symbols and Abbreviations

symbol	units	description
σ	$\text{ohm}^{-1}\text{m}^{-1}$	electrical conductivity
m	$\text{m s}^{-1}\text{N}^{-1}$	mobility of a species (velocity per unit force)
e	C	unit charge of an electron $1.6 \cdot 10^{-19}$ C
P_{O_2}	atm	oxygen partial pressure
$\mu^{(i)}$	J	chemical potential of component i
n	-	number of electrons transferred
I_0	A	exchange current
A	m^2	Generally a geometric area of the electrode but in the case of metal/YSZ systems it is not well defined. It is related to the length of the triple phase boundary line between metal/YSZ/gas
T	$^{\circ}\text{C}$ or K	temperature
C	F	capacitance
C_{dl}	F	The capacitance of the double layer at the metal/YSZ interface
i_f	A	faradaic current
Z_f	ohm	Impedance associated with the faradaic current i_f .
V	V	potential
θ	-	Fraction of a surface covered with a species. ($1 \geq \theta$).
θ_{eq}	-	The equilibrium coverage under zero or low current flow.
R_{ct}	ohm	The charge-transfer resistance associated with oxygen transfer.
$\alpha_{a,c}$	-	transference number
F	C eq.^{-1}	faradays constant, = 96487
R	$\text{J K}^{-1}\text{mol}^{-1}$	gas constant, =8.314
η	V	overpotential
K_i	varies	Equilibrium constant associated with reaction i .
ΔH_{ads}	J	The heat of adsorption which is negative of the enthalpy for the adsorption reaction.
Q	J mole^{-1}	Apparent (measured) activation energy.
E_r	J mole^{-1}	Activation energy associated with charge transfer.
Z_m	ohm	Impedance associated with mass transfer (supply or removal of oxygen to/from the charge-transfer reaction sites).
k_i	$[\text{conc.}]^{1-n} \text{s}^{-1}$	Rate constant for reaction i .
Γ	-	Oxygen activity when fraction of adsorbed oxygen equals unity.
ω	rad s^{-1}	angular velocity ($2\pi f$)
δ	m	surface-diffusion distance
R_{D0}	ohm	Real part of diffusion impedance.
L	m	Width of metal/YSZ contacts (rectangle).
ΔG	J mole^{-1}	Gibbs free energy
f	Hz	frequency
E_{cell}	V	cell potential (open-circuit potential minus ohmic drops and overpotentials)
E_{OCV}	V	open-circuit potential

S_t	m^2	total surface area (measured through BET)
S_c	$\text{m}^2 \text{kg}^{-1}$	specific surface area (measured through BET)
N	-	Avogadro's number ($6.023 \cdot 10^{23}$)
A_{CS}	m^2	Area occupied by adsorbed N_2 molecule.
M	g mole^{-1}	molar mass
P	atm	In the case of BET analysis: partial pressure of adsorbate.
P_o	atm	In the case of BET analysis: saturated pressure of adsorbate.
A_{cal}	m^2	Calibrated integrator count.
V_{cal}	m^3	Calibrated integrator.
P_a	atm	In the case of BET analysis: ambient pressure = 1
D	$\text{cm}^2 \text{s}^{-1}$	diffusion constant

abbreviation	explanation
OCS	Oxygen-Containing Species
EIS	Electrochemical Impedance Spectroscopy
RE	Reference Electrode
CE	Counter Electrode
WE	Working Electrode
TPB	Triple Phase Boundary (between metal, YSZ and gas)
XPS	X-ray Photoelectron Spectroscopy
SEM	Scanning-Electron Microscope
LEEDS	Low-Energy-Electron Diffraction
TG	Thermogravimetry
CSZ	Calcium-Stabilized Zirconia, $(\text{CaO})_x(\text{ZrO}_2)_{1-x}$
YSZ	Yttria-Stabilized Zirconia [in this thesis it represents the following composition: $(\text{Y}_2\text{O}_3)_{0.08}(\text{ZrO}_2)_{0.92}$]
LMN	Doped Lanthanum Manganate LnMnO_3

Acknowledgments

The author wishes to express his sincere appreciation to the following people for helping me during the course of this work:

To my thesis advisor, Professor Uday B. Pal for his excellent guidance, patience and constant encouragement.

To Dr. Victor Stancovski for sharing his scientific experience with me and with whom I have enjoyed many discussions on a countless number of subjects.

To Professor Donald R. Sadoway, a member of my thesis committee, whose contributions to electrochemistry have been and always will be a great inspiration to me. Thanks are also due, for his help in improving the quality of my thesis.

To Professor Chris E. Scott whom I greatly enjoyed interacting with, during my committee meetings.

To Professor Michael J. Cima for his excellent suggestions on the experimental approach in this thesis and for providing me the opportunity to use the scientific equipment in the CPRL.

To Professor Harry L. Tuller for many stimulating discussions and helpful suggestions.

To my colleagues in the High Temperature Process Technology group for their support and advise.

Chapter 1

Introduction

The transfer of oxygen between an electron-conducting phase and an oxygen-ion-conducting phase is an important reaction in high-temperature electrochemical devices. In solid oxide fuel cells and oxygen pumps the oxygen-transfer kinetics need to be fast in order to minimize polarization losses. In YSZ-based amperometric sensors, a precise knowledge of the oxygen-transfer mechanism is needed in order to correlate the measured current with concentration of the diffusing species. The present work elucidates the role of Pd and Pt electrodes in the transfer of oxygen across solid-electrolyte/electrode interfaces. Under appropriate thermodynamic conditions the metal electrode reacts with oxygen to form oxygen-containing species (OCS). When OCS are present at the reaction sites for oxygen transfer, the transfer process will be partially blocked. A direct current changes the local oxygen potential at the charge-transfer sites and this affects the stability of the OCS. The purpose of this thesis is to establish a link between the influence of direct current, temperature and oxygen potential on the oxygen-transfer mechanism and the reactivity of Pt and Pd electrodes with oxygen. Because of the fundamental nature of this process the

results of this thesis are directly applicable to the operation and processing of devices that use oxygen-ion-conducting electrolytes and metal electrodes.

1.1 Background to Solid-State-Electrochemical Cells and their Applications

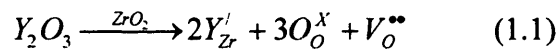
Solid-state electrochemistry has emerged as a subsection of the interdisciplinary science of solid-state ionics. It concerns a group of solid materials that conduct charge through ionic motion when they are subjected to an electrochemical-potential gradient and can therefore be seen as solid electrolytes. Just as in a liquid electrolyte, the charge transport also involves mass transport, and changes in chemical states can be directly linked to electrical phenomena. Solid-state electrochemical cells can therefore be used in applications that utilize electrochemical mass and charge conversion. This is especially useful where liquid electrolytes cannot be used. Ionic conduction is encountered in a wide range of materials ranging from ionic crystals to polymers.

Compared to cells based on liquid electrolytes, the solid electrolytes, are in some respect, simpler to analyze since no convection occurs and no solvated ions exist. Furthermore, the solid has a simpler crystallographic structure and the conduction is, in most cases, due to a single type of ion. Unfortunately this is countered by a very complicated electrode. The electrode in a solid-state cell represents an interface where the conduction changes its nature from ionic to electronic. The electrode/electrolyte interface is a region of contact between two solids where the degree of wetting is much lower than for a system with at least one liquid phase. Furthermore, the surface of the electrode is, in most cases, not sharply defined. The electrode processes frequently include chemical

reactions at the electrode surface. To add to these complexities, the ion-conducting electrolyte behaves under certain conditions as a semiconductor.

1.1.1 Stabilized-Zirconia-based Electrolytes

Unlike CeO_2 and ThO_2 , the fluorite structure is not stable at room temperature in ZrO_2 due to the small ratio between the radii of the metal ion and oxygen ion. Pure ZrO_2 has a monoclinic structure between room temperature and 1170°C . Between 1170°C and 2370°C it transforms to a tetragonal structure and, above 2370°C up to its melting point, it has a fluorite structure. Doping ZrO_2 with oxides such as CaO or Y_2O_3 stabilizes the fluorite structure from room temperature up to its melting point. These solid solutions, $(\text{ZrO}_2)_{1-x}(\text{MeO})_x$ are called stabilized zirconias. Doping zirconia with an oxide where the cation has a different valence means that the host Zr^{4+} is replaced by Me^{z+} . If the charge difference $4-z$ is positive, it means that the non-stoichiometry is compensated by either oxygen vacancies or interstitial cations. Density measurements [Hund 1951] show, however, that the oxygen vacancies are the compensating defects. This gives in Kröger-Vink notations for the case of the dopant Y_2O_3 [Kröger 1979]:



In undoped ZrO_2 the ionic conductivity due to Schottky-type defects is low. Increased oxygen-vacancy concentration due to aliovalent doping enhances the ionic conductivity according to [Schmalzried 1981, Shewmon 1989]:

$$\sigma = [\text{V}^{\bullet\bullet}_{\text{O}}]me \quad (1.2)$$

where m is the ion mobility and e is the electron charge .

The high ionic conductivity in fluorite-type solid solutions is due to the high range of aliovalent-dopant solubility that the structure allows for [Kudo 1990]. It is suggested that this is due to the low packing (see figure 1.1) density [Kudo 1990]. The loose structure allows a high solubility of dopants by accommodating a great degree of defects.

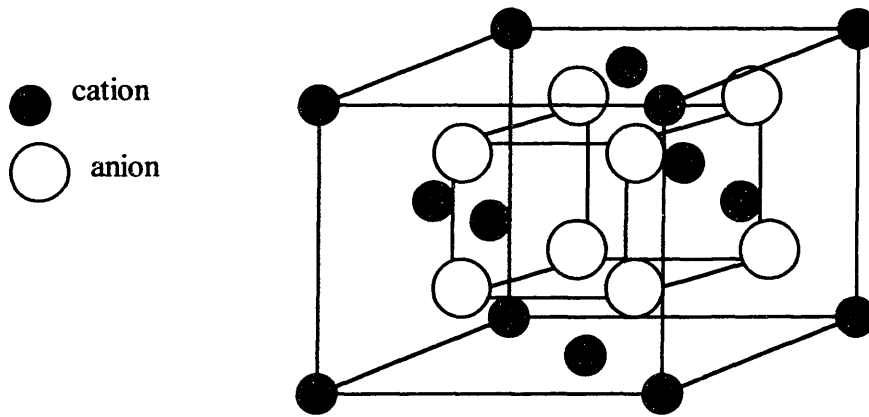


Figure 1.1. Unit cell for Fluorite structure.

As seen in figure 1.2 [Baumard 1984] the ionic conductivity of ZrO_2 - Y_2O_3 does increase with an increasing dopant concentration in the low-concentration region. When doped above 8-10 mole% Y_2O_3 the conductivity of the solution begins to drop. The decay is believed to be due to the clustering of oxygen vacancies [Kudo 1990], the formation of defect pairs, or the formation of an ordered superlattice.

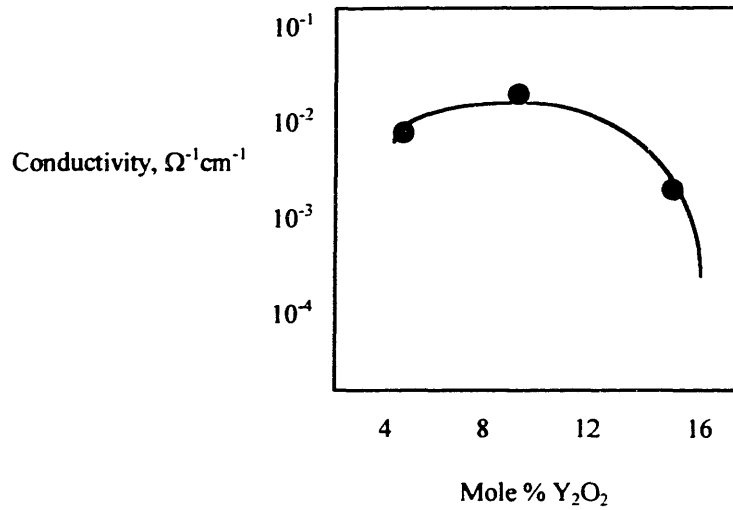
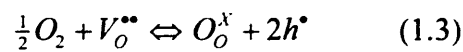


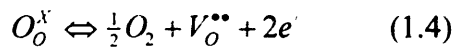
Figure 1.2. Effect of dopant concentration on oxygen-ion conductivity for the $\text{ZrO}_2\text{-Y}_2\text{O}_3$ system [Baumard 1984].

The electrical conductivity in stabilized ZrO_2 can also appear via electronic-charge carriers at extreme oxygen partial pressures, P_{O_2} . This is due to a nonstoichiometry in the oxygen concentration.

Under high P_{O_2} :



and under low P_{O_2} :



The contribution of the electronic conductivity is negligible (ionic conductivity is more than 4 orders of higher magnitude) when P_{O_2} is in the range: 0.21 and 10^{-20} atm and the temperature is below 900°C [Weppner 1977].

1.1.2 Solid Oxide Fuel Cells (SOFC)

The high ionic conductivity enables the use of stabilized zirconias as electrolytes for solid oxide fuel cells. The principle of the cell operation is shown in figure 1.3.

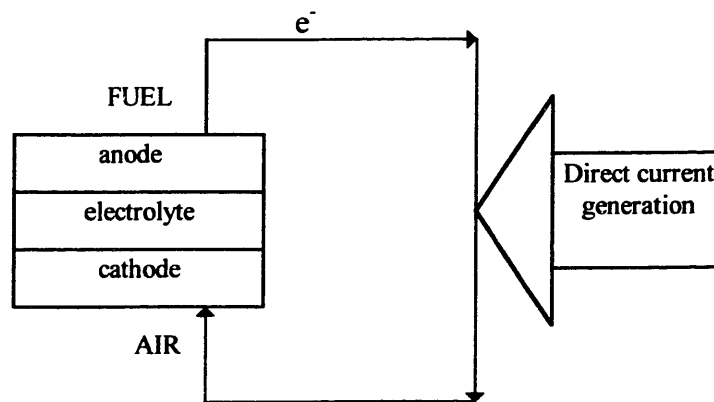
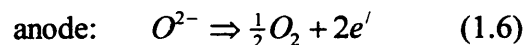
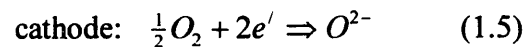


Figure 1.3. Schematic diagram of SOFC.

The SOFC converts chemical energy into electricity electrochemically by combining fuel and oxidant gases through an oxygen-ion-conducting electrolyte. Oxygen is reduced at the cathode, transported through the electrolyte, and oxidized at the anode, according to the following two reactions:



Fuel, in the form of H₂, CO, or hydrocarbons, is passed over the anode while oxidants (typically air) are supplied at the cathode. Direct current is supplied to a load when the electrons in eqs. (1.5) and (1.6) are led through an external electronic lead connecting the anode and the cathode. The selection of the electrode materials are extremely important in order to lower the polarization. The electrode must have a high electronic conductivity in order to act as current collectors but they also have to be electrocatalytic with respect to

reactions (1.5) and (1.6). The cathode needs to be chemically stable in oxidizing atmospheres at high temperatures. There are few materials that are stable under these conditions. Noble metals (Pt, Pd or Au) and certain conducting ceramics (doped LaMnO_3) are currently used. The anode in SOFC:s often needs to catalyze not only reaction (1.6) but also chemical reactions such as the internal steam reforming of hydrocarbons [Singh 1989]. Hence the anode usually consists of catalytically-active metals such as Ni or Pt [Trimm 1988]. State-of-the-art SOFC consist of an anode made of porous Ni/YSZ cermets, YSZ electrolyte, and a porous LaMnO_3 cathode [Minh 1995].

1.1.3 Potentiometric and Amperometric Sensors

Zirconia-based sensors are used in many applications, such as the measurement of oxygen potential in molten metals/slugs or combustion gases. An example of a potentiometric sensor to measure oxygen partial pressure P_{O_2} is shown in figure 1.4.

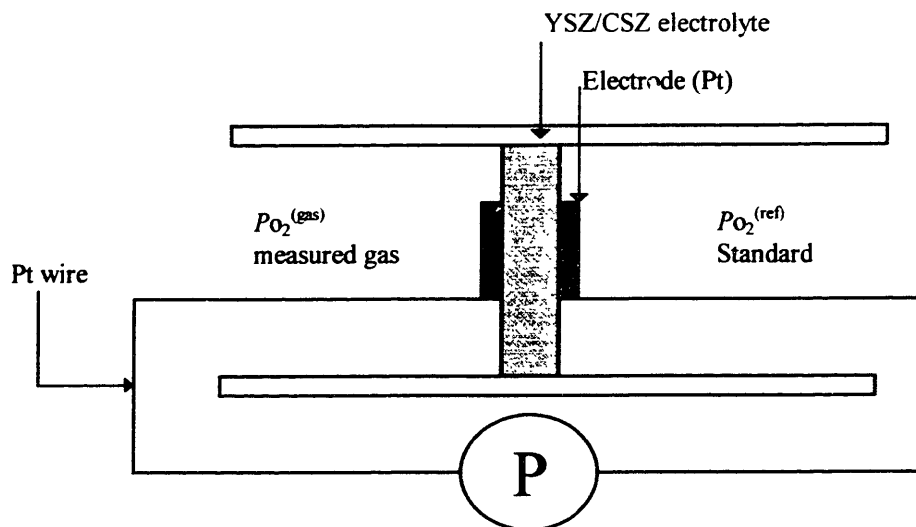
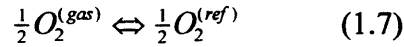


Figure 1.4. Potentiometric oxygen sensor.

Here an oxygen-ion-conducting electrolyte (YSZ or CSZ) separates two compartments. On one side there is a reference oxygen potential $P_{O_2}^{(ref)}$. The reference oxygen potential is established through either a known gas mixture or a metal/metal oxide mixture such as Cr/Cr₂O₃. The other compartment contains the gas whose oxygen potential is to be measured. An open-circuit electrical potential is measured between the electrodes attached to the electrolyte in the respective compartments with a potentiometer. The potential is set by virtue of the equilibrium of reactions (1.5) and (1.6), the sum of which is:



$$E = \frac{1}{4F} (\mu^{(g)} - \mu^{(ref)}) = \frac{RT}{4F} \ln \left(\frac{P_{O_2}^{(g)}}{P_{O_2}^{(ref)}} \right) \quad (1.8)$$

The oxygen partial pressure of the gas is calculated from equation (1.8). The measured potential is for the immediate vicinity of the electrode. The conditions at the electrode are therefore important. For example, transport limitations at a porous electrode, or reactions between the gas, liquid metal, or slag, may result in deviations of the measured potential from the bulk. It is therefore important to know exactly where in the electrode the equilibrium represented by (1.7) is established and how the electrode is chemically influenced by the environment.

Amperometric sensors are based on measuring the limiting current and thereby calculating the oxygen potential. Typically, the limiting current is determined from the polarization characteristics (see figure 1.5 and 1.6) and the oxygen potential is calculated from the diffusion profile near the electrode. The limiting current may arise due to local transport limitations at the electrode. This may be due to the electrode reacting with the environment. If the electrode is not inert with respect to the environment, then it is

difficult to obtain a stable reading for the limiting current. Furthermore, if changes in the electrode microstructure occur during operation, the limiting current can not be easily related to concentrations in the bulk.

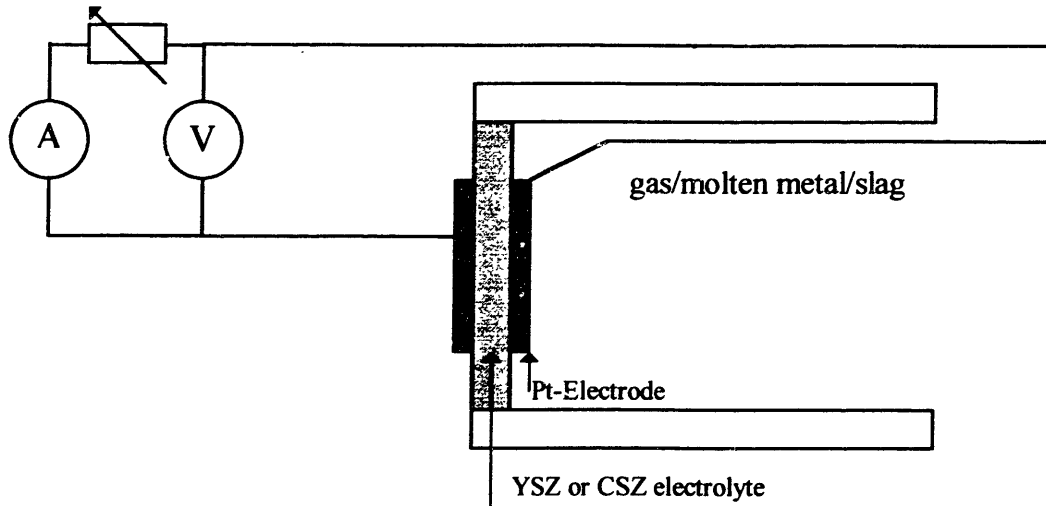


Figure 1.5 Amperometric sensor for measuring the limiting current.

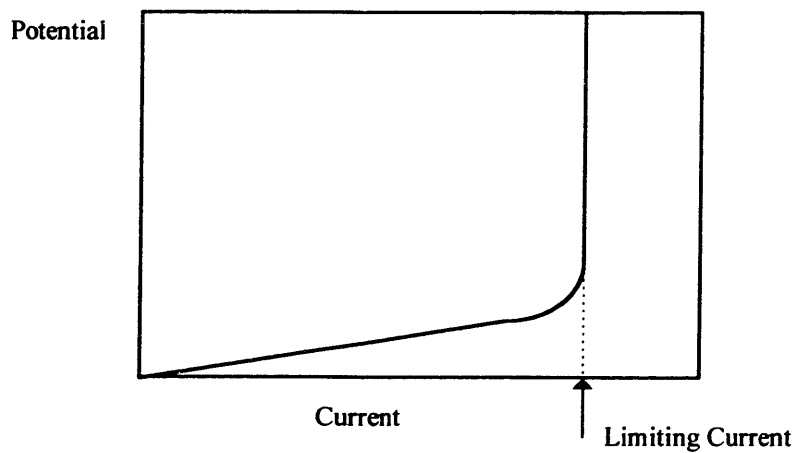


Figure 1.6 Limiting current evaluated from the polarization characteristics.

1.1.4 Oxygen Pumps

Zirconia-based oxygen pumps provide an excellent way to control oxygen pressures. Unlike mechanical techniques, they cover a wide range of P_{O_2} down to 10^{-38} atm [Yuan 1969]. They are used primarily for obtaining ultra-low oxygen potentials but can essentially be used for refining industrial gases also. The principle of operation of a zirconia-based oxygen pump is shown in figure 1.7.

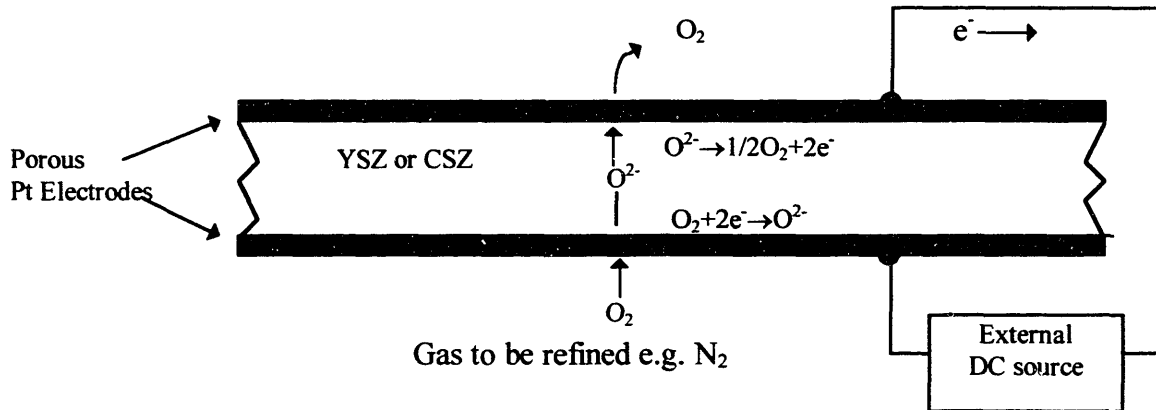


Figure 1.7. Zirconia-based oxygen pump.

Porous Pt electrode paste is applied to both sides of a YSZ (or CSZ) membrane, and an applied electric potential forces the oxygen from one side to the other. The efficiency of the process is determined by the kinetics of the electrode reactions (1.5) and (1.6). The rate at which molecular oxygen is pumped is equal to $I/4F$.

1.2 The Importance of Studying the Oxygen-Transfer Reaction

The study of the reactions occurring at a gas/metal electrode/YSZ electrolyte is necessary in order to understand and optimize the processes occurring in various electrochemical devices based on zirconia electrolytes. The study of noble-metal electrodes is directly applicable to the design of sensors and oxygen pumps since these devices frequently use Pt electrodes. State-of-the-art SOFC use Ni/YSZ cermet anodes and LaMnO₃ cathodes. Ni/YSZ cermets are only stable in reducing atmospheres, and the different interfaces are hard to quantify. The use of noble-metal pastes offers an easily controllable electrode morphology. They are stable in reducing as well as oxidizing atmospheres. If a mechanistic theory can be established for oxygen and charge transfer between electronic conductors and ionic conductors through a study of noble metal/YSZ interfaces, the Ni/YSZ cermets can be tailored to be more effective electrocatalysts.

It is as yet unclear where exactly the oxygen-transfer reaction occurs. The role of the different phases (ionic conductor, electronic conductor, mixed conductor, and gas) is not known. Finally, there is a lot of disagreement among the studies about the rate-determining step. The complexity and interdependence of electrochemical and chemical reactions in these systems may explain the uncertainties still present in the description of electrode processes.

The work done over the last decades in the analysis of the cathodic processes was reviewed recently by a number of authors [Siebert 1994, Steele 1995, Barbi 1995, Wiemhofer 1993, Wiemhofer 1995], who pointed out the remaining uncertainties regarding the elementary steps of the reaction mechanism. The uncertainties arise due to

the differences in electrode areas, gas atmospheres, and temperature regions. that existed during the studies. The elementary steps of the anodic reaction have not been extensively investigated and are even less understood than the cathodic reaction. The use of different fuel gases leads to a multitude of electrocatalytic reactions, which add to the complexity of the system. The mechanism, and the role of the oxygen reduction/oxidation as a necessary first step in any of these reactions, is still under analysis.

The information available on the reaction mechanisms at the gas/Pt/YSZ interface while current is passing is relatively scarce. From our current-interruption studies, coupled with electrochemical impedance spectroscopy (EIS), we have reason to believe that the investigation of interfaces during current passage and shortly after current interruption may provide valuable information regarding the processes occurring under current flow conditions. The reaction path and the kinetics of individual steps may be substantially altered after a faradaic current flows through the cell.

1.3 Objective

The initial objective of this work was to study the electrocatalytic role of Ni-YSZ cermet anodes on steam reforming of hydrocarbons in solid oxide fuel cells. A laboratory-scale fuel cell was built with Pt cathode, YSZ electrolyte and Ni-YSZ anode. In the electrochemical measurements the cell impedance under near equilibrium conditions was substantially altered after maintaining the cell under load. This seemingly anomalous behavior meant that one or many of the processes that are responsible for the cell impedance change irreversibly due to current passage. The consequence is that the

electrochemical overpotential measurements that constitute the polarization characteristics at different currents are not easily interpreted. The source of the current-induced effect on the impedance needed to be identified. The solid electrolyte under load supplies or depletes oxygen locally at the electrode/electrolyte interface. This interface was experimentally isolated in order to study the effect of current on the Pt/YSZ interfacial impedance. The initial experiments revealed that the kinetics of the oxygen-exchange reaction was slowed after supplying oxygen to the reaction sites (anodic currents). Depleting oxygen from the reaction sites with a cathodic currents enhanced the rate of the oxygen-exchange reaction. This meant that the electrode was affected by the local change in oxygen potential. Pt is generally thought to be inert with respect to high-temperature oxidation but there is evidence in the catalysis literature that various oxygen compounds form at the Pt surface. The observations prompted a change in the direction of the research. The objective was to answer the following questions:

- *What is the role of the electrode beyond current collection?*
- *Is the electrode or electrode/electrolyte interface inert with respect to oxygen and if not, does this affect the interfacial oxygen transfer process?*

Based on the results obtained for Pt/YSZ interfaces a hypothesis was formulated that the oxygen transfer process is slowed by the presence of oxygen compounds at the oxygen transfer sites. The effect of temperature, oxygen-partial pressure and current on the interfacial impedance was correlated with the stability of oxygen compounds on platinum.

The lack of thermodynamic data on oxygen compounds on platinum led to the testing of the hypothesis for a system with a well known oxidation thermodynamics, namely Pd/YSZ. The results from the investigation of the Pd/YSZ system confirmed the hypothesis.

1.4. Layout of the Thesis

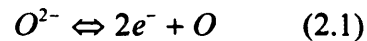
Chapter 2 provides the theoretical background on how the electrical impedance response is interpreted in terms of electrochemical, chemical or transport processes. Included is also a summary of the available information on oxygen interaction with platinum and palladium. Based on this information, the basic hypothesis of the role of oxygen on the charge transfer process is presented. Chapter 3 describes the experimental approach. The organization of the remainder of the thesis follows the order in which the work was carried out. Chapter 4 presents briefly the steam reforming studies, wherein the first observations of a current induced change on the oxygen transfer process were made. Chapter 5 deals with the results from the electrochemical impedance measurements of the Pt/YSZ interface. The hypothesis presented at the end of chapter 2 is expanded to a two-path- physico-chemical model. The model is correlated with the data on oxygen-platinum interactions that are summarized in chapter 2. Chapter 6 includes the work on Pd/YSZ. Since the Pd/YSZ interface has been less studied compared to the Pt/YSZ interface the near equilibrium results are analyzed in detail in order to construct an impedance model for the oxygen transfer process. The model developed in chapter 5 is then tested for the Pd/YSZ interface and correlated with the oxidation thermodynamics of Pd. The

conclusions of the thesis are summarized in chapter 7. The results of this thesis show that Pt and Pd electrodes are affected by the local changes in oxygen potential caused by direct current. This has important consequences on the operation and processing of the various electrochemical devices that are to be used under current passing conditions. Chapter 8 discusses the implication of the results of this thesis on SOFC and amperometric sensors. Chapter 8 also includes suggestions for future work.

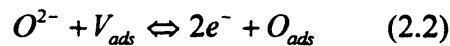
Chapter 2

The Complexity of the Oxygen-Transfer Reaction

The kinetics of the oxygen and charge transfer across electrode/YSZ-electrolyte systems is extremely important for many electrochemical devices, such as solid oxide fuel cells, sensors, and oxygen pumps. The exchange reaction at the interface is the following:



The oxygen atoms are either adsorbed at a free surface, combined and evaporated, or dissolved into an oxygen-dissolving phase. Assuming insolubility, reaction (2.1) is expanded to:



The above reaction involves the participation of ionic oxygen, atomic oxygen, vacant adsorption sites, and electrons. Hence, it takes place in the simultaneous presence of an oxygen-ion conducting phase (e.g. YSZ), a free surface, and an electron-conducting phase (e.g. a metal). The idle rate of this reaction can be represented by the exchange current.

$$I_0 = f(n, A, T, [V_{ads}], [O_{ads}]) \quad (2.3)$$

Mechanistically this is an extremely complex problem to analyze, in particular because the reaction sites are not of a simple nature and therefore it is hard even to identify them, and even harder to quantify the effective reaction area A . Furthermore, the reaction area A is, of course, not independent of the concentration of $[V_{ads}]$. The present chapter aims at elucidating the current understanding of the mechanisms behind reaction (2.1) and the ambiguities therein.

The chapter also describes the various models that connect the electrochemical impedance response to chemical processes. All existing models are based on measurements under static condition, i.e. zero-current flow. It is likely, that the electrodes are affected by the changes in local oxygen potentials induced by a current. The reason for this is that the thermodynamic stability of oxygen-containing species (OCS) are affected by the local oxygen potential changes at the charge-transfer sites. The presence of OCS affects the charge-transfer reaction by lowering the effective number of reaction sites. At the end of this chapter a summary of the existing data on the oxygen-Pt and oxygen-Pd interactions are given in order to show that the dynamic state (under current flow) of the interface may differ from the static (zero current flow). The role of OCS as a possible inhibitor of the oxygen-exchange reaction is discussed.

2.1 Two Basic Types of Interfaces

Interfaces where oxygen and charge transfer occurs on oxygen-conducting electrolytes can be separated into two basic types.

TYPE I - The first type is an interface between a purely electron-conducting current collector and a purely ion-conducting electrolyte. Noble metal-YSZ interfaces belong to this category. The solubility of oxygen is generally low in the electron-conducting phase and thus the exchange reaction occurs mainly at the surface in a sorption layer. There are many proposed models but it is generally agreed that the actual charge transfer occurs at or near the triple-phase boundaries (electronic conductor/ionic conductor/gas, see the dashed circle in Figure 2.1). The overpotential is related to the temperature and the oxygen potential at the electrode.

Type I

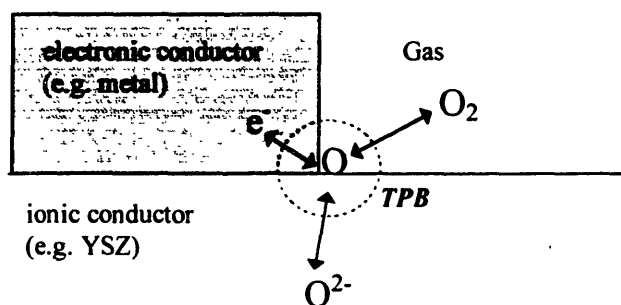


Figure 2.1 The triple phase boundary (TPB).

TYPE II - In a type II interface, the electrode is able to dissolve oxygen either as oxygen ions (mixed-conducting oxides), or as atomic oxygen (e.g. silver). In the case of a mixed-conducting-oxide electrode, the overpotential is also related to the oxygen-vacancy gradient between the electrode/gas interface and the electrode/electrolyte interface. The contact area between the electrolyte and electrode, as well as the thickness of the

electrode, plays an important role. The oxygen and charge transfer occurs via an area instead of a triple-phase boundary [Hammouche 1989]. Some investigators have found that even in these cases, the currents through the electrolyte does in fact also flow from triple-phase boundaries [Misuzaki 1994]. The triple-phase boundaries are extremely electrocatalytic with respect to the oxygen and charge-transfer reaction. If the mixed-conducting layer were dense the electrode performance would not be as good as for a porous layer. [Hammouche 1989] found that layers of $\text{La}_{1-x}\text{Sr}_x\text{MnO}_3$ initially showed very small faradaic currents when they were polarized. There would, however, after enough polarization, appear a large faradaic current. This change was accompanied by the formation of oxygen vacancies due to the decomposition of the electrode.

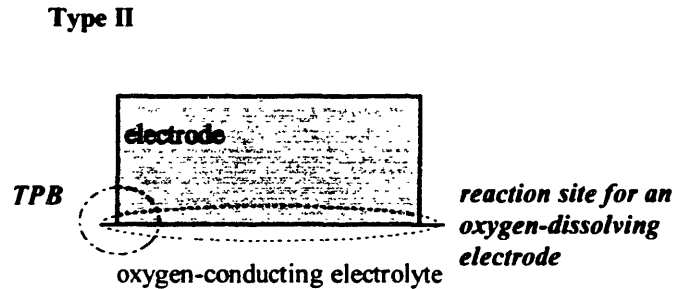


Figure 2.2 Reaction sites for type II interface (In a mixed-conducting electrode, the TPB and the entire electrode surface are reaction sites).

2.2 The Metal/YSZ Interface

Metal/YSZ interfaces belong to type I in the classification above. Pt/YSZ is generally chosen as a model interface for the study of reaction (2.2) at the metal/YSZ

interfaces. This is due to the following reasons. The study of Pt as an electrode material is directly applicable to sensors and oxygen pumps. Furthermore, an understanding of the fundamental reaction steps at the Pt/YSZ interfaces can be used to elucidate the role of the Ni/YSZ cermets as electrocatalysts in SOFC anodes. Finally, Pt is suitable for a mechanistic investigation as it allows a study to be conducted in a wide P_{O_2} and temperature range.

2.2.1 Pt/YSZ

Reviews on the work done in the analysis of the cathodic process in the Pt/YSZ system [Siebert 1994, Steele 1995, Barbi 1995, Wiemhofer 1993, Wiemhofer 1995], show that there still remains uncertainties regarding the elementary steps of the oxygen and charge transfer mechanism. The elementary steps of the anodic reaction are less understood since the different fuel gases add to the complexity. This is due to the complicated couplings between the electrode reaction and the chemical reactions between the fuel gas and oxygen. The mechanism and the role of the oxygen reduction/oxidation as a necessary first step in any of these reactions is still under analysis. The discrepancies are partly due to the use of different processing techniques by different authors resulting in different electrode microstructures. This makes a direct comparison between various studies difficult. Most investigators study only a narrow temperature and P_{O_2} range.

Furthermore, the information available on the reaction mechanisms at the gas/Pt/YSZ interface while current is passing is scarce. The reaction path and the kinetics

of individual steps may be substantially altered after a faradaic current flows through the cell.

The following is a summary of the different intermediate reaction steps that may occur at the Pt/YSZ interface. With respect to reaction (2.2) the schematic represents the cathodic direction.

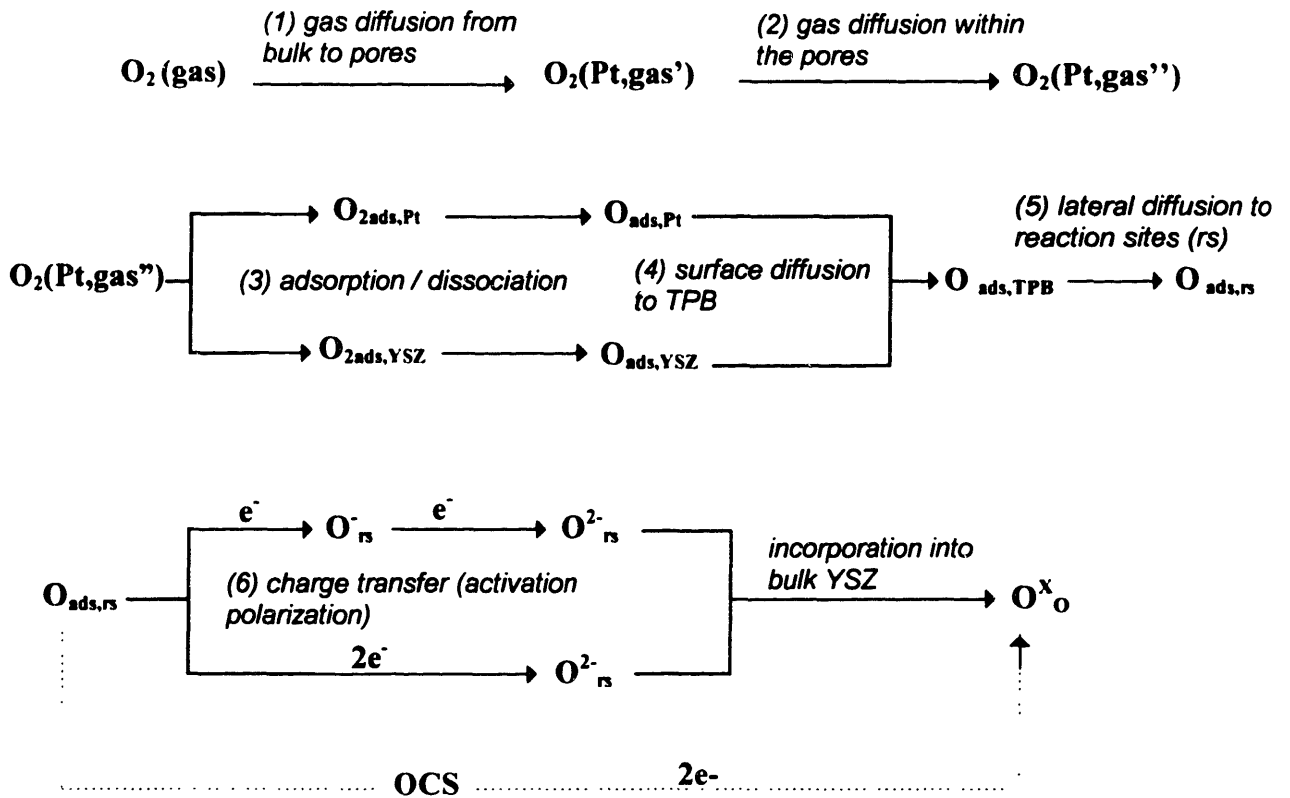


Figure 2.3 Schematic of the pathways of oxygen and charge transfer at the Pt/YSZ interfaces.

The rate-limiting step for the oxygen transfer may be any of the steps in figure 2.3. Gas-phase diffusion has been suggested as the rate-limiting step in references [Etsell 1971, Gür 1980, Braunshtein 1981]. The behavior of oxygen on the surface of YSZ is not well known but, on transition metals, oxygen is assumed to undergo dissociative adsorption [Anderson 1975]. Bauerle concluded this to be the rate-limiting step in his pioneering work with impedance spectroscopy [Bauerle 1969]. Bulk diffusion of oxygen in Pt has been discarded since the activation energy is 6 times higher than for surface diffusion [Moghadam 1986]. Surface diffusion of oxygen atoms on Pt has been suggested as rate-limiting [Pizzini 1973, Mizusaki 1987]. Lateral diffusion of oxygen in the YSZ/Pt interface was found to be rate-limiting by Wang et al. (Wang 1981). The dashed path represents oxygen-charge transfer reaction through oxygen-containing species (OCS). It is the objective of this work to investigate this mechanism.

2.2.2 The Electrical Analogs of Physical and Chemical Processes at YSZ / Metal Interfaces

The following section connects the interfacial impedance response to the various kinetic processes presented in figure 2.3. The P_{O_2} and temperature dependencies will be discussed. The reaction scheme presented in figure 2.3 has Platinum as a metal electrode, but the scheme can be viewed as more general and hence applicable to any metal that does not dissolve oxygen appreciably. It should be remembered, however, that the dashed-OCS path will be strongly influenced by the degree of inertness of the metal. For metals such as Ni and Co, the OCS path may be encountered only under oxidizing conditions

whereas for Pt and Pd the influence of OCS on the oxygen-exchange reaction may only be encountered under specific thermal and chemical conditions.

The YSZ/Metal interface can be characterized as an electrical circuit consisting of a double layer capacitance in parallel with a faradaic impedance [Macdonald 1987, Bruce 1995] as shown in figure 2.4.

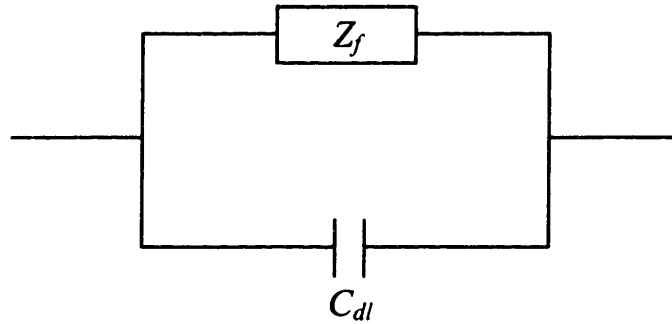


Figure 2.4 The metal-YSZ Interface.

The double layer capacitance C_{dl} for the YSZ/Pt interface has been reported by many investigators [Winnubst 1984, Bauerle 1969, Ververk 1983, Velle 1991] and the values lie between 60-350 $\mu\text{F}/\text{cm}^2$. Wang et al. [Wang 1979] found the C_{dl} to be between 30-125 $\mu\text{F}/\text{cm}^2$ for the Pt/CeO₂-CaO interface. No P_{O_2} dependence has been observed. The faradaic impedance Z_f can be investigated in order to find its adherence to the steps in figure 2.3. The faradaic impedance is the ratio between the ac parts of the voltage and the current $\Delta V / \Delta i_f$. The change in the faradaic current due to a small-signal perturbation is generally expressed as a Taylor expansion [Macdonald 1987].

$$\Delta i_f = \left(\frac{\partial i_f}{\partial V} \right)_c \Delta V + \sum \left(\frac{\partial i_f}{\partial C_i} \right)_V \Delta C_i + \text{higher - order terms} \quad (2.4)$$

Here C_i represents the concentration of the redox species at the interface. If the higher order terms are neglected (the signal is small enough such that the system responds linearly), the impedance can be written as:

$$Z_f = \frac{1}{\left(\frac{\partial \mathcal{V}}{\partial \mathcal{V}}\right)_{C_i}} \left(1 + \sum \left(\frac{\partial \mathcal{V}}{\partial C_i} \right)_V \frac{\Delta C_i}{\Delta i_f} \right) \quad (2.5)$$

The first term within the parenthesis in equation (2.5) describes the influence of charge - transfer resistance, and the second term is the influence of mass transport. The faradaic impedance in figure 2.4 can now be separated into two parts: $Z_f = R_{ct} + Z_{mt}$. For the YSZ/Metal system, assuming that no stable intermediate species are formed, the only independent concentration is that of the adsorbed oxygen O_{ads} (equation 2.2). The concentration is equal to the fraction of covered surface sites θ . Equation (2.5) thus becomes:

$$Z_f = \frac{1}{\left(\frac{\partial \mathcal{V}}{\partial \mathcal{V}}\right)_{\theta}} \left(1 - \left(\frac{\partial \mathcal{V}}{\partial \theta} \right)_V \frac{\Delta \theta}{\Delta i_f} \right) \quad (2.6)$$

The charge transfer part in equation (2.6) is representative of step (6) in the reaction scheme in figure 2.3. Steps (1)-(5) in figure 2.3 constitute the mass-transport term in equation (2.6).

For high-temperature systems, the relaxation frequency of interfacial-charge-transfer impedance is so fast that it appears only in the high frequency range wherein the chemical species (that participate in the mass transport process) are unaffected by the ac perturbation. Therefore if the relaxation frequency is high, the charge transfer can be

isolated in the impedance spectra. It should be mentioned, however, that this does not imply in any way that the charge-transfer resistance is generally rate controlling. It is most likely that a mass transport process will take over upon the slightest dc polarization. Pure charge transfer is only encountered if the ac frequency is sufficiently high so that $\theta = \theta_{eq}$.

2.2.2.1 Charge-transfer Resistance (R_{ct})

The charge-transfer resistance is given by the first part of equation (2.6) as

$$R_{ct} = \frac{1}{\left(\frac{\partial \bar{\alpha}_f}{\partial V}\right)_\theta} \quad (2.7)$$

The Butler-Volmer equation for reaction (2.2) is:

$$i_f = i_0 \left\{ \frac{1-\theta}{1-\theta_{eq}} \exp\left(\frac{\alpha_a n F \eta}{RT}\right) - \frac{\theta}{\theta_{eq}} \exp\left(\frac{-\alpha_c n F \eta}{RT}\right) \right\} \quad (2.8)$$

Here, θ_{eq} is the fraction of surface sites that are covered with adsorbed oxygen under equilibrium conditions. α_a and α_c are the anodic and cathodic transference coefficients, respectively. α_a and α_c are often taken to be 1/2 without proper justification. Bockris and Reddy [Bockris 1977] give a more general treatment which is used in the present work. η is the overpotential. i_0 is the exchange current which can be shown to be [Bockris 1977]:

$$i_0 = nFAk_r(1-\theta_{eq})^{\alpha_c}(\theta_{eq})^{\alpha_a} \quad (2.9)$$

Here n is the number of electrons transferred and $k_r = k_{r0} \exp(-E_r/RT)$. If $\Delta\theta$ is small due to steps (1)-(5) in figure 2.3 being near equilibrium, then (2.8) becomes:

$$i_f = i_0 \left\{ \exp\left(\frac{\alpha_a n F \eta}{RT}\right) - \exp\left(\frac{-\alpha_c n F \eta}{RT}\right) \right\} \quad (2.10)$$

By using equation (2.10) in equation (2.7) and assuming that the overpotential η is small, R_{ct} is readily evaluated:

$$R_{ct} = \frac{RT}{nFi_0(\alpha_a + \alpha_c)} \quad (2.11)$$

Note that equation (2.11) includes the exchange current given by (2.9) in the denominator. Since θ_{eq} represents the equilibrium coverage, it is set by the oxygen potential in the gas phase through an adsorption isotherm. Assuming a Langmuir-adsorption isotherm, the equilibrium can be written for dissociative and molecular adsorption respectively:

$$\frac{\theta_{eq}}{1 - \theta_{eq}} = K_{diss}(PO_2)^{1/2} \quad [\text{dissociative}] \quad (2.12)$$

$$\frac{\theta_{eq}}{1 - \theta_{eq}} = K_{diss}PO_2 \quad [\text{molecular}] \quad (2.13)$$

Equilibrium (2.12) is inserted in the expression for the exchange current (2.9) resulting in the charge-transfer resistance in the case of dissociative adsorption (2.11).

Under high coverage ($\theta_{eq} \approx 1$):

$$R_{ct} = \frac{RT}{(\alpha_a + \alpha_c)n^2F^2 Ak_r (K_{diss}PO_2)^{-\frac{\alpha_c}{2(\alpha_c + \alpha_a)}}} \quad (2.14)$$

Under low coverage ($1 - \theta_{eq} \approx 1$):

$$R_{ct} = \frac{RT}{(\alpha_a + \alpha_c)n^2F^2 Ak_r (K_{diss}PO_2)^{\frac{\alpha_c}{2(\alpha_c + \alpha_a)}}} \quad (2.15)$$

In the case of molecular adsorption without dissociation, equation (2.13) would be used instead of (2.12) and the factor 1/2 in the exponent of the denominator in (2.14) and (2.15) would disappear.

The dependence of $\ln(R_{ct})$ on $1/T$ would reveal an apparent activation energy Q , which is a sum of the activation energy of the exchange current E_r and a contribution from the heat of adsorption ($K_{ads} = K_0 \exp(\Delta H_{ads})$). The heat of adsorption is the negative of the free enthalpy change for equilibrium (2.12) or (2.13), ($\Delta H_{ads} = -\Delta H$).

$$Q = \left(\frac{\partial \ln(R_{ct})}{\partial 1/T} \right) = E_r \pm \left(\frac{\alpha_c}{\alpha_c + \alpha_a} \right) \frac{\Delta H_{ads}}{2} \quad (2.16)$$

The sign in front of the second term is positive in the case of a high surface coverage ($\theta_{eq}=1$) and negative for a low surface coverage ($1 - \theta_{eq}=1$). The factor 1/2 in the second term disappears in the case of molecular adsorption.

A dependence of P_{O_2} on R_{ct} can be predicted from equations (2.14) and (2.15). This is defined by α_a and α_c , which depend on the slowest step of a multistep-charge-transfer process. The details of the treatment are outlined by Bockris and Reddy [Bockris 1977]. α_a and α_c are calculated from the following two equations:

$$\alpha_a = \frac{n - \gamma_a}{\nu} - r\beta \quad (2.17)$$

$$\alpha_c = \frac{\gamma_b}{\nu} + r\beta \quad (2.18)$$

n is the total number of electrons transferred, γ_b is the number of electrons transferred before the slowest step, and γ_a is the number of electrons transferred after the slowest step. r is the number of electrons transferred during the slowest step, and ν is the number

of times that the slowest step has to repeat itself. β is the symmetry coefficient, and is taken as 1/2.

Oxygen is known to chemisorb dissociatively on metals at high temperatures [Anderson 1975]. With this assumption, different multistep reaction sequences will now be analyzed in the light of equations (2.17) and (2.18). Once the P_{O_2} dependence on R_{ct} in equation (2.14) is measured, the obtained result can be compared with the tables below.

Table 2.1 Reaction schemes for oxygen transfer.
(a)-(b) : No charged intermediates. (c)-(f) : Charged intermediates are formed.

(a)	reaction steps	α_a	α_c	$\frac{\alpha_c}{2(\alpha_c + \alpha_a)}$
	(A1) $1/2O_2(g) = O_{ads} = O_{rs}$	-	-	-
	(A2) $O_{rs} + 2e^- \Rightarrow O^{2-}$	1	1	1/4

(b)	reaction steps	α_a	α_c	$\frac{\alpha_c}{2(\alpha_c + \alpha_a)}$
	(B1) $1/2O_2(g) = O_{ads} = O_{rs}$	-	-	-
	(B2) $O_{rs} + e^- \Rightarrow O_{rs}^-$	3/2	1/2	1/8
	(B3) $O_{rs}^- \Rightarrow O_{rs'}^-$ †	1	1	1/4
	(B4) $O_{rs'}^- + e^- \Rightarrow O^{2-}$	1/2	3/2	3/8

Dissociated oxygen (unlike H,S,N where the surface bonds are essentially covalent) has been found to carry a negative charge [Anderson 1975]. Based on this finding, four additional reaction schemes are presented.

(c)	reaction steps	α_a	α_c	$\frac{\alpha_c}{2(\alpha_c + \alpha_a)}$
	(C1) $O_2(g) + e^- = O_{ads} + O_{ads}^-$	7/2	1/2	1/16
	(C2) $O_{ads}^- + O_{ads} \Rightarrow O_{rs}^- + O_{rs}$	3	1	1/8
	(C3) $O_{rs}^- + O_{rs} + 3e^- \Rightarrow 2O^{2-}$	1/2	5/2	1/2

† rs and rs' both represent reaction sites where charge transfer take place; the differentiation is made only to represent the possibility of a mass-transport step in between charge-transfer steps

(d)	reaction steps	α_a	α_c	$\frac{\alpha_c}{2(\alpha_c + \alpha_a)}$
	(D1) $O_2(g) + 2e^- = 2O_{ads}^-$	3	1	1/8
	(D2) $2O_{ads}^- \Rightarrow 2O_{rs}^-$	2	2	1/4
	(D3) $2O_{rs}^- + 2e^- \Rightarrow 2O^{2-}$	1	3	3/8

(e)	reaction steps	α_a	α_c	$\frac{\alpha_c}{2(\alpha_c + \alpha_a)}$
	(C1) $O_2(g) + 2e^- = O_{ads} + O_{ads}^{2-}$	3	1	1/8
	(C2) $O_{ads}^{2-} + O_{ads} \Rightarrow O^{2-} + O_{rs}$	2	2	1/4
	(C3) $O_{rs} + 2e^- \Rightarrow O^{2-}$	1	3	3/8

(f)	reaction steps	α_a	α_c	$\frac{\alpha_c}{2(\alpha_c + \alpha_a)}$
	(E1) $O_2(g) + 3e^- = O_{ads}^- + O_{ads}^{2-}$	5/2	3/2	3/16
	(E2) $O_{ads}^{2-} + O_{ads}^- \Rightarrow O_{YSZ}^{2-} + O_{rs}^-$	1	3	3/8
	(E3) $O_{rs}^- + e^- \Rightarrow O_{YSZ}^{2-}$	1/2	7/2	7/16

2.2.2.2 Mass Transport Impedance Z_{mt}

The mass-transport impedance, Z_{mt} , is given by the second term in equation (2.6):

$$Z_{mt} = - \frac{\left(\frac{\partial i_f}{\partial \theta} \right)_v \frac{\Delta \theta}{\Delta i_f}}{\left(\frac{\partial i_f}{\partial \mathcal{V}} \right)_\theta} \quad (2.19)$$

The denominator is evaluated from equation (2.10) and the first term in the numerator from equation (2.8). The second term, $\Delta \theta / \Delta i_f$, is obtained by solving an equation for the mass transport with appropriate boundary conditions. In this section, models for the various mass transport steps in figure 2.3 are presented. Steps 1 and 2 represent gas - diffusion processes and are not treated here. They are not expected to be rate controlling in porous and thin electrodes for near-equilibrium conditions [Misuzaki 1987]. The first

two cases are adsorption (step 3 in figure 2.3) and surface diffusion (step 4 in figure 2.3). These processes are purely mass transport controlled. The derivations of the impedances corresponding to these processes are therefore based on equation 2.19. The third process (step 5 in figure 2.3) represents a competition between mass transport and charge transfer and the derivation of the impedance is in this case based on equation 2.6.

Dissociative adsorption of atomic oxygen (step 3 in figure 2.3)

If the adsorption/desorption is not fast enough compared to the diffusion and charge transfer, Z_{mt} will depend on the kinetics of equilibration between oxygen in the gas phase and the adsorbed state. Franceschetti (Franceschetti 1986) developed a model consisting of an RC parallel circuit. R was inversely proportional to the kinetic rate constant for equilibration with the gas phase ($k_{eff} = |k_{adsorb} - k_{desorb}|$). The origin of C is unclear but it may be related to the fact that dissociated oxygen atoms tend to be negatively charged.

$$R_{mt} \propto \frac{1}{k_{eff}} \quad (2.20)$$

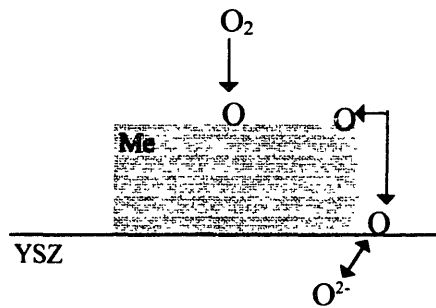


Figure 2.5 Process wherein Adsorption kinetics is rate controlling.

Surface diffusion towards triple phase boundary (step 4 in figure 2.3)

The situation is illustrated in figure 2.6. The assumption is that adsorbed oxygen atoms have to diffuse a distance δ to the triple phase boundary on the surface of the electrode. The reason for this is that the adsorption rate is low in the region of δ so that surface diffusion is faster. Physically, the metal grain might have a very low contact angle with the electrolyte such that gas access is prohibited in this region.

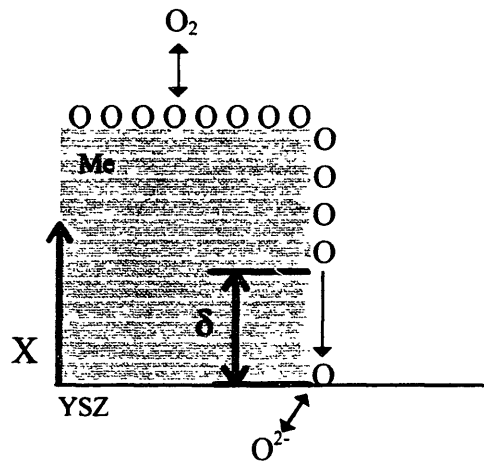


Figure 2.6 Surface diffusion of atomic oxygen adsorbed on metal particle.

At any distance from the triple-phase boundary beyond δ , the adsorption equilibrium holds, and therefore the surface coverage of oxygen atoms is in equilibrium with the gas phase,

$\theta - \theta_{eq} = \Delta\theta = 0$. Hence, the first boundary condition becomes:

$$\Delta\theta_{(x=\delta)} = 0 \quad (2.21)$$

The current at the triple-phase boundary gives rise to a constant-flux boundary condition:

$$i_f = -2FD\Gamma \left(\frac{d\Delta\theta}{dx} \right)_{x=0} \quad (2.22)$$

Γ is the oxygen activity when the fraction of surface coverage equals 1. D is the diffusion constant for oxygen. Using (2.21) and (2.22), a solution to Fick's 2nd law can be found [Gabrielli 1984]. Using this, $\Delta\theta/\Delta i_f$ is evaluated and Z_{mt} is obtained from equation (2.19).

$$Z_{mt} = \frac{RT}{4F^2 D \Gamma \theta_{eq} (1 - \theta_{eq})} \frac{\tanh\left(\delta \sqrt{\frac{j\omega}{D}}\right)}{\sqrt{\frac{j\omega}{D}}} \quad (2.23)$$

At high frequencies ($\omega = 2\pi f$) the phase angle of Z_{mt} is 45° . As the frequency decreases the impedance will resemble a resistor in parallel with a capacitor. However, if the diffusion distance δ is large enough in comparison to the diffusion coefficient D , the transport process approaches the case of diffusion in a semi-infinite media, and the 45° phase angle is maintained at lower frequencies (this is a classic Warburg impedance). This is rarely encountered in YSZ / metal systems, and the 45° phase angle is only encountered at high frequencies. A series expansion for $\tanh(s)$ reveals that the function will equal its argument s when s goes to zero. Hence, at low frequencies (generally if $j\omega/D \ll 3$), Z_{mt} will equal its real part. Using equation (2.12), the P_{O_2} dependency is estimated:

At low coverage ($1 - \theta_{eq} \approx 1$):

$$Z_{mt(\omega \rightarrow 0)} = R_{D0} = \frac{RT\delta}{4F^2 D \Gamma K_{diss} (P_{O_2})^{1/2}} \quad (2.24)$$

At high coverage ($\theta_{eq} \approx 1$):

$$Z_{mt(\omega \rightarrow 0)} = R_{D0} = \frac{RT\delta}{4F^2 D \Gamma K_{diss} (P_{O_2})^{-1/2}} \quad (2.25)$$

Interfacial diffusion in the metal/YSZ -2 phase region (step 5 in figure 2.3)

In the preceding two cases (steps 3 and 4) the charge-transfer kinetics is much faster than the mass-transport step. For a cathodic current, this would mean that any oxygen arriving at the triple-phase boundary is consumed immediately. There is no lack of reaction sites, and most of the charge-transfer reaction is located near the triple-phase-boundary region. If the charge transfer were not infinitely fast compared to steps 3 and 4, there would be a pile-up of oxygen near the three phase interface (figure 2.7a) Wang and Nowick proposed that, in the case of comparable charge-transfer and mass-transport rates, oxygen atoms would diffuse through the 2-phase region of the YSZ/metal interface, and thereby extend the reaction zone as shown in figure 2.7b [Wang 1979].

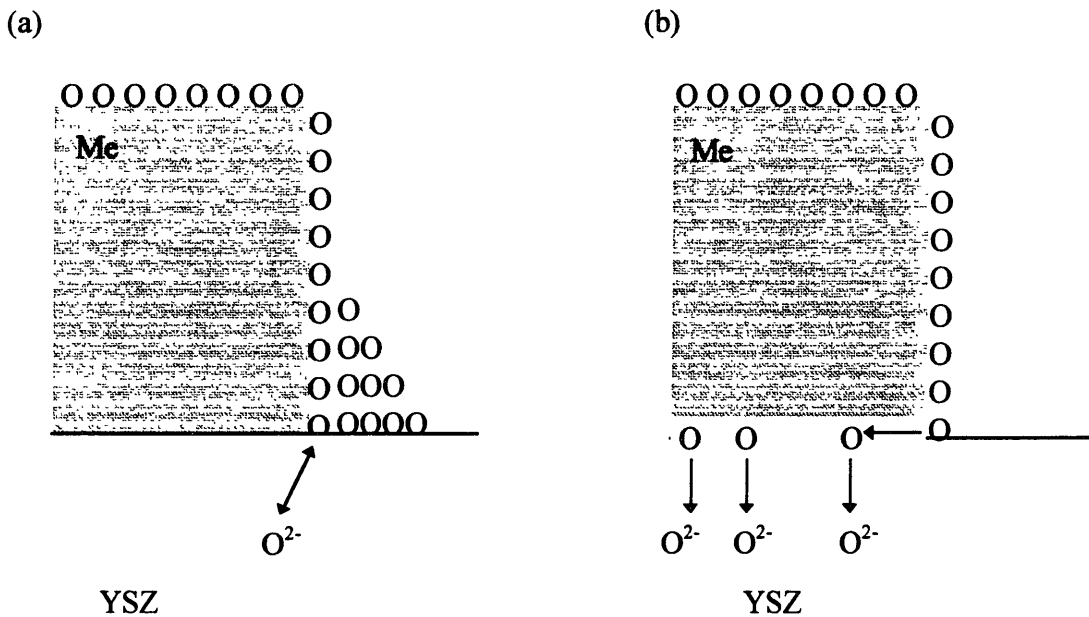


Figure 2.7 Mass-transport rate is comparable to charge-transfer rate.
(a) Pile up at the interface, (b) Interfacial diffusion model by Wang and Nowick [Wang 1979] (dotted region represents the YSZ/metal interface).

An expression for the impedance, based on the competitive interfacial diffusion/charge transfer process, is shown in equation (2.26) [Franceschetti 1989]. The derivation was made with the assumption that the contacts between YSZ and metal grains are rectangular strips with widths of $2L$ (figure 2.8). k is a kinetic rate constant and D is the diffusion constant for oxygen in the 2-phase region.

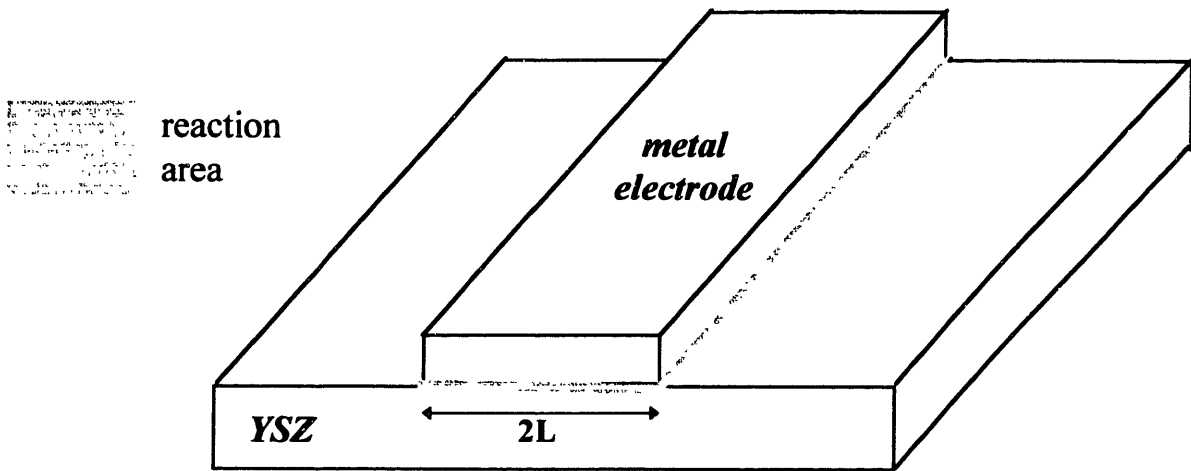


Figure 2.8. The two-phase reaction zone.

$$Z_f = \frac{R_{ct} \left(1 + \frac{j\omega}{k} \right)}{\left(\frac{j\omega}{k} + \left(\sqrt{\frac{kL^2}{D} \left(1 + \frac{j\omega}{k} \right)} \coth \left(\sqrt{\frac{kL^2}{D} \left(1 + \frac{j\omega}{k} \right)} \right) \right)^{-1} \right)} \quad (2.26)$$

Equation (2.26) includes the combined contribution of the mass transport and charge transfer. The complex nature of the impedance makes it hard to break down the expression into discrete components. At high frequencies however, Z_f will approach R_{ct} . Also, when the ratio L^2/D gets smaller, the diffusion will be faster, and Z_f will approach

R_{ct} . Thus when the metal particle size is small enough, the contribution of lateral diffusion will be negligible.

2.3 The Effect of Oxygen on Platinum

Pt is known for its resistance to oxidation. Figure 2.9 shows a plot of the Gibbs free energy for a number of platinum oxides with various stoichiometries as a function of temperature. The data for this plot is taken from *The Oxide Handbook* [Samsonov 1982].

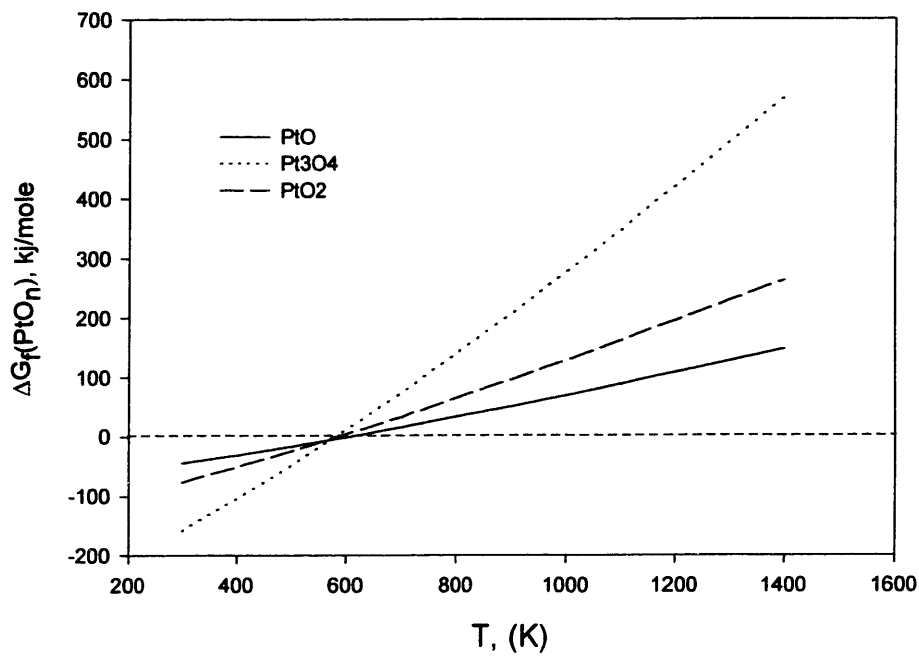


Figure 2.9. ΔG of formation of PtO_n in 1 atm O_2 vs. T .

The graphs represent the formation of oxides in pure oxygen at 1 atm total pressure. None of the oxides are thermodynamically stable above 300°C, and it is likely that their nucleation will be kinetically impaired below 300°C. These oxides can therefore be

assumed to be non-existent in the temperature and pressure conditions at which YSZ-based devices operate.

Even though Pt is resistant towards bulk oxidation, there is, in surface science and catalysis literature, enough evidence to suggest that Pt is not entirely inert with respect to forming interfacial and surface compounds with oxygen. The study of the oxygen-containing species present on Pt surfaces at high temperatures (above 400°C) is difficult; these species are either unstable or metastable at room temperature. In most cases, their study can be done only by *in-situ* investigations at high temperatures. The experimental evidence on the state of oxygen at the O₂/Pt/YSZ interfaces provided by surface science and catalytic studies points to the existence of distinct types of oxygen bonding on Pt surfaces.

Gland [Gland 1980A, Gland 1980B] studied the interaction of Pt single crystals (Pt(111)) with oxygen over a wide temperature range (-173 to 1127°C). He used *in situ* spectroscopic techniques (EELS, UPS, TDS, XPS and AES) and identified three states of oxygen on the Pt (111) surface: (1) below -100°C, adsorbed molecular oxygen predominates with a desorption heat of 37 kJ/mole. The primary bond between the Pt surface and molecular oxygen is formed by electron transfer from the valence band of Platinum into orbitals derived from the antibonding π orbitals of the adsorbed molecules. The layer is fairly mobile. (2) between -123°C and about 427°C, adsorbed atomic oxygen predominates but is present at higher temperatures as well. Saturation of the Pt(111) surface with atomic oxygen yields a layer containing about 10¹⁴ atoms/cm². At low coverage, LEED (low energy electron diffraction) shows an island growth mechanism for

the ordered oxygen phase. The heat of adsorption varies with coverage. It is around 500 kJ/mole at a coverage of $\theta = 0.02$, and 160 kJ/mole at $\theta = 0.8$. (3) at higher temperatures, between 527 and 827°C, a *subsurface* oxygen is present. The decomposition of this oxide begins near 977°C and the process is limited by mass transfer. The authors were not able to extract decomposition heats.

Samorjai [Samorjai 1981] reported that the thermal desorption of oxygen from a Pt crystal surface (12,9,8) has two maxima, one at 700-800°C and the other at 950-1000°C. The heat of adsorption of the strongly bound oxygen was estimated to be 270kJ/mol.

Kuzin and Komarov (Kuzin 1990) studied the adsorption of oxygen on porous Pt electrodes between 552 and 758°C, and found two states of oxygen: a weakly bound adsorbed state and a strongly bound one.

Chao *et al.* (Chao 1991) studied the electrochemical formation of Pt oxide at 477 °C through cyclic voltametry, and found a peak that they assigned to PtO_x formed during the anodic scan.

Stable Pt-O compounds have been found by several investigators [Berry 1982, Vayenas 1982, Velle 1991]. The stoichiometry for these oxides has not been established. The free energy diagrams for these oxides are shown in figure 2.10. The compound reported by Velle *et al.* [Velle 1991] is stable up to 800°C . It is very likely that these compounds will be present under oxidizing conditions near or at the Pt/YSZ interface.

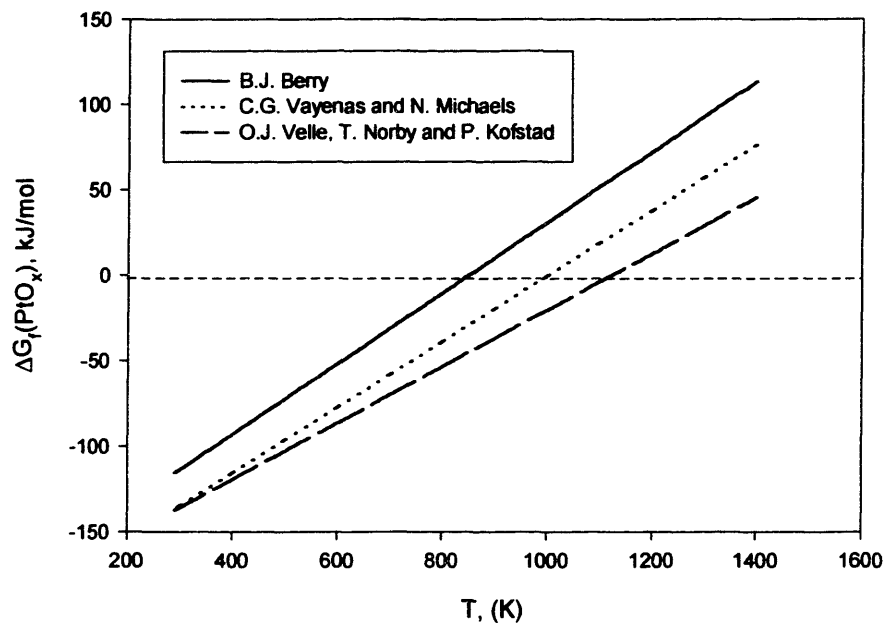


Figure 2.10. ΔG of formation of PtO_x in 1 atm O_2 vs. T .

2.4 The Effect of Oxygen on Palladium

Pd differs from Pt in that a stable oxide (PdO) is present in a wide P_{O_2} and temperature range, as shown in figure 2.11.

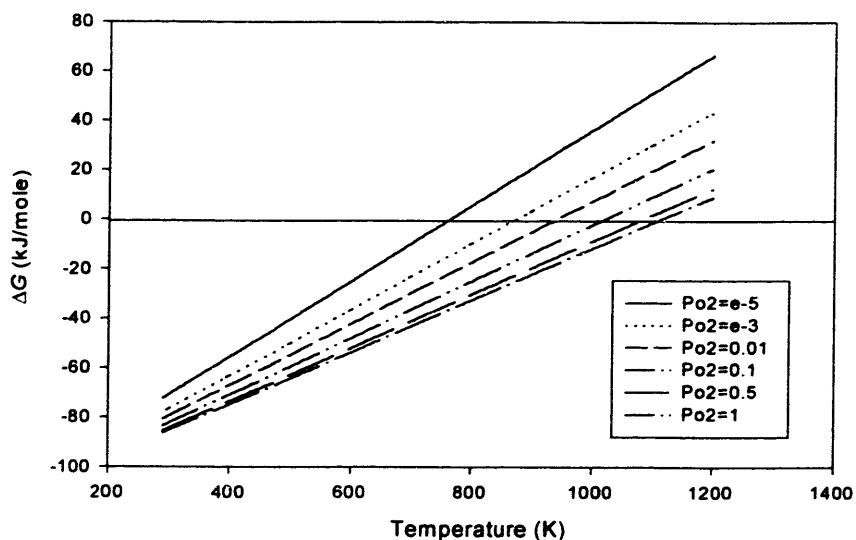


Figure 2.11 ΔG of formation of PdO vs. temperature at various P_{O_2} . (calculated from *Thermochemical Data of Pure Substances*) [Barin 1993])

The kinetics of Pd oxidation has been reported by Duval [Duval 1963]. In air Pd oxidation starts above 364°C, and decomposes above 830°C. Kodas *et al.* [Kodas 1997] investigated the isothermal oxidation kinetics of Pd powders in air in the temperature range, 600 - 675°C. They found that the conversion was initially from Pd to a substoichiometric PdO. The substoichiometric PdO then converted to Pd^{II}O. The substoichiometric oxide was preceded by chemisorption and diffusion. Pure Pd reacted topochemically and the reaction rate was limited by the oxygen diffusion through the substoichiometric oxide layer.

Doping the Pd powders with Ca increased the oxidation resistance by inhibiting oxygen diffusion through the oxide layer.

2.5 Role of Interfacial Oxygen Containing Species in the Oxygen Exchange Process at the Metal/YSZ Interface

As discussed in the previous section, it is possible that oxygen may react with Pd or Pt at the surface to form compounds of varying stability. For Pd there exists a definite oxide whereas, for Pt, there exists a range of compounds: from loosely adsorbed oxygen to Pt-oxides (section 2.3). Any type of oxygen bonded to the metal will henceforth be denoted, *oxygen-containing species* or OCS.

The OCS may form from oxygen supplied from the atmosphere (see figure 2.12 a) or from an anodic current (see figure 2.12 b).

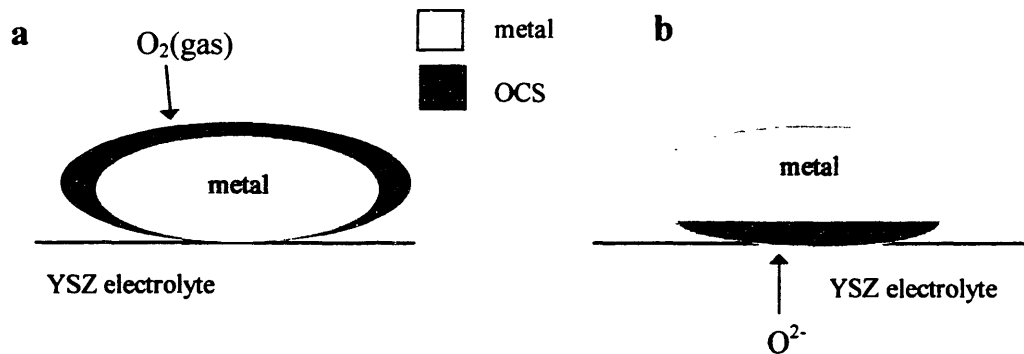


Figure 2.12. OCS formation
a) from gaseous oxygen
b) oxygen supplied through the electrolyte

As shown in figure 2.1, the oxygen-transfer reaction takes place at or near the triple-phase boundary (TPB). When OCS is present at the TPB, it may block the reaction if it is insulating with respect to ions as well as electrons (see figure 2.13 a). Electrically, the

interface would be represented by a capacitor. On the other hand, it may only be partially blocking. The OCS may then act as an intermediate step in the charge-transfer process (see figure 2.13 b). This is likely if the OCS consist of oxygen loosely bonded to the metal surface. In this case, the interfacial process is associated electrically with an impedance Z_{ocs} .

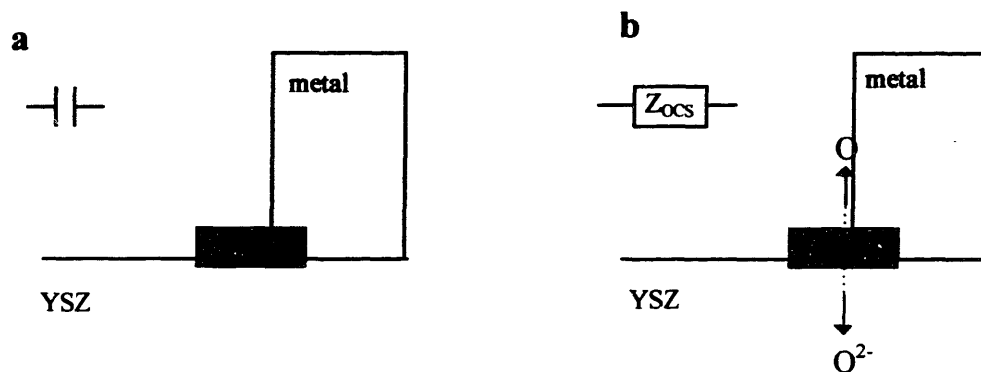


Figure 2.13 The presence of OCS at the TPB.

The magnitude of Z_{ocs} depends on the strength of the me-O bonds that needs to be broken or established in the oxygen-transfer process. TPB sites covered with OCS may coexist with clean TPB sites. Under such circumstances two paths may exist for oxygen transfer: one through the OCS (figure 2.13 b) and another at the OCS-free TPB sites (figure 2.1). The paths can be envisaged as being in parallel, as shown in figure 2.3 (dotted and solid lines). The contribution of each path depends on the extent of OCS coverage at the TPB. The area in equation 2.3 is a function of the length of the triple-phase boundary. This term is therefore dependent on the OCS concentration at the TPB.

Chapter 3

Experimental Approach and Data Analysis

The electrochemical measurements were made in two different experimental configurations. A single-compartment cell and a lab-scale-fuel cell configuration, with separated gas compartments. Under specific thermodynamic conditions, oxygen-containing species (OCS) are stable on the metal surface. This work investigates how the presence of these species at the charge-transfer sites affect the oxygen-exchange reaction. The stability of the OCS are sensitive to the local oxygen potential at the charge-transfer sites. Hence, the effect of current on the exchange reactions at Pt/YSZ and Pd/YSZ is extensively studied and the results are reported in chapters 5 and 6. All the results reported in these chapters were obtained using the single-compartment cell. The lab-scale fuel cell configuration was used in the steam reforming experiments reported in chapter 4 where the existence of OCS was first observed.

3.1. Experimental Configuration for the Study of Electrode Reactions

The experimental setup for studying interfacial impedance is shown below in figure 3.1. The high-temperature cell was placed inside an alumina tube sealed with McDaniel caps. This entire assembly was placed inside a resistance-heated Lindbergh furnace with a 12" hot zone. Care was taken so that the cell was placed in the middle of the hot zone of the furnace.

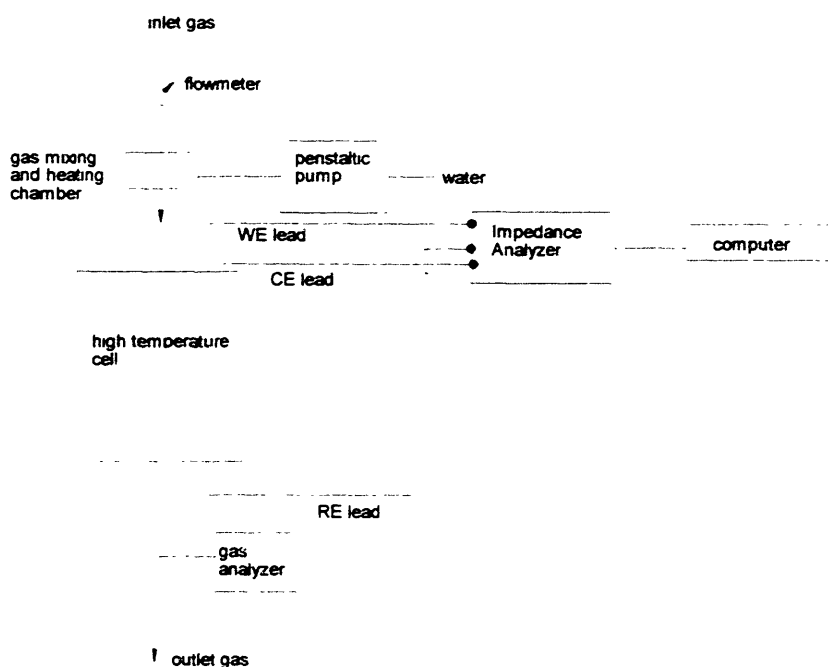


Figure 3.1. The experimental setup for 3-electrode impedance measurement of a YSZ/electrode interface.

Gas flowrates were selected such that the gases would reach furnace temperature at the beginning of the hot zone and would not alter the temperature of the cell. The inlet gases were set by calibrated flowmeters supplied by Alborgh and Matheson. When steam was used in the inlet gas, liquid water was introduced into a heated chamber (kept at 120°C)

with the use of a peristaltic pump. The vaporized water was mixed with the other gases in this heated chamber before being introduced into the furnace. An AMETEK Quadrupole mass-spectrometer was used to monitor the composition of the outgoing gases.

The working (WE) and counter (CE) electrodes were placed on opposite sides of the electrolyte disc, and the reference electrode (RE) was painted on the edge. The reference electrode consisted of Pt-ink supplied by Engelhard. After coating and drying, of the reference electrode it was fired in air at 900°C for 1.5 hours. The minimum distance between RE - WE and RE - CE, respectively, was 2 mm. The electrode configuration is shown in figure 3.2.

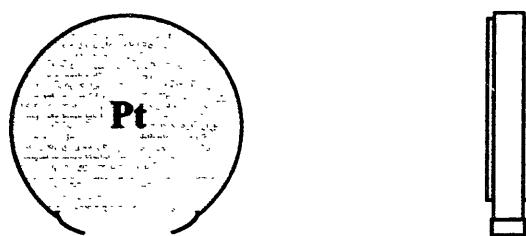


Figure 3.2. The electrode/YSZ/electrode cell.

A cross section of the high-temperature cell is shown in figure 3.3. The contacts between the electrodes and lead wires were achieved by platinum gauze pressed on the electrodes by alumina wedges. This configuration maintained a good electrical contact and permitted free access of the gas phase to the electrodes, while allowing for thermal expansion. The electrode connections are shown in figure 3.4.

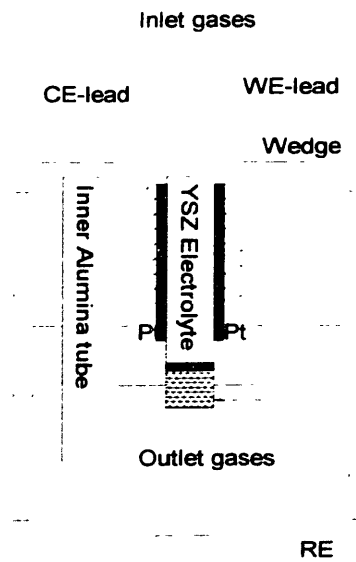


Figure 3.3. Cross section of the high-temperature cell assembly.

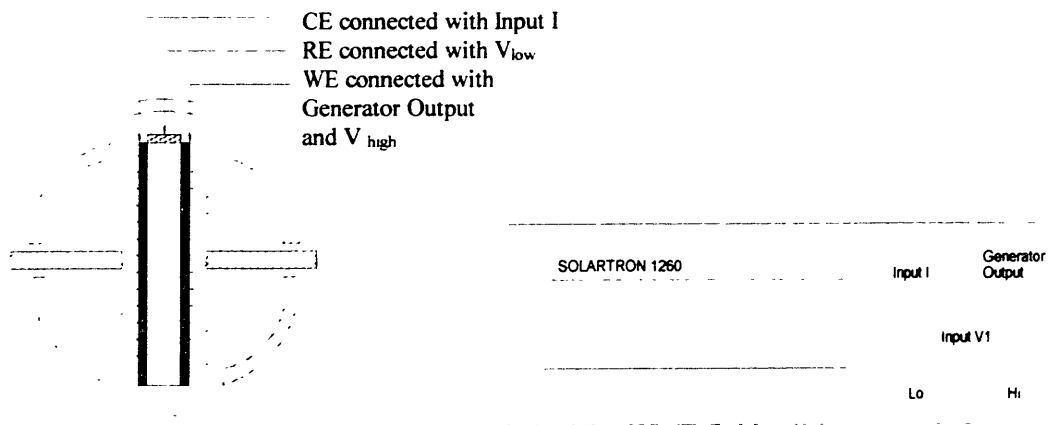


Figure 3.4. The high-temperature cell and the connections of the electrodes to the terminals of the Solartron 1260.

3.1.1. Electrochemical Impedance Spectroscopy (EIS)

The principle of EIS is to perturb the cell with an alternating electrical signal of small magnitude and then follow the response of the system as a function of the signal over a range of frequencies. The main assumption made is that the system reacts linearly to the perturbation. The impedance resulting from the linear I - V relationship (see appendix I) consists of an imaginary and a real part:

$$Z = a + bi \quad (3.1)$$

Or in polar form:

$$Z = |Z|e^{i\phi} \quad (3.2)$$

Here ϕ is the phase angle. This can be represented in a *phasor* diagram as shown in figure 3.5 below.

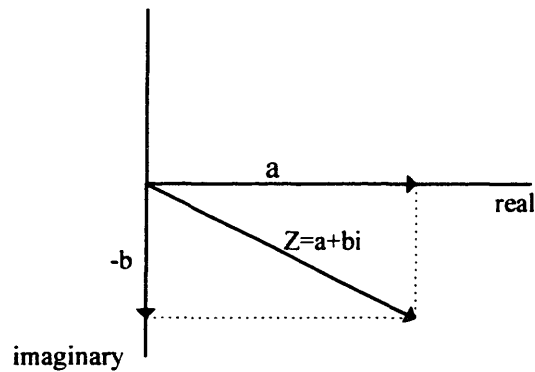


Figure 3.5. Phasor diagram representing the impedance.

The nature of the response makes it suitable to use electrical analogies to interpret the impedance of an electrochemical cell. As an idealized model, interfaces with charged double layers can be seen as capacitors, and transport processes within the bulk electrolyte

and electrodes as resistors. Less obviously, the activation barrier for interfacial charge transfer can be represented [Bard 1980] as a resistor. In the absence of mass-transfer limitations, the charge-transfer resistance can be derived from a differentiation of the Butler-Volmer equation:

$$\frac{\partial I}{\partial V} = I_0 \left(\frac{nF}{RT} \right) \left[(1 - \alpha) \exp \left[\frac{(1 - \alpha)nF\eta}{RT} \right] + \alpha \exp \left[\frac{-\alpha nF\eta}{RT} \right] \right] \quad (3.3)$$

For small perturbations, the overpotential η can be expected to be small, and equation (3.3) reduces to:

$$R_{ct} = \frac{\partial I}{\partial V} = I_0 \left(\frac{nF}{RT} \right) \quad (3.4)$$

Since the exchange current is generally assumed to be a constant, the impedance associated with charge-transfer activation can be modeled as a resistor (figure 3.6).

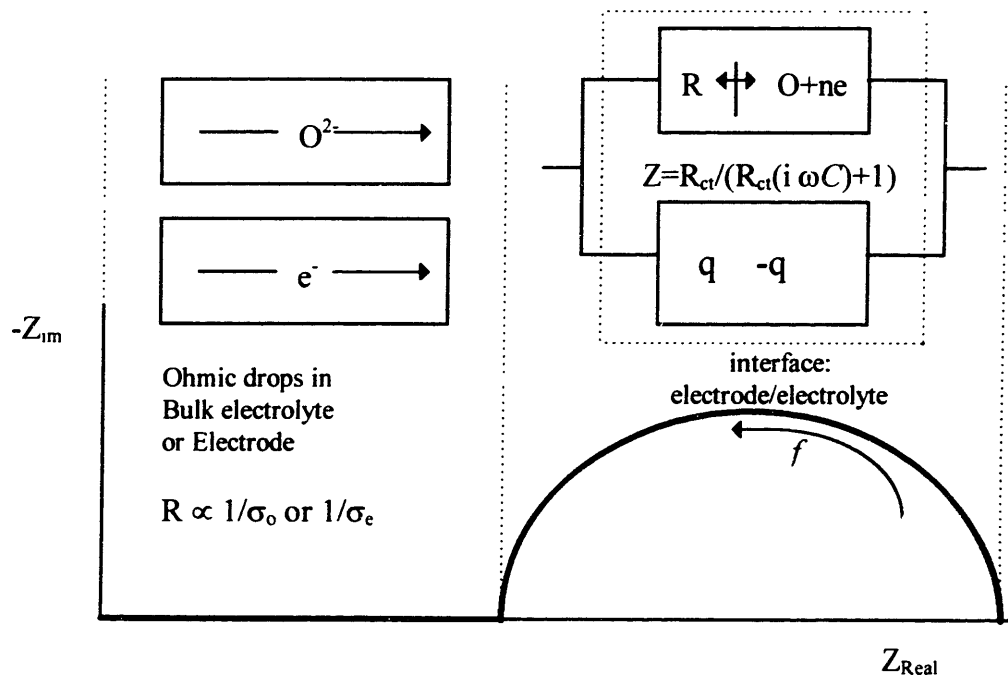


Figure 3.6. Link between an electrochemical halfcell and the complex impedance.

An ideal electrochemical interface can thus be seen as a charge-transfer resistance R_{ct} (*faradaic*) in parallel with a double layer capacitance C_{DL} (*non-faradaic*) as shown in figure 3.6. Here the phase angle will vary with frequency and hence at low frequencies C_{DL} will be shorted whereas at high frequencies R_{ct} will be shorted.

A lot of information on solid electrolytes as well as electrode/electrolyte interfaces can be gathered this way. The use of EIS to characterize systems with YSZ electrolytes was first done by J.E. Bauerle [Bauerle 1969]. He found three contributions to the impedance of the cell: an electrode polarization characterized by a double layer capacitance and a charge-transfer resistance, a capacitive-resistive electrolyte impedance, and a pure ohmic-electrolyte resistance.

3.1.1.1. The Experimental Procedure for the Study of Interface Reactions with EIS

A three - electrode system was used, in order to isolate the impedance response of a single electrode/electrolyte interface. The experimental setup is shown in figure 3.1. The EIS was carried out with a Solartron 1260 Impedance Analyzer controlled by the Z60 software written by Scribner Associates. The spectra were measured mostly in the voltage - control mode. The ac amplitude was 30 mV. Linearity checks were done for the operating conditions prior to all experiments. This was done in the *sweep voltage:amplitude* mode between 0.005 and 0.05V at 10,000Hz, 1Hz, and 0.01 Hz. The sweeps were always done from high to low frequency. This proved to be essential, especially in dynamic situations when the spectra had to be taken fast.

The interfaces under study were placed in gas mixtures of known P_{O_2} and were monitored until a steady state, as seen by EIS, was reached. After observing a stable spectrum for a given P_{O_2} , a current of 10 mA was passed for 10 minutes. While a current passes, the WE functions either as a cathode or an anode, depending on the direction of the current. Impedance spectra were taken, between the WE and RE, continuously during the current flow and at short intervals after current interruption. The frequency response of the interface was thus monitored in the time domain. Since the object of most measurements in the time domain was to study the dynamic nature of the interface, the spectra had to be taken at short intervals. However, the study of electrode reactions inhibited us from limiting the spectra to too high frequencies (the low frequency values naturally take longer time). The following conditions were found to be optimal for the time-domain measurements:

Table 3.1. Conditions for time-domain measurements.

High f (Hz)	Low f (Hz)	generator amplitude (V)	logarithmic sweep steps/decade	delay time	integration cycle	time for spectra (sec)
80	1	0.03	10	0	1	55

Once the spectra reached steady state, the frequency range was expanded to 0.1 or sometimes even 0.01 Hz. Spectra were also taken during current passage in the current-control mode under the following conditions:

Table 3.2 Conditions for measurements in the current-control mode under dc bias.

High f (Hz)	Low f (Hz)	generator amplitude (I)	logarithmic sweep steps/decade	delay time	integration cycle	time for spectra (sec)
80	0.1	0.02	10	0	1	55

The monitor was, in this case, activated for 0.02 V, and an appropriate current bias was on. The low-frequency measurements were in this case mostly limited by the time that the current bias needed to be passed.

3.1.1.2. Interpretation of the Impedance Spectra for the Metal/YSZ Interface

A major part of the data analysis and modeling was the deconvolution and equivalent-circuit fitting of the impedance data. Most of the impedance spectra for the electrode/electrolyte interfaces had the characteristics of figure 3.7:

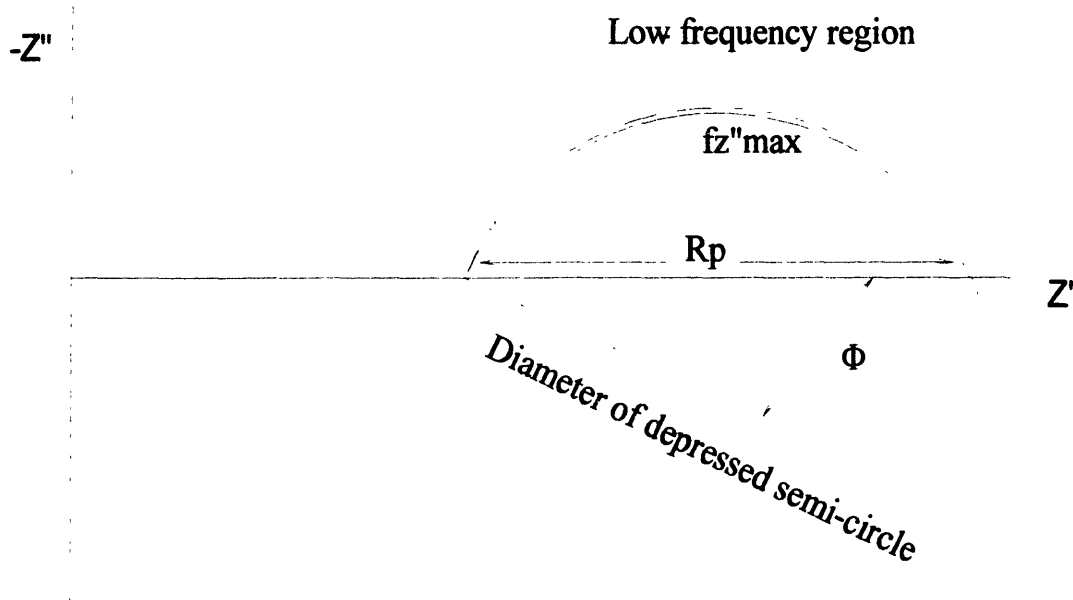


Figure 3.7. Typical spectra of the Pt/YSZ interface.

The high-frequency intercept was assigned to the ohmic drop between the reference electrode and the working electrode. The inductive tail beyond this intercept was assigned to the leadwires. The low frequency arc included the lumped response of all the electrode processes at the working electrode. It was constituted of a single (as in figure 3.7) or several depressed semi-circles. Depressed semicircles are frequently encountered in the literature [Christensen 1994, ASTM]. The depressions were not large enough to cause a notable difference between the R_p from the real axis intercepts and the diameter of the depressed semi-circle.

The low frequency part of the impedance spectra for the electrode/electrolyte interfaces were interpreted in 2 stages.

Initially, before the physical phenomena had been mapped, certain features of the spectra were extracted and compared. The following characteristics were chosen:

R_p : The difference between the low and high frequency intercepts of the low frequency arc was taken as a characteristic value for the summed resistance of the electrode processes.

$f_{Z_{\max}}$: The maximum component of the low frequency arc is related to the relaxation time of the lumped response. Its value should be characteristic for the types of electrode processes that occur.

Equivalent-circuit fitting was done using *Zview*, which is a CNLS (Complex Nonlinear Least Square) fitting software provided by Scribner Associates. Due to the small (but not non-existent) depression angles, distributed elements (DE) had to be used in most cases. The DE named ZARC was found to model the spectra most appropriately. ZARC produces a complex plane impedance curve which forms an arc of a circle with the center displaced from the real axis. The ZARC can be seen as a constant phase element (CPE) in parallel with a resistor (figure 3.8):

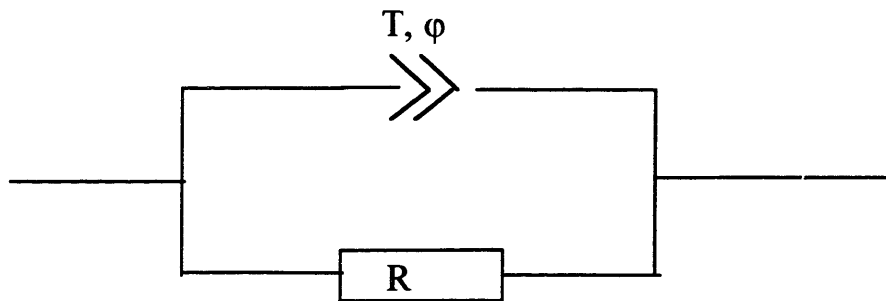


Figure 3.8 The ZARC element.

The mathematical formula for ZARC is:

$$Z = \frac{R}{1 + RT(i\omega)^\varphi} \quad (3.5)$$

The smaller the value for φ , the more the center is displaced, i.e., a value of 1 would result in a pure *RC* parallel circuit.

3.1.2. Gas Analysis

The outlet gases were sampled in an AMETEK quadrupole M200 residual gas analyzer (mass-spectrometer). It was operated mainly in the tabular mode and in each scan the following gases were analyzed: CO, CO₂, Ar, CH₄, O₂ and H₂O. The dwell time (time allotted for each sample) was kept at 60 msec.

3.2. Experimental Configuration for Study Conducted under Fuel Cell Conditions

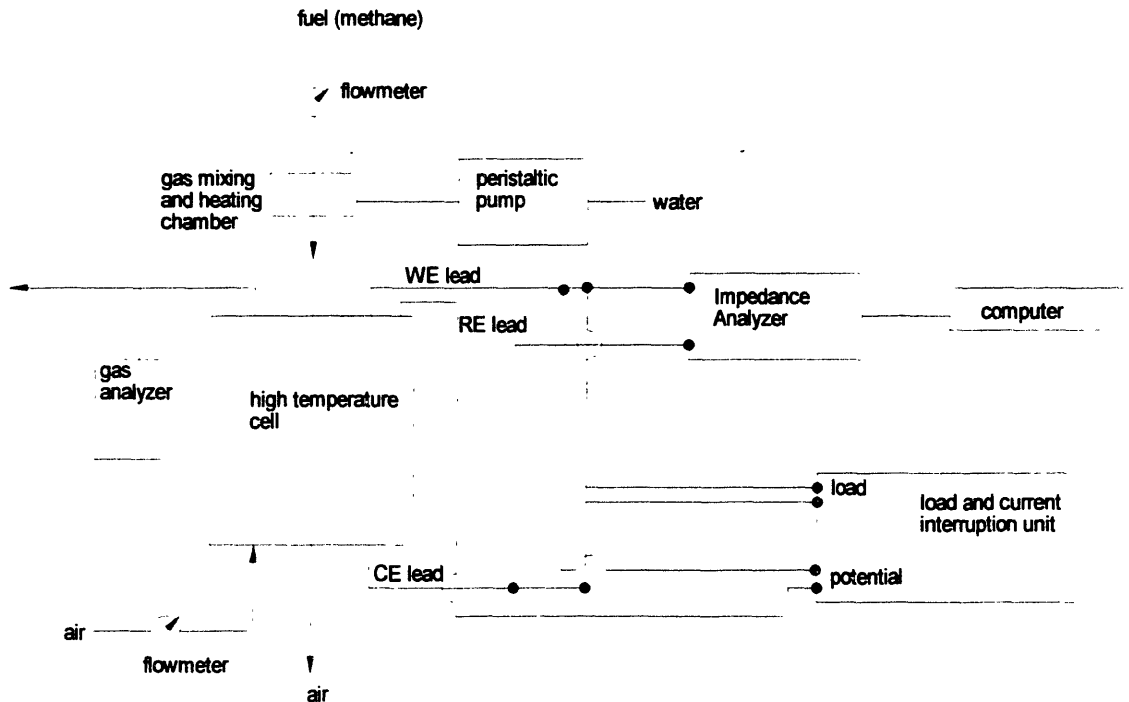


Figure 3.9. The experimental setup for the laboratory-scale fuel cell.

Figure 3.9 shows the experimental configuration of the fuel cell. The cell was positioned in the middle of the hot zone of the furnace tube of a gas-tight Lindbergh resistance furnace. The total length of the hot zone was 12". A 855-25W fuel cell-test-load system equipped with a current interrupter and a 1260 Impedance Analyzer was connected between the working electrode (WE) and the counter electrode (CE) of the cell. In order to isolate the anodic and cathodic compartments, the cell was mounted on top of a 3/4" OD alumina tube, as shown in figure 3.10. The cell was sealed to this tube with a high temperature sealant, AREMCO Ceramabond 516, which has a thermal

expansion coefficient intermediate between that of zirconia and alumina. In order to achieve an adequate seal, several seal layers had to be applied. The seal was then dried at 90°C for 5 hours followed by a 2 hour heat treatment at 200°C intervals up to the experimental temperature. The seal did not hold while cooling the cell, and therefore the seal had to be reapplied every time the cell was heated from room temperature. The area inside the inner alumina tube was the cathodic compartment (figure 3.10).

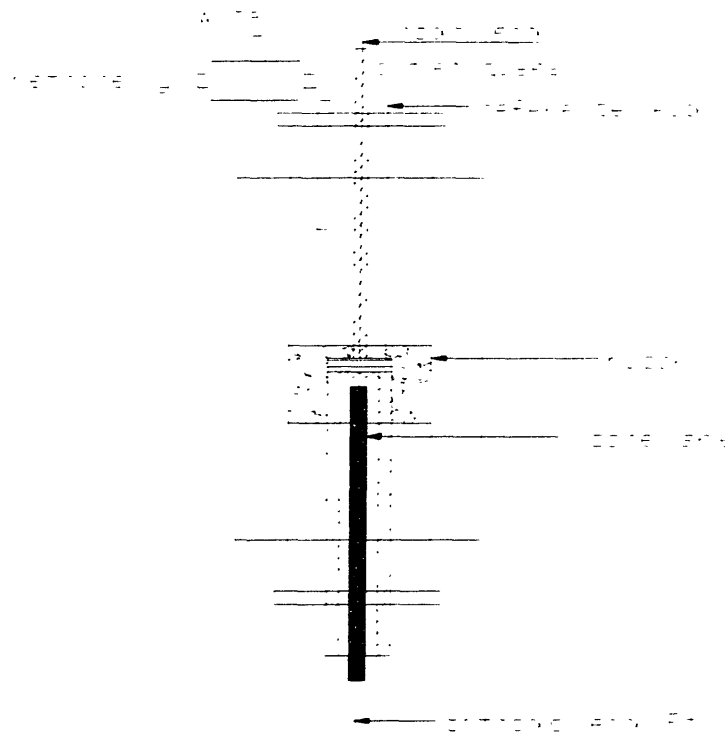


Figure 3.10. Separated compartments of the fuel cell.

A ceramic weight was placed on top of the cell in order to press the contact gauze (Pt or Ni) and the reference electrode (Pt) to the anode. The configuration of the

electrodes are shown in figure 3.11. At the cathode, the contact to the electrode was made with a Pt-gauze. In order to minimize contact resistance, the cathodic contact was spring-loaded to the electrode.

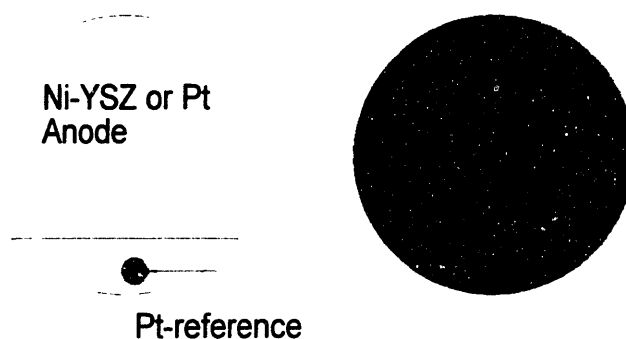


Figure 3.11. Electrode configuration.

The anodic gas mixtures were prepared in a heated mixing chamber. The inlet gases were set by calibrated flowmeters supplied by Alborgh and Matheson. When steam was used in the inlet gas, liquid water was introduced into a heated chamber (kept at 120°C) with the use of a peristaltic pump. The vaporized water was mixed with the other gases in this heated chamber before being introduced directly into the hot zone of the furnace. This was done in order to avoid any carbon deposition outside the hot zone. An AMETEK Quadrupole mass-spectrometer was used to monitor the composition of the outgoing anodic gases. The anodic fuel gases that were used were $\text{CH}_4/\text{H}_2\text{O}$, CO/CO_2 , H_2/CO_2 , and H_2/N_2 . Compressed air was used as the oxidant gas in the cathodic compartment. All gases were provided by BOC.

3.2.1. Electrochemical Impedance Spectroscopy

Electrochemical impedance spectroscopy was used in a 2-electrode mode to monitor the total impedance of the cell. A 1260 Solatron Impedance Analyzer described in section 3.1.1. and shown in figure 3.3 was used for this purpose. The WE was connected to Generator Output and V-high while the CE was connected to Input I and V-low. Linearity checks were made before any measurements. The impedance had to be measured without a current flow through the cell, since a flow would cause deviation from the I - V linearity. To achieve this, the impedance was operated in two different modes:

- a) The impedance spectra was measured during a potential bias that was applied to counter the Nernstian EMF of the cell.
- b) The impedance spectra was measured in the current-control mode with a zero bias to block any current passage through the cell.

Generally the second method b) was found to work better since it was impossible to compensate exactly for the EMF, and thus it could not be made sure that no current leaked. The total impedance response of the cell and leads consists of the elements in figure 3.12.

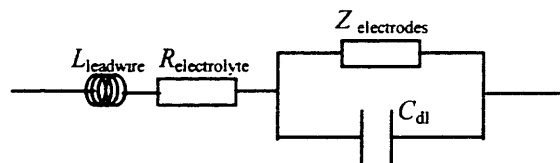


Figure 3.12. Electrical circuit for the impedance of the overall cell and leads.

3.2.2. Current Interruption

In solid electrolytes the ohmic losses are large enough to cause inaccuracies in overpotential measurements with potentiostatic control. The current-interruption technique, also known as the indirect method, eliminates the problems with ohmic losses.

The method involves a galvanostatic control, and current is allowed to flow long enough such that steady state is established. The current is then interrupted and the potential between the working and reference electrode is measured within 10^{-6} seconds after current interruption. The overpotential decay that follows the current interruption can be explained through figure 3.13. Here Z_f represents the faradaic impedance at the working electrode (WE), R_{WE} the ohmic drop at the WE, R_{E1} the ohmic drop between the reference electrode (RE) and WE and R_{E2} the ohmic drop between RE and the counter electrode. The ohmic contributions R_{WE} , R_{E1} and R_{E2} will disappear in less than 10^{-12} seconds [Jeager 1972]. After current interruption the potential across Z_f is same as the potential before interruption because the current is supplied by the electrode/electrolyte double layer C_d and it corresponds to the electrode overpotential η . The potential accordingly decays after current interruption as the double layer discharges as shown in figure 3.14. Assuming that steady state was reached prior to current interruption i.e. $(d\eta/dt)_b = 0$, the initial rate of decay is given by:

$$\left(\frac{d\eta}{dt}\right)_0 = \frac{i}{C_d} \quad (3.5)$$

The potential therefore decays linearly with time and, by extrapolating the decay to zero time, the overpotential corresponding to a certain steady-state current is evaluated.

The instrument used for the current-interruption measurements was a 855-25W Fuel cell load, supplied by Scribner Associates, equipped with a fast current interrupter and voltage meter. The cell current was controlled by the variable load ($25\text{m}\Omega$ - $10^6\Omega$).

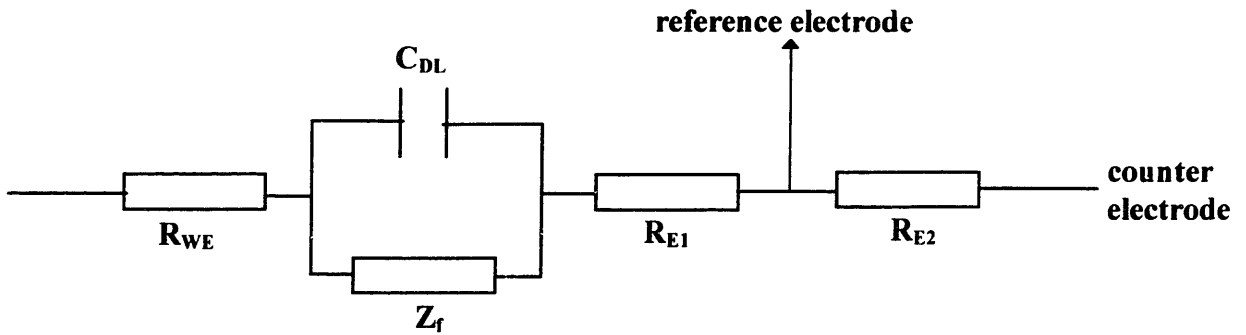


Figure 3.13. Principle of current interruption.

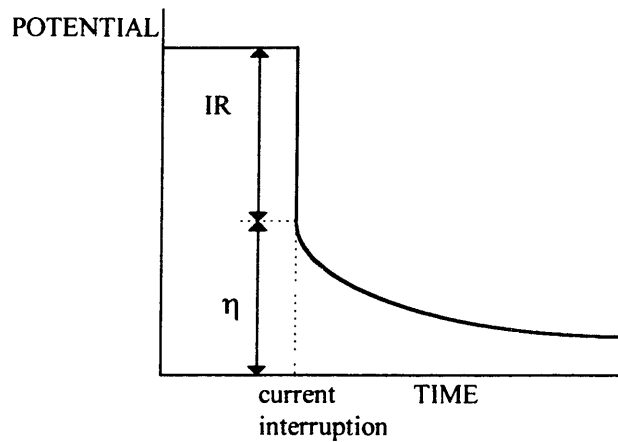


Figure 3.14. Over-potential decay after current interruption.

3.2.3. Current vs. Voltage Characteristics

The overall cell performance was monitored by measuring the current vs. voltage characteristics between the cathode and anode. Control of the current, and measurement of the voltage, was achieved with the 855-25W Fuel cell load. The cell voltage E_{cell} at a certain steady-state current would equal:

$$E_{Cell} = E_{OCV} - R_{electrolyte} * I + \eta_{anode} (I) + \eta_{cathode} (I) \quad (3.6)$$

The deviation of E_{cell} in equation (3.6) from linearity would reveal the current dependency of the total overpotential of the electrodes. However, the behavior was, in most cases, linear due to the large contribution of $R_{electrolyte}$.

3.2.4. Gas Analysis

An AMETEK gas analyzer was used to monitor the outlet gases. For details see section 3.1.1.

3.3. Electrode Preparation and Characterization

3.3.1 Pt-ink Electrodes

Pt electrodes were prepared with Pt ink supplied by Engelhard: Pt-ink 6926. This material has been recommended in literature [Wang 1979] since it is free of inorganic additives and flux. Before ink application, the electrolyte surfaces were polished and washed in an ultrasonic bath, first with acetone and then with de-ionized water. The

material was stenciled on to the YSZ electrolyte and then left to dry for 24 hrs. It was then fired in air at 900°C for 1.5 hrs, as recommended by the vendor. The microstructure thus produced was close to that reported in the literature [Mizusaki 1987] with a pore size of 2-4µm.

3.3.2 Ni/YSZ electrodes

The procedure for processing Ni/YSZ cermets has been published earlier [Sridhar 1996]. The procedure is described in Appendix I.

3.3.3 Electrolytes

The 1.7 mm thick 1/2" diameter electrolytes were supplied by SIEMENS AG. The ZrO₂ discs were doped with 8mole% Y₂O₃.

Chapter 4

Ni-YSZ/YSZ/Pt Cell - Steam Reforming Studies (detection of current-induced changes in cell - impedance spectra)

The initial observations of the current induced effect on the electrode impedance were made in a laboratory-scale fuel cell. The fuel cell was being used for anodic-internal steam reforming studies. After operating the cell with an external load (i.e. passing a direct current) the near-equilibrium-impedance spectrum was considerably different than the near-equilibrium spectrum before current passage. The seemingly irreversible changes complicated the electrochemical analysis of the current-interruption data since the state of the cell under equilibrium seemed to change depending on how much current had been passed.

This chapter discusses the initial steam-reforming studies. The motivation is not to interpret the electrochemical results but rather to present the conditions under which the current-induced-impedance change was first observed. The results in this chapter are obtained for a working solid oxide fuel cell (SOFC). It therefore emphasizes the application of the results and conclusions of this thesis to SOFC.

4.1 Surface Area Characterization of the Ni-YSZ Cermets

Four different cermets were chosen for the steam-reforming studies (Table 4.1). The processing of the Ni-YSZ cermets are described in appendix I. The objective was to establish the effect of Ni content and Ni-grain shape on internal steam reforming. Steam reforming is a process that is enhanced in the presence of a catalyst. Process kinetics are therefore sensitive to the surface area and composition of the constituents of the Ni-YSZ cermets.

Table 4.1. Ni-YSZ cermet samples.

Sample type	Initial powder composition	Ni - powder type
A	80 weight% Ni	Needle
B	60 weight% Ni	Needle
D	80 weight% Ni	Spheres
E	60 weight% Ni	Spheres

The specific surface areas of the four Ni-YSZ cermets were measured with BET. A relatively large quantity was needed to get an adequate accuracy in the measurements (1 gram). Cermets coated on the YSZ could not be used since the total weight obtained from a porous cermet film on a YSZ disk of 1.5 cm diameter was too little. Therefore, separate batches were prepared on large alumina plates. After processing, the cermets were carefully scraped off so that its structure was preserved to the extent possible. A

QUANTASORB™ was used with Nitrogen as an adsorbate to measure the surface area of the cermets. The total surface area is given by the following expression:

$$S_t = \frac{X_M N A_{cs}}{M} \quad (4.1)$$

N is the Avogadro's number ($6.023 \cdot 10^{26}$), M the molecular weight of nitrogen (28 g/mole), and A_{cs} the surface that an adsorbed N_2 molecule occupies. X_M is the total weight of the adsorbate corresponding to a monolayer, and is calculated from the slope or intercept of a plot depicting the following expression:

$$\frac{1}{X \left(\frac{P_0}{P} - 1 \right)} = \frac{C-1}{X_M C} * \frac{P}{P_0} + \frac{1}{X_M C} \quad (4.2)$$

P is the partial pressure of the adsorbate, P_0 the saturated-partial pressure of the adsorbate, and C a constant related to the enthalpies of adsorption and condensation of the adsorbate. X is a parameter that depends on the weight of the adsorbate and the ratio P/P_0 , and is calculated from the following expression:

$$X = \frac{A}{A_{cal}} V_{cal} \left(\frac{P_a M}{RT} \right) \quad (4.3)$$

Here, A is the sample integrator, P_a the ambient pressure (= 1 atm), and A_{cal} the calibrated integrator. The specific surface area S_c is the total surface area S_t divided by the mass of the sample. The results of the surface-area measurements are shown in table 4.2.

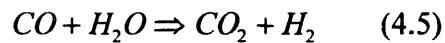
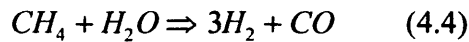
Table 4.2. Results of surface area measurements.

Sample type	Specific surface area, S_c , $m^2 g^{-1}$
A	0.31
B	0.95
D	0.34
E	0.80

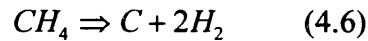
The surface area is higher for B and E (60 wt% Ni) than for A and B (80 wt%Ni). A higher YSZ loading may inhibit the Ni particles from coarsening. Thus, a lower surface area is observed for the Ni - rich samples.

4.2 Internal Steam Reforming and Overall Impedance

Ni is known to be a good catalyst for the steam-reforming reactions due to its ability to adsorb hydrocarbons and cleave C-H bonds [Rostrup-Nielsen 1977, Rostrup-Nielsen 1984]:



Ni is unfortunately also a good catalyst for the coking reaction:



Reaction 4.6 results in solid carbon formation on the catalyst which may lead to catalyst poisoning as well as clogging of the pores. In order to avoid reaction (4.6), the inlet feed ratio of methane to steam needs to be kept low. In the preliminary experiments it was found that coking occurred whenever the ratio of CH₄ to H₂O exceeded 1/4. Table 4.2 shows the composition of the outlet gas for the four different anodes when the inlet gas had a CH₄ to H₂O ratio of 1/4. $f(i)$ denotes the mole fraction of species i .

Table 4.2 Results of gas composition analysis of the outlet gas at 900°C when the inlet gas had a CH₄/H₂O ratio of 1/4.

cermet	A: 80 wt% Ni needles	D: 80 wt% Ni spherical	B: 60 wt% Ni needles	E: 60 wt% Ni spherical
$f(H_2)$	0.62	0.51	0.59	0.55
$f(CH_4)$	0.1	0.3	0.17	0.2
fraction reformed CH ₄	0.74	0.39	0.59	0.56

According to table 4.2, needle-shaped Ni-powder results in a higher degree of reforming especially for the case of high Ni-loading.

Impedance spectroscopy was used to monitor the stability of the cell. An example of the impedance spectra is shown in figure 4.1.

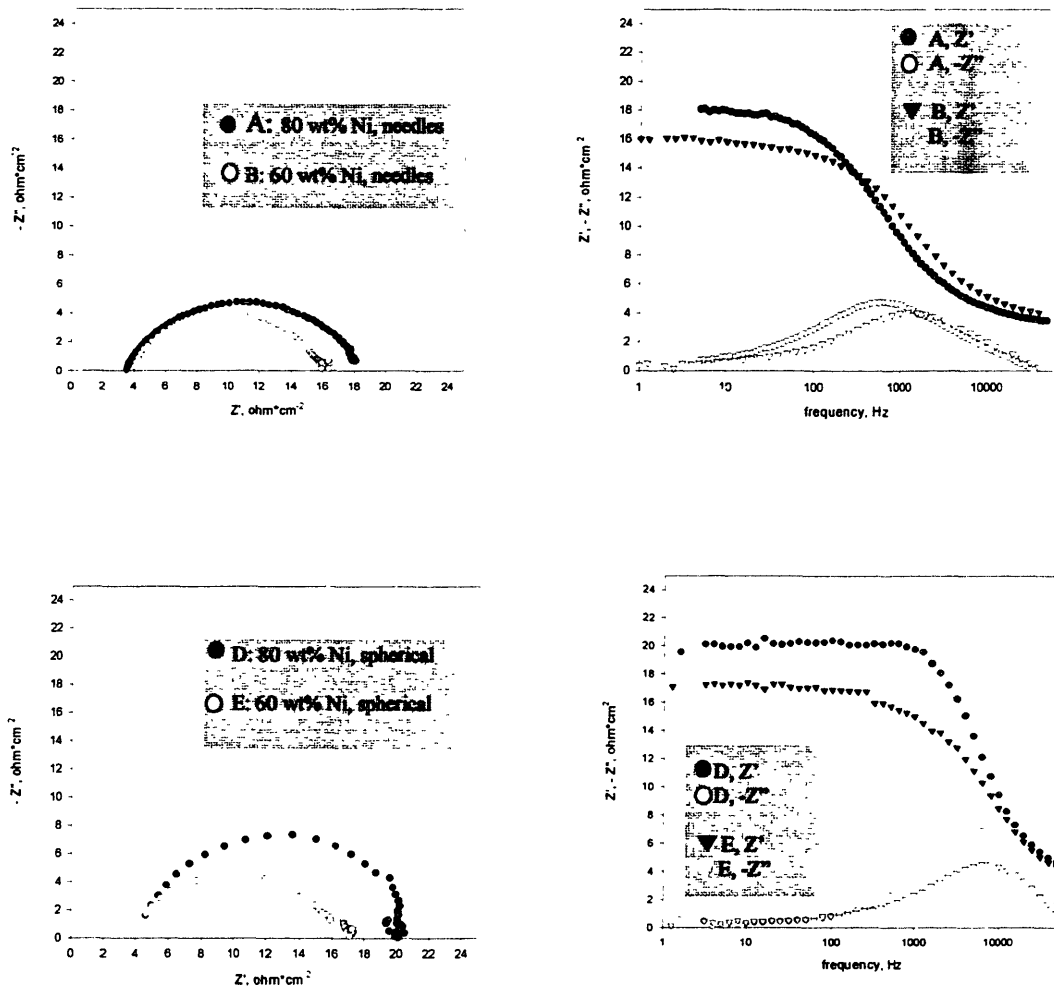


Figure 4.1. Impedance spectra for cells using cermets A,B,D and E.

The figure shows the cole-cole representation as well as a impedance vs. frequency representation of the impedance spectra, for the four different cermets, at 900°C and $\text{CH}_4/\text{H}_2\text{O} = 1/4$. For both types of Ni-grain shape, the overall impedance is smaller for

samples with 60 wt% Ni than with 80 wt% Ni. The reason could be that a higher YSZ loading contributes to a better adherence with the electrolyte and hence improves the interfacial contact, thereby lowering the impedance.

Higher YSZ loading gives better interfacial-reaction kinetics whereas high loading of needle-shaped Ni-grains gives better steam-reforming characteristics. A composite anode that consists of a high Ni (needle-shaped grains) loading at the gas/electrode surface but a high YSZ loading at the electrode/electrolyte interface would optimize both processes. This would also eliminate the thermal mismatch at the electrode/electrolyte interface.

4.3 Cell - Impedance Change after Current Interruption

Current-interruption measurements were done in order to measure the overpotential during a given current flow. The details of the measurement technique are described in chapter 3. An example of the measured polarization vs. current is shown in figure 4.2.

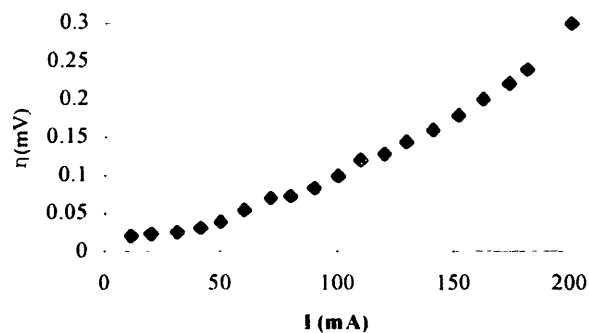


Figure 4.2. Polarization measurements obtained through current interruption for type A cermet (80 wt.%, needles).

It was found that the cell impedance was substantially altered after a current-interruption measurement. A typical example is shown in figure 4.3. The maximum current density that was applied in the measurement was 150 mA / cm^2 and was maintained for 10 minutes.

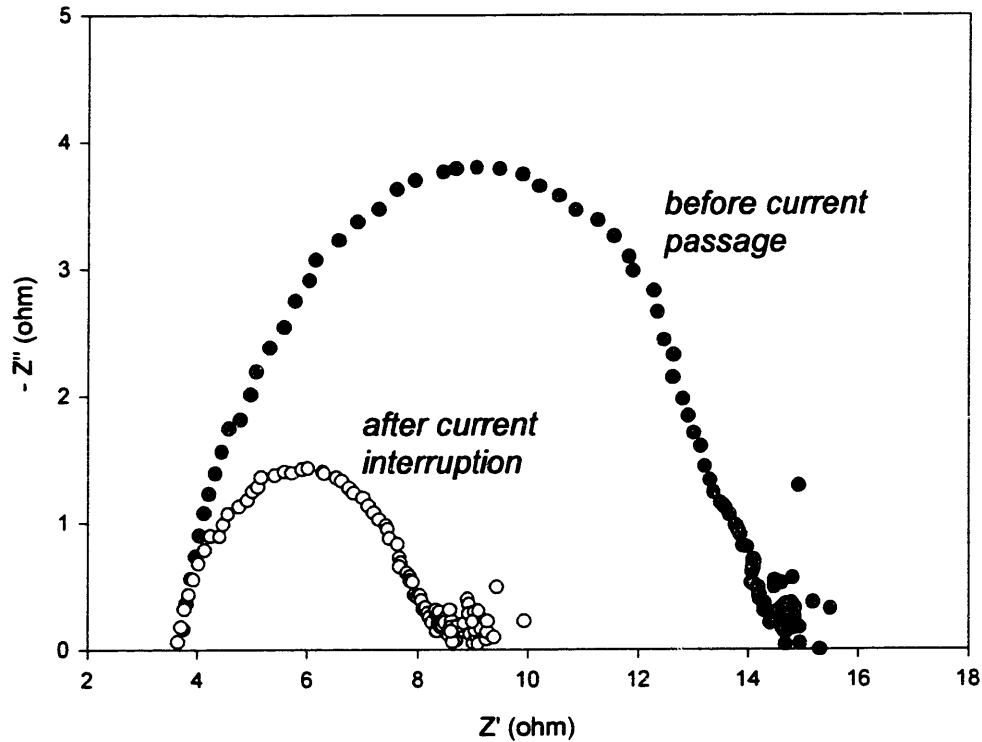


Figure 4.3. Cell impedance before and after current interruption.
80 wt% Ni spherical grains. $T=900^\circ\text{C}$.

Due to the observed change in impedance, the obtained I vs. η characteristics (figure 4.2) could not be readily interpreted. As seen in figure 4.3 the high-frequency intercept (corresponds to the ohmic contributions from the electrolyte, leads etc.), did not change much, suggesting that the current has affected the electrode. The state of the electrode thus depends on the amount of current that has been passed. We now know that this is

due to the formation/depletion of oxygen containing species (OCS) at the charge-transfer sites. When OCS are present at the charge-transfer sites, they partially inhibit the oxygen-exchange reaction. The thermodynamic stability of the OCS is altered by changes in the local oxygen potential induced by the ionic current. The kinetics of the oxygen-exchange reaction at the electrode keep changing depending on the current. The polarization characteristics in figure 4.2 cannot be interpreted on the basis of a single-constant exchange current.

This necessitated a further study in order to find the source of the observed impedance change. A three-electrode-electrochemical cell was constructed in order to isolate the Pt/YSZ interface. The results of the in-depth study of the influence of temperature, oxygen partial pressure and current on the oxygen-transfer reaction are presented in chapter 5. It will be shown in chapter 5, that the current-induced impedance change is linked to oxygen being pumped to or depleted from electrode/electrolyte interface. Oxygen reacts with the metal at the reaction sites to form oxygen-containing species, the presence of which partially blocks the oxygen-transfer reaction. The effect of direct current on the exchange reaction has been overlooked by other investigators. Most work on the exchange-reaction kinetics has focused on near-equilibrium impedance measurements. The only current that were passed were the ac ripples caused by the impedance measurements. These currents ($<0.01\text{mV}$) are too small to cause any measurable changes on the impedance spectra.

Chapter 5

Platinum-YSZ Interface

The impedance changes due to current passage in Ni-YSZ/YSZ/Pt cells was attributed to the local P_{O_2} change causing the formation/depletion of oxygen containing species (OCS). OCS are formed as a result of the oxygen interaction with the metal electrode. The presence of OCS at the charge transfer sites, changes the rate of the oxygen exchange reaction and its associated impedance. In order to test this hypothesis, an in depth study of the Pt/YSZ interface was carried out and the obtained results are presented and discussed in this chapter. Near equilibrium studies were initially conducted in order to establish the basic oxygen-transfer mechanism and compare the results to those of earlier investigators. In order to study the effect of faradaic currents, the interfacial impedance was monitored before and after current interruption in the time domain.

5.1 Near-Equilibrium Conditions (650°C to 900°C)

The interfacial impedance near equilibrium conditions was studied in the temperature range, 650 to 900°C and P_{O_2} range 0.01 to 1 atm. Near-equilibrium

impedance of the Pt/YSZ interface has been studied by many investigators (chapter 2). The system was similar to those of Bauerle [Bauerle 1969] and Velle [Velle 1991] and therefore only the summary of our results are reported here.

A single depressed arc was observed in the frequency region assigned to the interfacial-oxygen-charge-transfer reaction. R_p (the difference in the real axis intercepts of the arc) decreased steadily with increasing P_{O_2} above 700°C (figure 5.1).

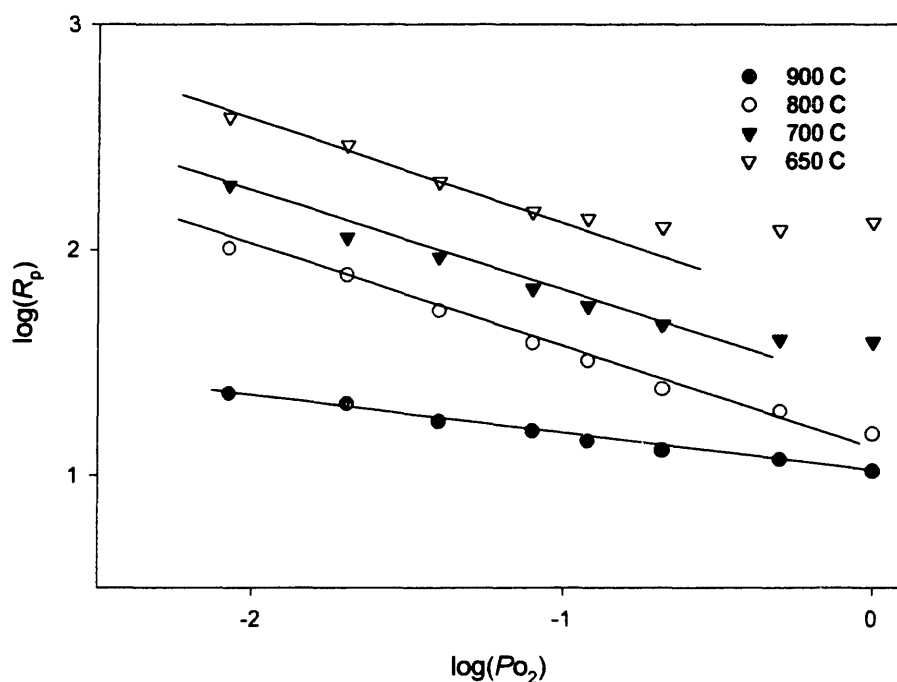


Figure 5.1. $\log R_p$ vs. $\log (P_{O_2})$.

At 700 and 650°C there was a minimum after which R_p increased with P_{O_2} . At 700°C the minimum occurred at $P_{O_2} = 0.21$ atm and at 650°C at $P_{O_2} = 0.12$ atm. The occurrence of

the minimum could be associated with a diffusion process that is prevalent at high surface coverage of oxygen. Velle *et al.* [Velle 1991] argue that a diffusion impedance caused by the formation of PtO is present at high P_{O_2} and/or low temperatures. In this case the number of measurements that were made beyond the minima are too few to draw any conclusions.

The results are summarized in table 5.1. As reported earlier [Velle 1991, Bauerle 1969] the rate of the oxygen transfer is related to the surface coverage of oxygen (equation 2.16 and 2.18 in chapter 2). m is negative which means that R_p decreases with increasing P_{O_2} . The results agree with the Langmuir dissociative adsorption model with low surface coverage (equation 2.15). The supply of oxygen in the cathodic reaction controls the rate. At 900°C, the P_{O_2} dependency is about half of what is observed at lower temperatures.

Table 5.1. Summary of near-equilibrium-impedance measurements of the Pt/YSZ interface.

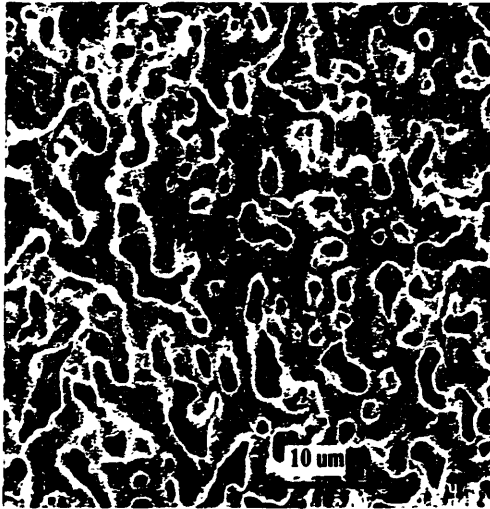
element	Q (kJ / mole)	$m, [R_p=(P_{O_2})^m]$
R_p	90 ± 5	$-0.18 \pm (?)$ ($T=900^\circ\text{C}$) -0.41 ± 0.01 ($T < 900^\circ\text{C}$)

The heat of dissociative adsorption for oxygen on platinum is 294 kJ/mole [Anderson 1975]. The activation energy calculated with equation (2.18) then becomes 208 ± 5 kJ/mole. This value is close to the value 199 kJ/mole found by Velle *et al.* [Velle 1991].

5.2 Microstructure

The microstructure of the electrode is shown in figure 5.2. Looking at the cross-section of a fractured interface of Pt/YSZ in a SEM one could see many contact points between Pt and YSZ such as the one shown in figure 5.2b. Necks seems to have been formed between Pt and YSZ. As seen from figure 5.2b, the necks are directly accessible by gas (due to the open porosity). Most likely the TPB where oxygen transfer across Pt/YSZ occurs is located at these necks.

(a) Top view
X 1500



(b) Cross section (Pt/YSZ interface)
X 15000



Figure 5.2. The Pt electrode and the Pt/YSZ interface.

5.3. Effect of Direct Current

In chapter 4 it was shown how the electrode impedance of a fuel cell was observed to change substantially after the passage of a direct current. Currents as low as 5 mA, passed for 5 minutes in some preliminary experiments, resulted in measurable changes. The changes with respect to the initial steady state were recorded after the current was applied. After going through a transient period, the impedance spectrum evolved towards a new steady state. The new steady state was not identical to the initial one before the current was passed. The nature and magnitude of both the time - dependent and time - independent changes were found to be influenced by the oxygen partial pressure (P_{O_2}), direction of the current, temperature, current density, and the total charge passed.

The focus of the present work is the analysis of the evolution of the interface after the current is interrupted. We will analyze here the evolution of the frequency response after the application for a short time of anodic and cathodic currents of constant and low magnitude, under isothermal conditions (at 900°C), and as a function of P_{O_2} . The study of the evolution of the state of the interface after current interruption requires the introduction of time as a variable in the analysis of the EIS spectra. The analysis reported here is based on a weighted - average state, because the EIS measurements require a finite time, and during this time the state of the system evolves towards a new steady state. We may call this approach wide - band, time - domain impedance spectroscopy.

In Figure 5.3a is shown the substantial change in the impedance spectra after the interruption of an anodic current of 10 mA passed for 10 minutes, when compared to the steady state measured before the current was passed.

After the passage of an anodic current (10 mA for 10 minutes) at $P_{O_2} = 0.61$ atm, the impedance spectrum is characterized by significantly larger values of the polarization resistance, R_p , and maximum absolute value of the imaginary component, Z''_{max} , as compared to the corresponding values for the steady - state spectra taken before the current was passed (figure 5.3a). The spectra changes with time and approaches a value that is characterized by larger values of R_p and Z''_{max} as compared to the steady state before current was passed. Next, starting from this new steady state, a cathodic current of 10 mA is passed for 10 minutes (Figure 5.3b). The new equilibrium spectrum measured after current interruption is 'shrunk.' The new steady state is different from both the earlier measured steady states. Since the cathodic current does not totally restore the interface to the initial state but leaves a hysteresis, it can be argued that the effect is not fully reversible. A similar irreversibility was observed when an anodic current was used to counter the change created by a cathodic current. Directly after interruption of cathodic or anodic currents there seemed to be a distinct time dependence of the spectra until the new equilibrium state was reached. The time evolution was, however, too fast to be determined using the initial impedance measurement setup. The patterns of time evolution and the hysteresis of the frequency response of the Pt/YSZ interfaces were also found to hold in other oxygen - rich atmospheres, such as, e.g., $P_{O_2} = 0.08$ atm and 0.21 atm.

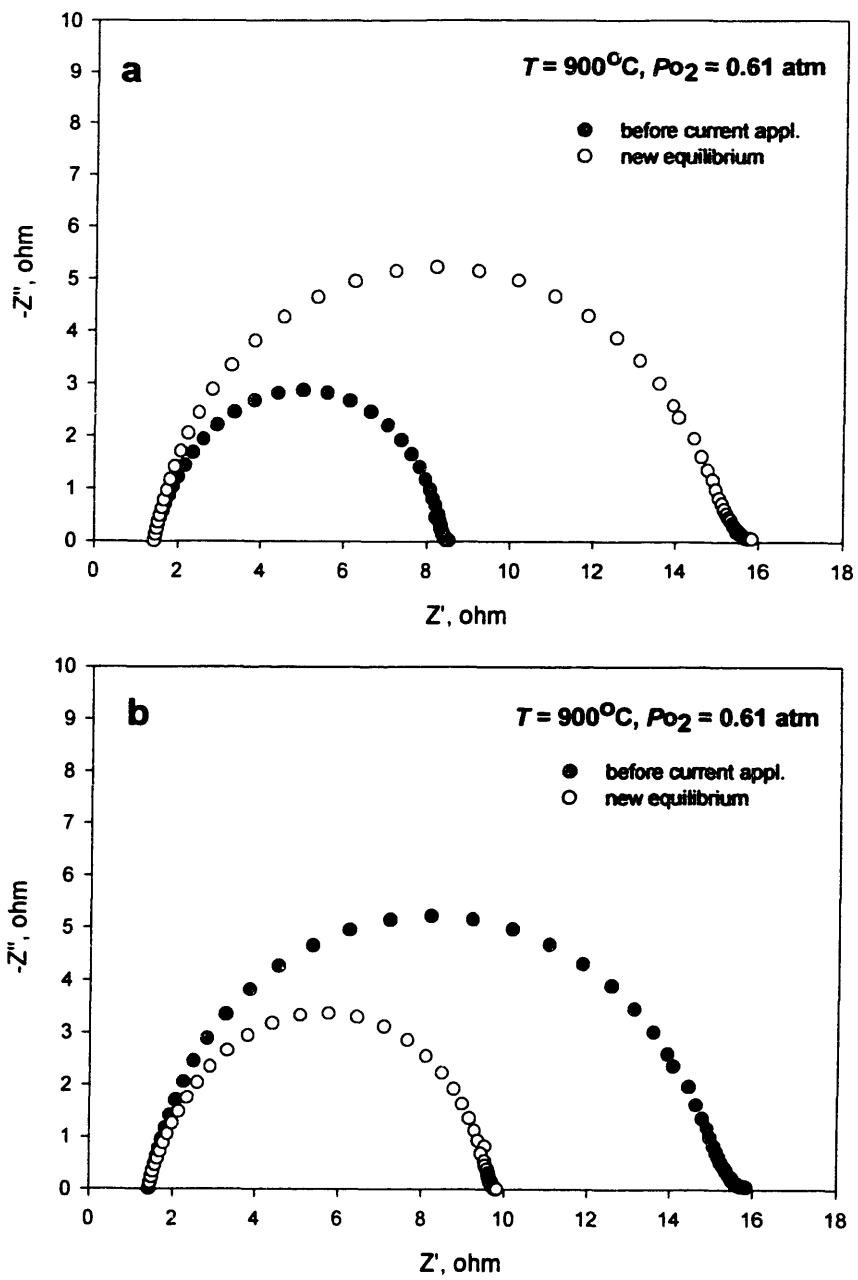


Figure 5.3 Effect of: (a) an anodic current (10 mA) passed for 10 minutes; (b) a cathodic current (10 mA) passed for 10 minutes.

A different pattern of behavior was found in an oxygen - poor atmosphere (pure argon), as shown in Figures 5.4a and 5.4b. The equilibrium spectrum after the interruption of an anodic current does not differ much from the initial spectrum. After a cathodic current, the spectrum is 'shrunk' (figure 5.4b). A significant difference is also found in the different time scales required for reaching a steady state: 15 - 20 minutes in an oxygen - rich atmosphere, more than 100 minutes in an oxygen - poor atmosphere.

The sequence of experiments was repeated after the initial results were obtained. Under atmospheres of different P_{O_2} values, the spectra repeated the individual features of their analogs in the previous runs.

As mentioned earlier, the EIS records a weighted - average state. The high - frequency part (above 1 kHz), recorded in under 1 second, may capture the state of the interface close to the time of current interruption, but the low frequency part covers a wider time interval, since it requires a much longer time to be recorded than the high - frequency part. We expect that a faster EIS data collection, presumably more adequate for the study of this type of effects, might be achieved by the use of a technique such as the time - resolved EIS, described by Popkirov [Popkirov 1996]. However, the experimental difficulties associated with the use of two well - synchronized cells, as required by the latter approach, are considerable for a high - temperature system. With this reservation, we will assume that the transient states recorded in the spectra taken after the current interruption describe the decay/reformation of species generated/depleted during current passage, and that these species are closely associated with the mechanism of charge and mass - transfer reactions across the interface.

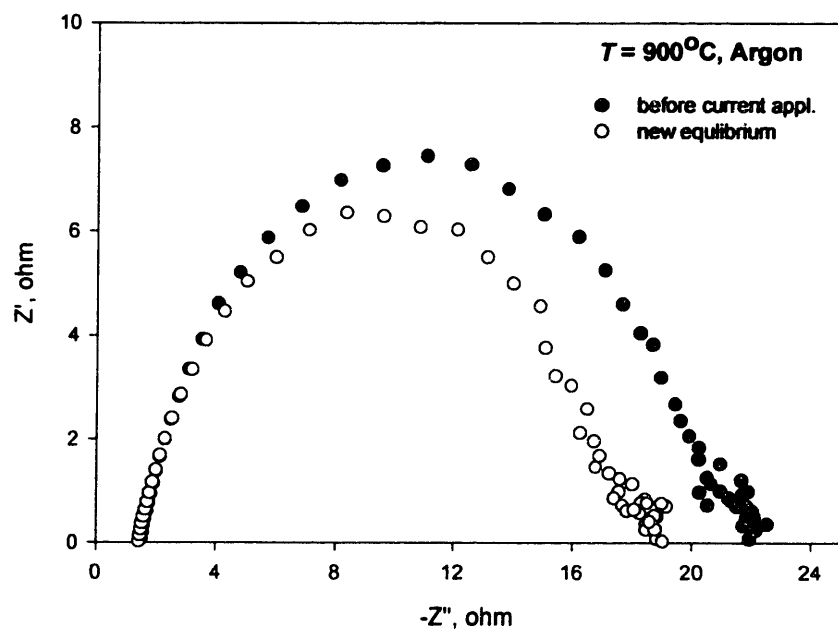
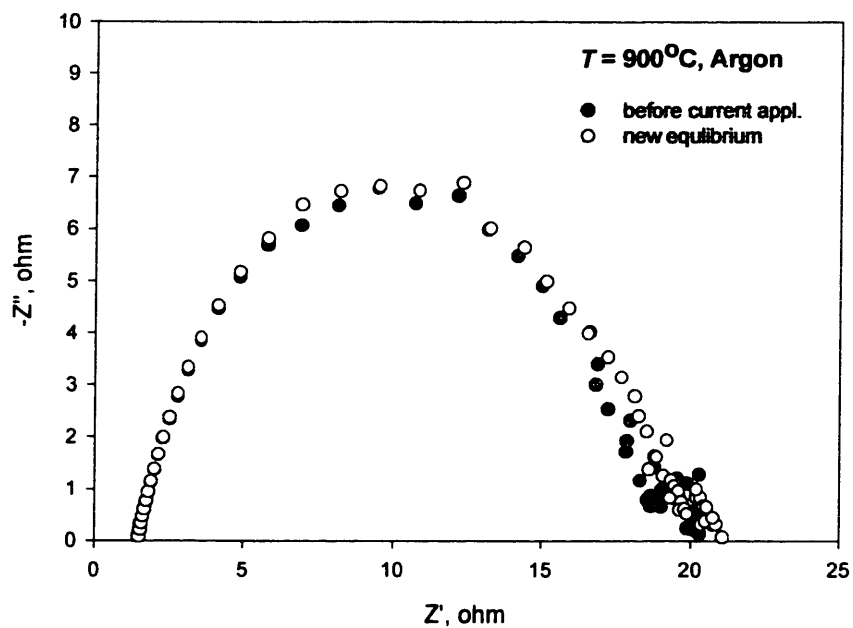


Figure 5.4. Effect of: (a) an anodic current (10 mA) passed for 10 minutes; (b) a cathodic current (10 mA) passed for 10 minutes.

The effect of long exposure (24 hours and more) of Pt electrodes to larger anodic currents (40 mA) has been studied by Van herle *et al.* [Van herle 1993] and was shown to lead to the doubling of the polarization resistance (R_p). This effect was attributed to the sintering of the porous platinum. The situation analyzed in this work is different. In order to avoid sintering of the electrode, much lower current densities and significantly shorter exposure times were used in our work. The microstructure of the Pt electrode after the experiment is the same as compared to the one observed before. Time - independent phenomena (hysteresis), as shown in Table 5.2, indicate that this effect is dependent on the direction of the current.

Table 5.2. Characteristics of the steady-state spectra established after current interruption.

atm. (P_{O_2})	current direction	before current R_p (ohm)	before current $f_{Z'_{max}}$ (Hz)	before current $f_{\theta_{max}}$ (Hz) (angle, °)	after current R_p (ohm)	after current $f_{Z'_{max}}$ (Hz)	after current $f_{\theta_{max}}$ (Hz) (angle, °)	change in R_p (ohm) (%)
$P_{O_2} \approx 10^{-5}$ atm	anodic	18.5	400	2009 (-47.5)	20.4	401	1596 (-48.6)	1.9 (10.3%)
„	cathodic	19.7	400	1596 (-48.6)	17.2	401	1596 (-47.2)	-2.5 (-13%)
$P_{O_2} = 8 \cdot 10^{-2}$ atm	anodic	7.6	1268	3185 (-37.6)	10.9	1007	3185 (-43)	3.3 (43%)
„	cathodic	10.9	1007	3185 (-43)	8.5	1007	3185 (-39.3)	-2.4 (-22%)
$P_{O_2} = 2.1 \cdot 10^{-1}$ atm	anodic	10	800	2530 (-42.9)	13.9	505	2530 (-45.8)	3.9 (39%)
„	cathodic	13.9	505	2530 (-45.9)	8.3	800	2535 (-39.4)	-5.6 (-40%)
$P_{O_2} = 6.1 \cdot 10^{-1}$ atm	anodic	7	1007	2530 (36.8)	14.2	505	2009 (-45.6)	7.2 (103%)
„	cathodic	14.2	505	2009 (-45.6)	8.5	800	2535 (-39.1)	-5.7 (-40%)

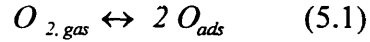
There is an increase in the polarization resistance (R_p) after oxygen has been pumped to the electrode (anodic current) whereas R_p decreases after oxygen has been removed (cathodic current). This effect is more pronounced in oxygen - rich atmospheres. Table 5.2 also gives the frequencies for the maximum imaginary component, $f_{z''\max}$, and maximum phase angle, $f_{\theta\max}$. Both these frequencies are indications of the lumped characteristics of the electrode processes involved. The apparent similarities in the values of $f_{z''\max}$ and $f_{\theta\max}$ suggest that the electrode processes in the initial and final steady states, respectively, are essentially of the same nature. Similarly, the chronoamperometry results of Robertson and Michaels [Robertson 1991] indicate that, after current interruption, the transient response seems to be dominated by the adsorption of oxygen. The currents considered by these authors are at least an order of magnitude higher than the currents passed by us.

5.3.1 The Time Dependent Behavior after Current Interruption

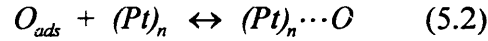
As mentioned in the previous section, the current-induced modification is not stable and a transient time dependent recovery of the impedance takes place after current interruption. The impedance evolves towards the steady state that existed before current passage. In order to capture the time dependent behavior, the impedance spectra had to be recorded fast enough with respect to the time scale of the recovery. The fastest spectra that could be recorded while maintaining a satisfactory accuracy in the measurements took a total of 55 seconds. An example of the recovery is shown in the inserts of figures 5.5a and 5.5b. Here the recovery is represented by R_p , the overall polarization taken as the difference in impedance between low and high frequency intercepts with the real axis in a Cole-Cole representation. The x-axis in the inserts represents the time passed after current interruption. The explanation to the current-induced modification of the interfacial impedance is described in section 5.3.2.

5.3.2 Physico-chemical Model

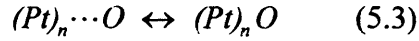
In oxygen - containing atmospheres it is likely that, under open-circuit condition, an equilibrium between the oxygen in the gas phase and the adsorbed oxygen atoms on the electrode surface will be established:



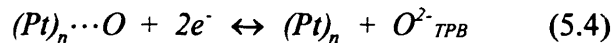
The coverage factor of the O_{ads} species, θ , is primarily a function of temperature, P_{O_2} , and the nature of the porous metal electrode [Velle 1991, Boukamp 1993, Kleitz 1981, Isaacs 1981, Mizusaki 1987, Van Hassel 1991]. We propose that the O_{ads} species can also be loosely and reversibly bound at certain sites, including the three phase boundaries (TPB):

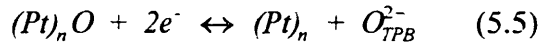


The transformation of these reversible sites into more stable, partially-oxidized species is possible as well:



According to reactions (5.1) - (5.3), the concentrations of $(Pt)_n \cdots O$ and $(Pt)_n O$ under open-circuit conditions, prior to any current passage, are governed by temperature and P_{O_2} in the gas phase. *In situ* confirmation for the formation under oxidizing conditions of a stable oxygen - rich layer at the Pt/zirconia interface was provided by Gopel *et al.* [Gopel 1990] and Zipprich *et al.* [Zipprich 1995] through high - temperature surface analytical techniques. Current passage will change the local oxygen concentration at the TPB, which may also change the concentration of the $(Pt)_n \cdots O$ and $(Pt)_n O$ species, according to the following reactions:





When $(Pt)_nO$ and $(Pt)_n$ are present at the TPB, they will decrease the number of effective charge - transfer sites, and thereby increase the interfacial impedance. From equations (5.4) and (5.5) it can be seen that an anodic current (oxygen is supplied to the TPB from the direction of the YSZ electrolyte) will lead to a decrease in the number of charge - transfer sites, thereby inhibiting the oxygen-transfer reaction. A cathodic current (oxygen is extracted from the TPB and incorporated into the YSZ electrolyte) will increase the concentration of charge - transfer sites and lead to electrocatalysis. The proposed model is described in figure 5.6 and agrees with the observed impedance spectra in oxygen - rich atmospheres.

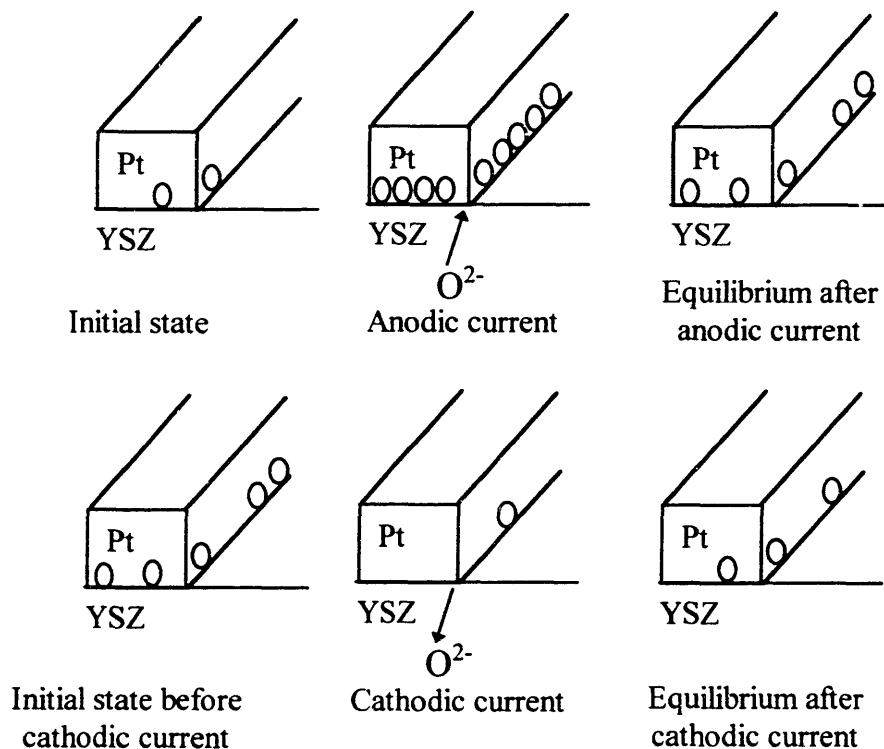


Figure 5.6. Current-induced oxygen supply / depletion at the TPB.

In pure argon ($P_{O_2} = 10^{-5}$ atm), the impedance spectra does not change much after the interruption of an anodic current (see figure 5.4a), which apparently contradicts our model. It should be remembered, however, that in oxygen - poor atmospheres the steady - state concentration of the $(Pt)_n^+O$ and $(Pt)_nO$ species is low and the steady - state polarization resistance is fairly large due to the low P_{O_2} . Since an anodic current leads to a local increase in P_{O_2} , the polarization resistance decreases in oxygen - poor atmospheres.

The difference between the new steady states and the initial ones (see Table 5.2) seems to be time - independent and can therefore be readily associated with the more stable species $(Pt)_nO$ rather than the labile $(Pt)_n^+O$.

The identification by Vayenas *et al.* [Vayenas 1995, Vayenas 1996] of different states of bound oxygen on polarized Pt - YSZ interfaces corroborates some of our findings, namely the current - induced formation of both unstable and remanent species on the interfaces under study. These authors identified the presence of two types of oxygen sites adsorbed on platinum, i.e., γ (normally adsorbed oxygen) and δ (spillover oxygen, pumped electrochemically).

Our experimental results indicate clearly that the frequency response of the electrode/electrolyte interface is strongly affected by the passage of even a small current. The fact that the effect is apparent after the current is interrupted (and a part of the change remains permanent) is explained by an increase or decrease in the density of electrocatalytic sites according to the above suggested model.

5.4 Chemical Cleaning

The presence of O (Pt)_n and O -(Pt)_n at the TPB increases the polarization resistance by partially blocking some of the sites available for oxygen transfer across the electrode/electrolyte interface. It is therefore conceivable that any treatment that might diminish the concentration of the OCS will lead to a decrease in the polarization resistance. This hypothesis was verified by monitoring the frequency response of the interface (previously equilibrated in air) exposed to atmospheres with low P_{O_2} , then switching back to air.

The sensitivity of the OCS to decomposition in a low P_{O_2} environment was investigated by exposure to an inert atmosphere (argon; $P_{O_2} = 10^{-5}$ atm). Treatments up to 24 hours did not result in any measurable change in impedance upon re-exposing the interface to air. A reducing atmosphere containing a mixture of CO-CO₂ ($P_{O_2} = 10^{-13}$ atm) was used for an active-cleaning treatment.

The changes determined by repeated CO-CO₂ treatments (1 hour each) followed by equilibration in air are shown in fig. 5.7. The early spectra (spectrum *I* in figure 5.7a) measured while the electrode was equilibrating with the air atmosphere are symmetric. The steady-state spectrum (spectrum *II* in figure 5.7a), after prolonged exposure to air measured prior to any CO-CO₂ treatment, has an asymmetric shape, indicative of the presence of one or more low-frequency processes. Presumably the Pt/YSZ interface contains an amount of OCS at this state. The first treatment resulted in a decrease of the steady-state R_p , mostly due to shrinkage of the low-frequency part of the spectrum (fig. spectrum *III* in 5.7a). The shape of the shrunk spectrum, which can be approximated by a

semicircle with a depression angle of 18° , is similar to the symmetric shapes of the spectra measured in the early stage of the equilibration in air prior to CO-CO₂ treatment (the shapes have depression angles varying between 15° - 20°).

The second treatment with CO-CO₂ results in a steady-state spectrum (spectrum *IV* in fig. 5.7b) characterized by half an order of magnitude increase in the value of R_p . The spectrum is quasi-symmetric: if the low-frequency (below 2 Hz) points are neglected, this spectrum can be described by a semicircle with a depression angle of 18.5° .

The following sequence of events is suggested to account for these observations. The initial treatment of the electrode in air leads to an increase of the R_p , which is attributed to an increase in the concentration of OCS. The first CO-CO₂ treatment creates the conditions for the decomposition of a fraction of the OCS. Consequently, the R_p is now lower.

After a second CO-CO₂ treatment, the increase in R_p upon re-exposure to air is dramatic compared to the first treatment. This increase of half an order of magnitude could be due to an over-exposure to the reducing atmosphere. It is hard to say why the interfacial impedance increases to such an extent, but it is possible that CO over-exposure may lead to a poisoning of the electrocatalytic interface. CO is known to poison the catalytic activity of Pt at lower temperatures [Kinoshita, 1988].

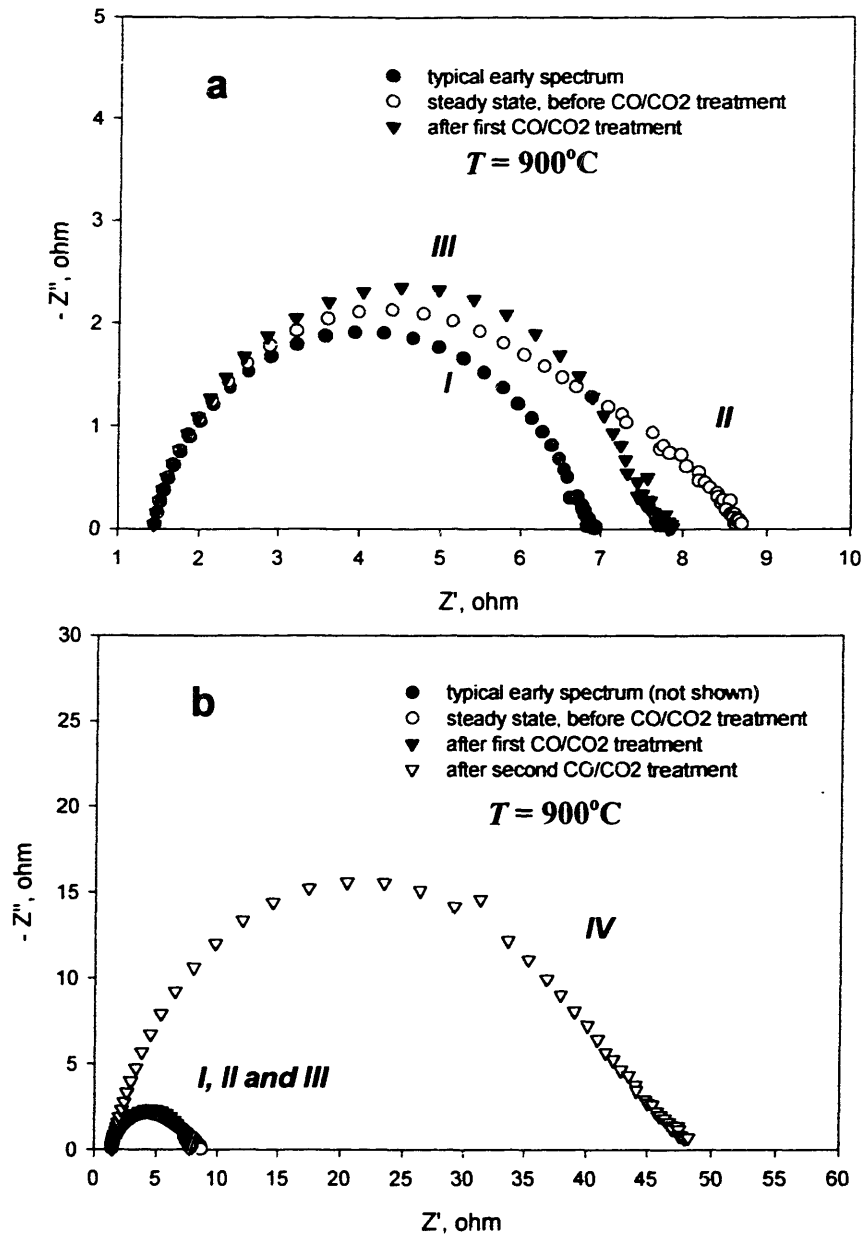


Figure 5.7. Impedance spectra in air before and after CO-CO₂ gas mixture treatment. The roman numerals indicate the sequence of the spectra taken.

5.5 Two Different Processes for Oxygen-and Charge-Transfer Reactions

Distinctly different behavior in the frequency response of the Pt/YSZ interface in air was encountered between 850°C - 1000°C while heating from room temperature to 1050°C in air as opposed to subsequent cooling. Figure 5.8a shows the interfacial impedance spectra in air for the temperature range $1050^{\circ}\text{C} \geq T \geq 900^{\circ}\text{C}$ upon heating from room temperature, and figure 5.8b shows the corresponding spectra after the same cell has been heat-treated at 1050°C and subsequently cooled. As seen in figure 5.8, the 1050°C treatment resulted in significantly lower interfacial impedances. Furthermore, the frequency of the maximum of the imaginary part of the impedance, $f_{Z''max}$, remains the same in figure 5.8b, thereby suggesting that the dominant reaction mechanism remains the same throughout the cooling process. Figure 5.8a, however shows that $f_{Z''max}$ has a temperature dependence, and a smaller value below 1050°C compared to figure 5.8b. This suggests that the oxygen and charge transfer reaction mechanism in figure 5.8a changes with temperature and is slower compared to that shown in figure 5.8b. This is further supported by the fact that the spectra in figure 5.8b took about 10-30 minutes to attain steady state after reaching the desired temperature. When heating from room temperature (figure 5.8a), the overall polarization, R_p , increased with time and it took considerably longer for the spectra to attain a steady state (5-20 hrs). The evolution with time of R_p , when heating from room temperature to 850°C and 950°C, is shown in figure 5.9.

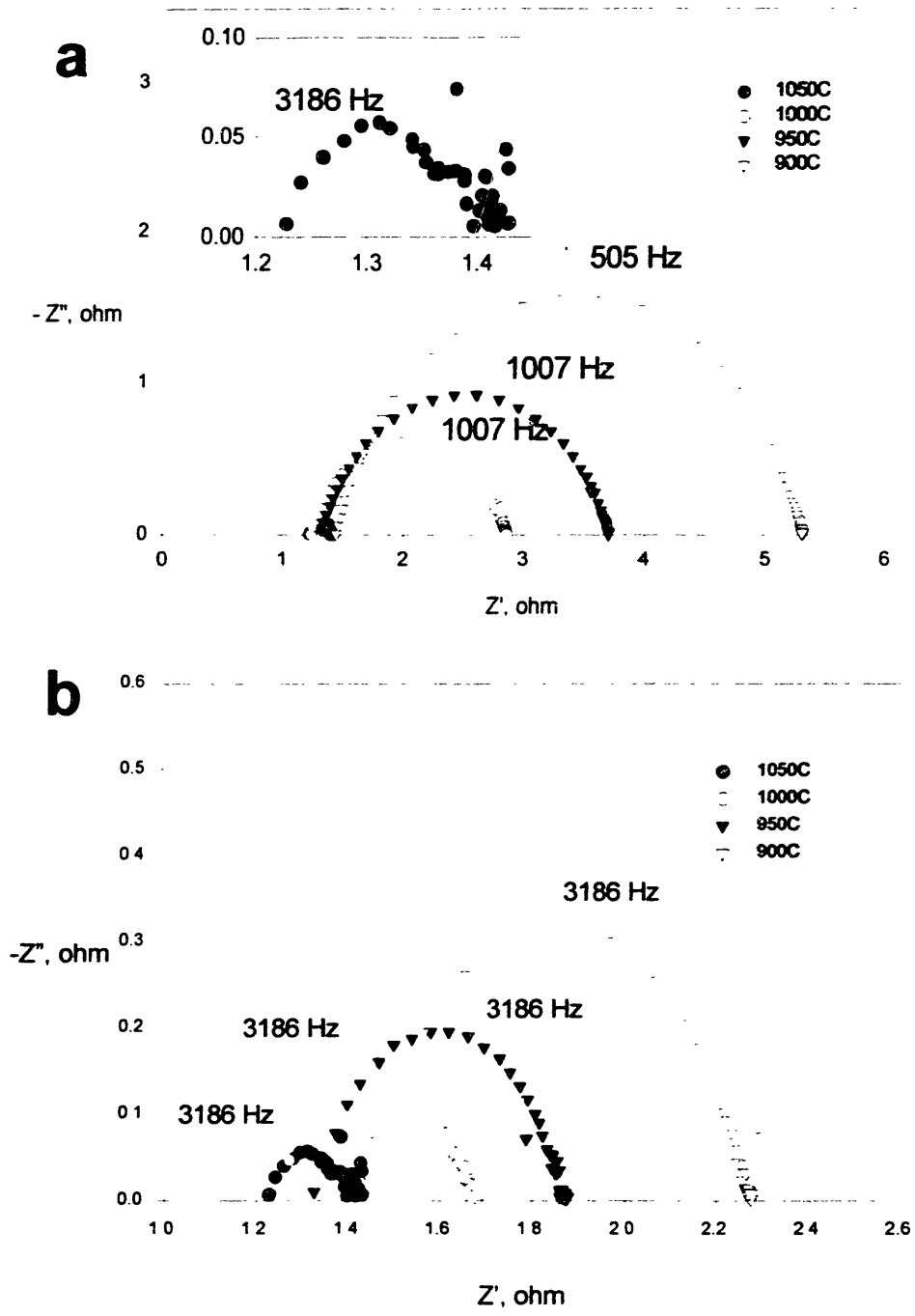


Figure 5.8. Steady-state spectra between 1050°C and 900°C: (a) heating from room temperature; (b) cooling from 1050°C.

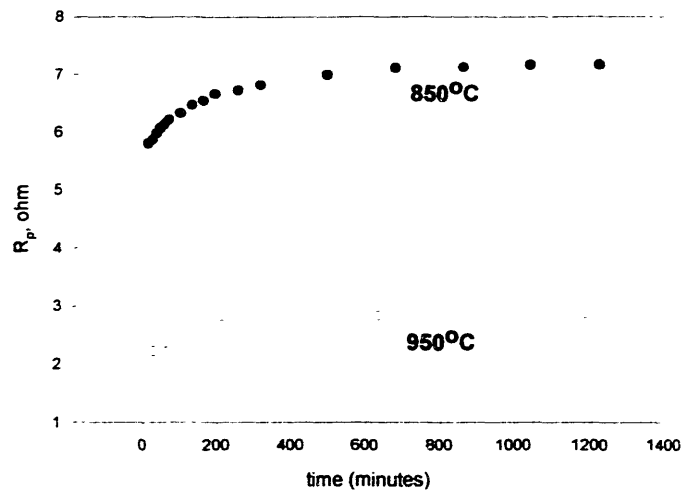


Figure 5.9. Equilibration after heating from room temperature.

The direct current-induced change in the impedance spectra that was discussed in section 5.2 was observed while heating from room temperature. The initial steady-state spectra were shown to be different from those taken after current interruption and this was linked to the formation and decomposition of OCS. This effect was not observed in the temperature range $1050^{\circ}\text{C} > T > 850^{\circ}\text{C}$ after the 1050°C treatment. Below 850°C , however, the direct current-induced modification of the impedance spectra was observable. The thermal-history conditions after which the current-induced modification of the impedance is observable are summarized in figure 5.10.

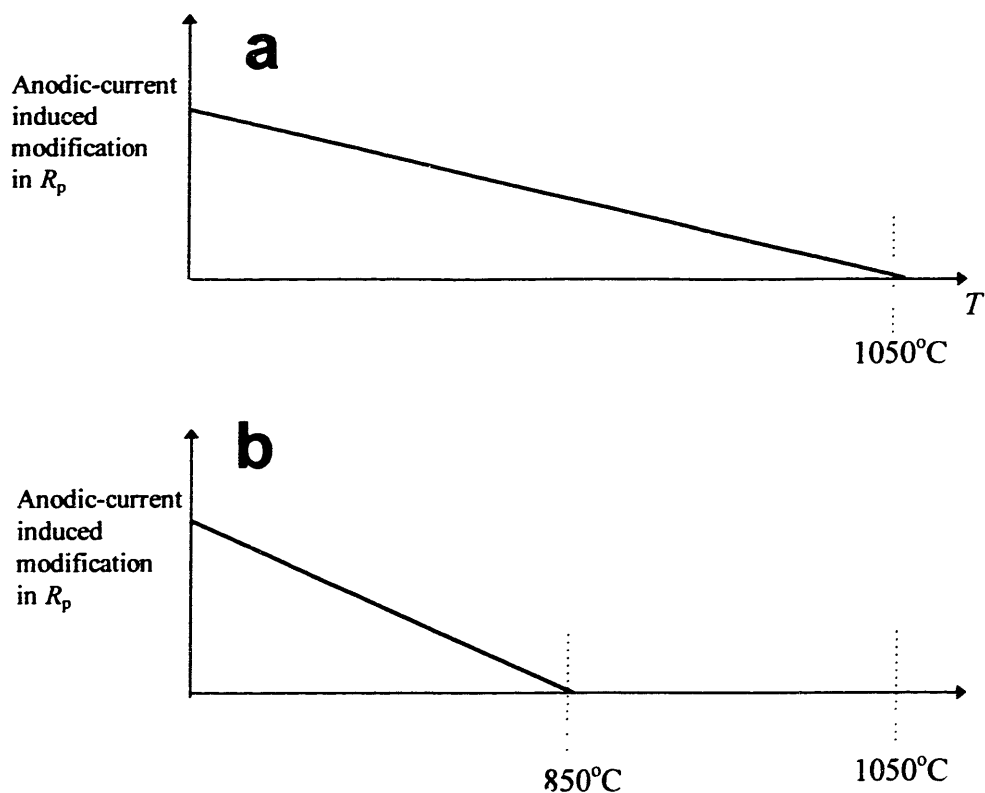
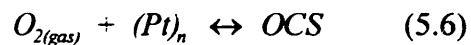


Figure 5.10 Thermal conditions for current-induced effect: (a) heating from room temperature; (b) cooling from 1050°C .

5.5.1. Slow Path through OCS

The Pt/YSZ interfacial impedance when heated to a temperature was found to increase with time during the equilibration process. As seen in figure 5.9, the impedance reaches a steady state after about 1000 minutes. The increase of the impedance is due to an equilibration of the electrode/electrolyte system with the gas phase. The oxygen in the gas phase equilibrates with the electrode, resulting in the formation of various oxygen-containing species, OCS. Using equations (5.1), (5.2) and (5.3) we may write:

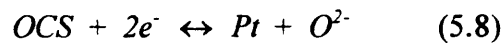


OCS includes all types of oxygen species present at the electrode, from weakly adsorbed oxygen atoms to stable oxides. The OCS are also present at the three-phase boundaries gas/Pt/YSZ (TPB). Since the TPBs are necessary sites for oxygen charge transfer [Siebert 1994, Steele 1995, Barbi 1995, Wiemhofer 1993, Wiemhofer 1995], the presence of OCS results in the blockage of the effective number of sites. The equilibration of the electrode in air involves an increase of the concentration of OCS at the TPB. When a fraction θ of the charge transfer sites is occupied by OCS, the total exchange current density can be written as:

$$i_0^{(total)} = i_0^{(ocs)}\theta + i_0^{(clean)}(1 - \theta) \quad (5.7)$$

Here $i_0^{(clean)}$ is the exchange current density for the charge transfer at the OCS-free TPB sites and $(1-\theta)$ is the fraction of the total TPB sites that are free of OCS. It is conceivable that a certain degree of oxygen transfer also occurs at the TPB that contain the OCS sites (although this process is expected to be much slower than that at the OCS-free TPB sites). In this case, $i_0^{(ocs)}$ would correspond to the exchange current at these sites. Since the OCS have a blocking effect, $i_0^{(clean)} \gg i_0^{(ocs)}$. The fraction θ is determined by the thermal history and the P_{O_2} exposure history of the Pt/YSZ interface (equation (5.6)).

The passage of a direct current alters the OCS concentration according to:



After the current passage, the concentration of the OCS-covered sites is altered according to equation (5.8) due to a local change in the oxygen potential. The exchange current is thus modified since the fraction of OCS at the TPB has been changed by $\Delta\theta$ and the

fraction of clean sites by $(-\Delta\theta)$. It may be noted that $\Delta\theta$ can be positive or negative depending on the direction of the current.

$$i_0 = i_0^{(OCS)}(\theta + \Delta\theta) + i_0^{(clean)}(1 - \theta - \Delta\theta) \quad (5.9)$$

If R_p is considered to be the charge-transfer resistance, it is inversely proportional to i_0 and is related to θ by:

$$\frac{1}{R_p} = C_1 - C_2(\Delta\theta) \quad (5.10)$$

Here C_1 is the exchange current before current passage and C_2 is equal to $(i_0^{(clean)} - i_0^{(OCS)})$. R_p will increase as $\Delta\theta$ increases due to an increase in the OCS concentration. By virtue of equation (5.8), anodic and cathodic currents should increase and decrease the OCS concentration at the TPB, respectively. Accordingly, an anodic current should increase the interfacial impedance by partially blocking some of the TPB sites, whereas a cathodic current should lead to a decrease in the impedance. As shown in figure 5.5, it is precisely what we observed when measuring the impedance just after the interruption of anodic and cathodic currents, respectively.

The current-induced modification has a time-dependent recovery of the impedance that takes place after current interruption. The impedance tries to evolve towards the steady state that existed before current passage. During the time-dependent recovery of the impedance, the OCS concentration re-equilibrates with the gas phase. This recovery is shown in the inserts in figure 5.5. Here the recovery is represented by R_p , the overall polarization taken as the difference in impedance between the low and high frequency intercepts with the real axis in a Cole-Cole plot. R_p is inversely proportional to the

effective number of the TPB sites. Figure 5.11 shows the difference in R_p , before and after different anodic currents are passed as a function of time after current interruption.

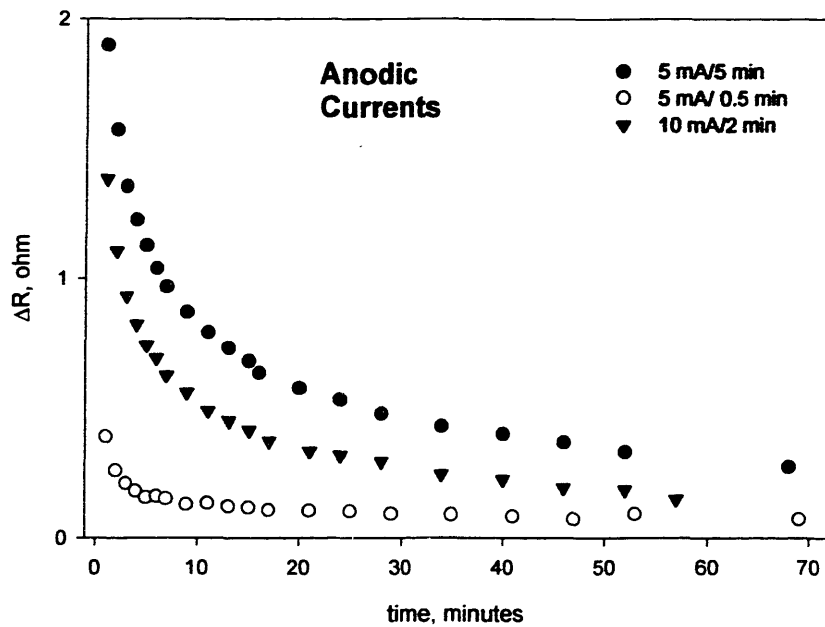


Figure 5.11. Time-dependent recovery after interruption of different current magnitudes.

Since θ is the fraction of OCS-covered sites at the TPB, the rate of change in the OCS concentration at the TPB after current interruption can be evaluated from the time dependency of $1/R_p$ according to equation (5.10). After anodic currents are passed, this rate would correspond to the removal of the excess OCS created during the passage of the anodic current. Physically this would involve decomposition of the OCS followed by

recombination and desorption of oxygen. The rates are shown in figure 5.12 for the same cases illustrated in figure 5.11.

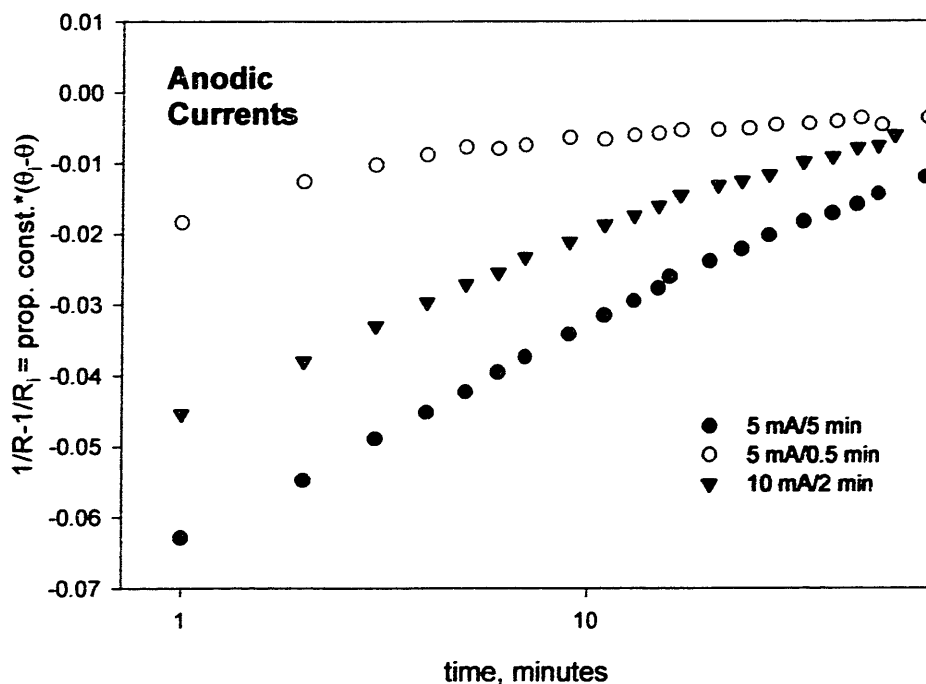


Figure 5.12. Rate of OCS equilibration with time.

The rate of change in the OCS can be written as:

$$\left(\frac{\partial \theta}{\partial t} \right)_{T, P, O_2} \propto \ln(t) \quad (5.11)$$

In figure 5.12 two distinct slopes can be identified during the equilibration process. This could mean that there are two distinct types of OCS that account for the two different observed rates. Oxygen loosely bonded to platinum, that can easily form and dissociate, $(Pt)_n \cdots O$, accounts for the initial fast recovery.

From figure 5.11 it can be seen that the effect on R_p is influenced by the magnitude of the charge that has been passed. Figure 5.13 shows R_p from the first spectra taken after interrupting anodic currents of various magnitudes (the lowest frequency point of the spectrum is taken 55 seconds after interruption).

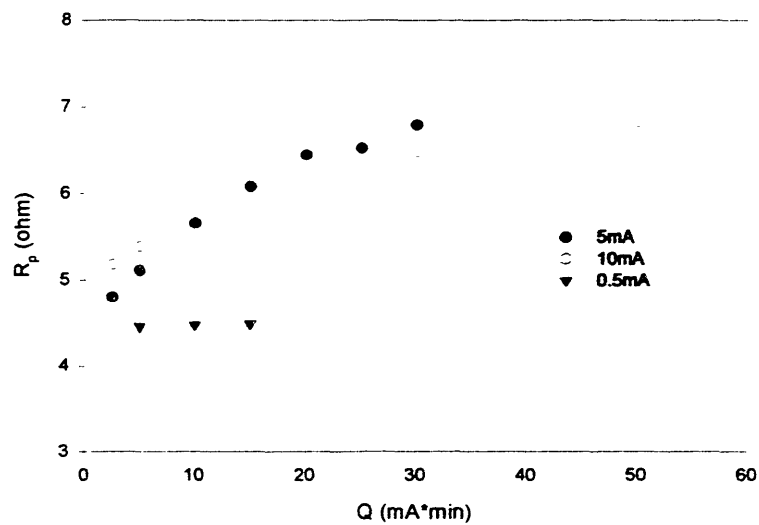


Figure 5.13 R_p , 55 seconds after current interruption.

For a given amount of charge passed, the change in R_p is not significant when the current is around 0.5 mA or below. At such low currents, the local oxygen potential is not sufficient to nucleate the OCS and observably affect R_p . When the anodic current is more than 5 mA, R_p initially increases with increasing charge due to more OCS formation according to equation (5.8). At about 40 mA*min (2.4 coulombs) there seems to be a limit beyond which there is no added effect. A thermodynamic or kinetic barrier is reached,

beyond which additional oxygen pumped to the interface does not result in further OCS formation.

5.5.2. Two Parallel Paths

The Pt/YSZ interface can be seen as having TPB sites that are either blocked by OCS or free of OCS, as seen in figure 5.14.

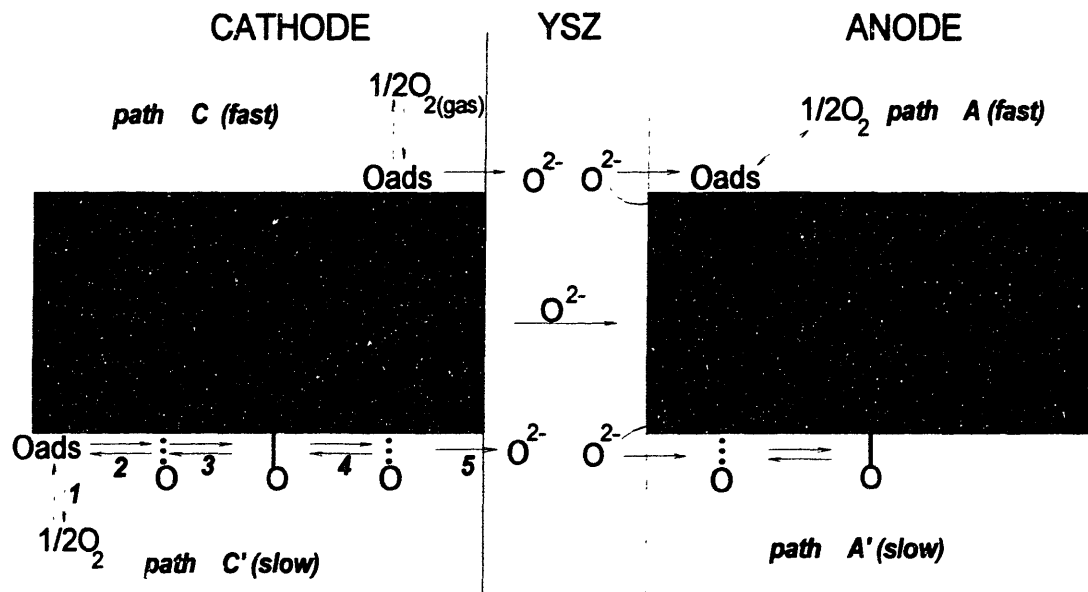


Figure 5.14. Physical-two-path model.

At the OCS-free sites, oxygen is transferred across the interface according to a fast anodic (A) or cathodic (C) path, whereas at the OCS-containing sites, oxygen is transferred along a much slower path, A' and C'. The slower path involves the formation/decay of the OCS as part of the oxygen transfer process. The activation energy for the overall polarization R_p in the temperature range $800^\circ C < T < 1050^\circ C$ is approximately 80 kJ greater when heating

from room temperature (figure 5.8a) compared to when cooling from 1050°C (figure 5.8b). This is of the same order of magnitude as the enthalpy of formation for PtO (71.18 kJ/mole)^[16] or PtO_{1.39} (56.94 kJ/mole) [Samsonov 1981] .

The heat treatment at 1050°C results in a gradual decrease in R_p as shown in figure 5.15a. As mentioned earlier, the slow charge-transfer path, including the current-induced modification of the impedance, is not observed upon cooling from 1050°C to 800°C (figure 5.5). Keeping the interface at 1050°C for a sufficiently long interval of time (\cong 1000 minutes) ultimately results in stripping most of the OCS. Somorjai *et al.* [Somorjai 1981] and Gland *et al.* [Gland 1980A, Gland 1980B] have reported that subsurface oxides in Pt decompose at around 980°C. By heating to 1050°C we may be providing the necessary activation energy for the complete decomposition of the OCS. It is conceivable that there has to be a sufficient concentration of OCS, serving as nucleation sites at the TPB, for the anodic current to further induce the formation of the OCS. This would explain our observation that after an OCS-stripping treatment at 1050°C, the OCS do not nucleate between 1050 and 800°C even after passing anodic currents, and therefore no current-induced modification of the impedance is observed in this regime. However, when heating from room temperature, the OCS are formed at lower temperatures and, since they are thermodynamically stable up to 1050°C, current-induced modification of the impedance spectra is present all the way up to 1050°C.

It is also conceivable, that once all the OCS have decomposed at 1050°C, the surface coverage becomes very small. Then, during cooling to 800°C, sufficient OCS do not nucleate to substantially change the surface coverage even when small anodic currents

are passed. As a result no visible current induced modification of the interfacial impedance is observed during this cooling process. However, when the temperature is below 800°C, it is possible that sufficient OCS are formed, and the oxygen-exchange reaction is primarily controlled by the smaller fraction of the clean sites. In this regime, small anodic currents can change the reaction of the clean sites by forming more OCS and thus also increase the interfacial impedance.

The evolution of the spectra taken during the heat treatment at 1050°C shows that $\log R_p$ decreases linearly with time until a lower limit is reached (figure 5.15a), after which, during cooling to 900°C, the frequency of the apex of the spectrum ($f_{Z_{\max}}$) is always 3186 Hz (see also figure 5.8b). We believe that the dominant oxygen and charge-transfer reaction mechanism is similar in all these cases. The equivalent circuit used in fitting these spectra (figure 5.15b) has a parallel R-C element and a distributed element (DE) of the ZARC [MacDonald 1987] type. The ZARC circuit is described as a resistor in parallel with a constant phase element (CPE). The resistor assigned to the high frequency intercept, and the inductive element (whose value is 1 μ H) in series with these components, are not represented in figure 5.15b. The DE is represented by the equation [MacDonald 1987]:

$$Z = \frac{R_{CPE}}{1 + A(j\omega)^\varphi} \quad (5.12)$$

where Z is the impedance of the DE, R_{CPE} the value of a resistor in parallel with the CPE, A a constant, ω related to the frequency, f , via the equation $\omega=2\pi f$, and φ is an exponent.

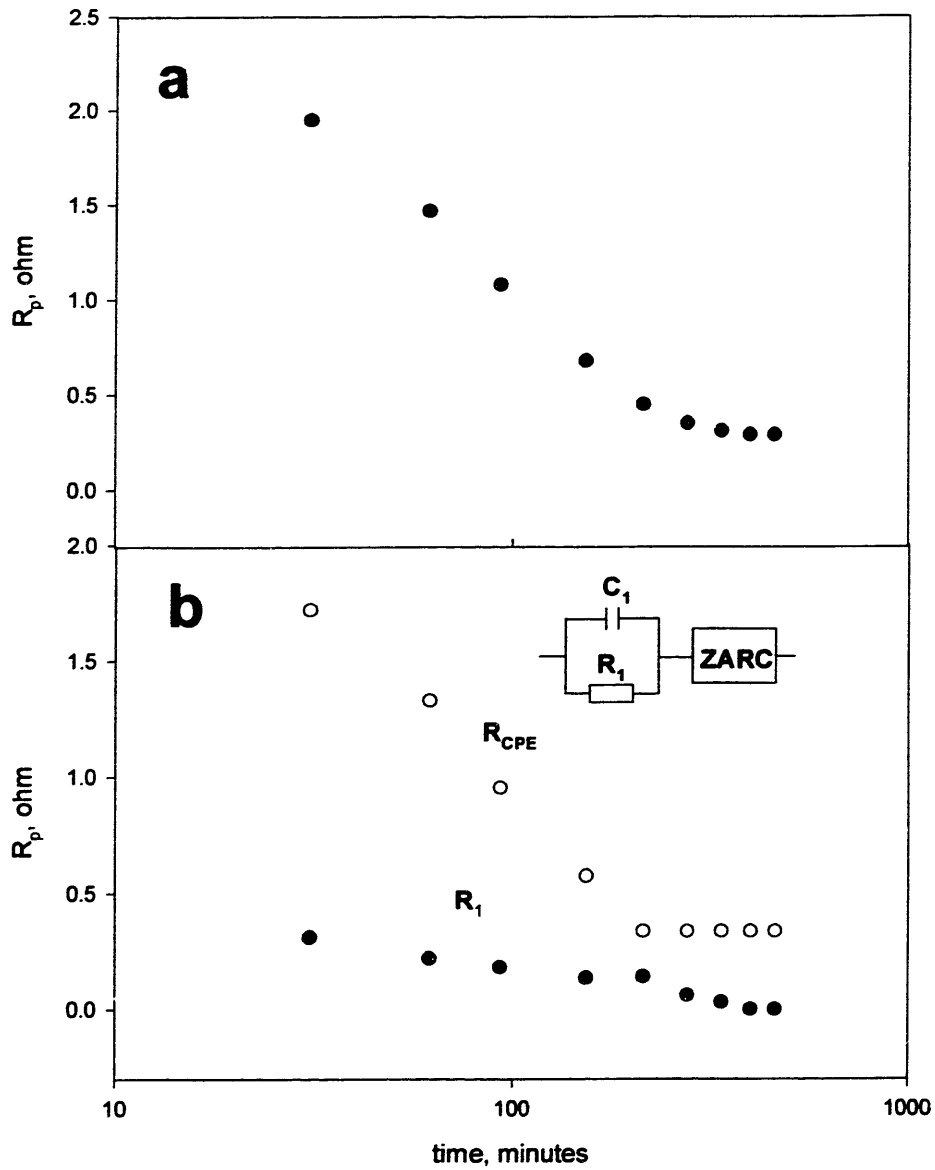


Figure 5.15. Evolution of the impedance spectra of the Pt/YSZ interface during heat treatment at 1050°C: (a) total R_p ; (b) the R values from a R - C element and from a distributed element. The last spectra are best fitted with a ZARC only; the R - C element tends to become insignificant.

The decay of R_p in figure 5.15 towards a lower asymptotic limit is assigned to the gradual decomposition of the OCS, including the subsurface oxygen. The two-element equivalent circuit used in the fitting of the early spectra (taken at < 100 minutes of dwell at 1050°C) cannot be used for fitting the steady-state spectra at this temperature. The steady state reached can be modeled by a ZARC. This process may be considered to represent the fast oxygen transfer for the interface under analysis. This process is represented by the spectra in figure 5.8b, and the fast paths A and C in figure 5.14. The values for A , R , and ϕ of the ZARC element fitted to the spectra in figure 5.8b, are given in Table 5.3.

Table 5.3. Values for the CPE fitted to the spectra in figure 5.14b.

T (°C)	ϕ	T (sec)	R (ohm)
900	0.79	0.0005	0.73
950	0.75	0.0007	0.65
1000	0.89	0.0003	0.43

The concentration of each type of charge-transfer site will determine the overall reaction rate and the respective exchange currents for each path. In an idealized model, the oxygen transfer depends on the type of the site. We propose that the process may be modeled by a parallel circuit in which the slow and the fast paths described in figure 5.14 are each assigned a weighting factor dependent on the state of the interface. The circuit represented in figure 5.16 represents this model.

The physical significance of the weighting factors may be described as follows: by assuming that the interface is OCS-free, the coverage factor θ is then 0 and the oxygen

transfer corresponds to the fast path. In the case of an interface completely covered by OCS, $\theta = 1$ and the oxygen transfer route then corresponds to the slow path. Any intermediate situation will be a combination of these two extremes. The contribution of each to the overall process would be proportional to the respective weighting factors. The weighting factors may therefore be understood as a quantitative measure of the effective coverage of the active sites.

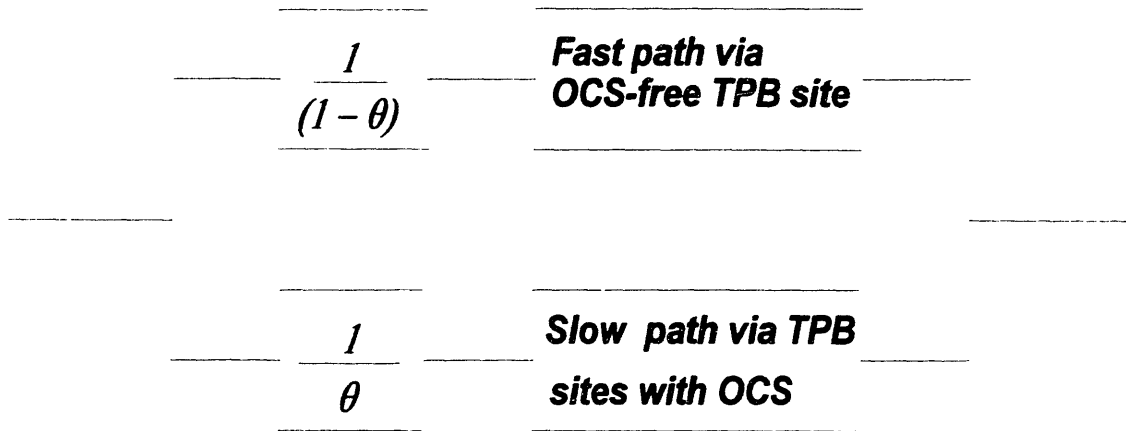


Figure 5.16. Electrical model of figure 5.14.

5.6. Summary of the Results on the Pt/YSZ Interface

Two parallel paths are identified for the oxygen-transfer process across the Pt/YSZ interface. One of this a slow path that involves the participation of oxygen containing species (OCS). The other is a fast path that occurs at OCS-stripped charge-transfer sites. The relative importance between the two paths is determined by the fraction of charge - transfer sites that are occupied by OCS. The concentration of OCS is dependent on the temperature, oxygen-partial pressure and current magnitude and direction.

The involvement of OCS in the oxygen transfer process is supported by the following observations:

- (1) The dependency of R_p on current direction and magnitude is consistent with the formation/depletion of OCS.
- (2) The decrease of R_p at 1050°C accompanied by an absence of a current induced change in the electrode impedance is consistent with the decomposition temperature of Pt-subsurface oxide.
- (3) The current induced modification for anodic currents is larger at lower temperatures. This is consistent with the increasing stability of oxygen compounds at lower temperature.

In order to further test the hypothesis of OCS participation in the oxygen transfer reaction, the Pd/YSZ system was investigated. This system was an ideal choice since Pd

and Pt have many properties in common especially with respect to their use as catalysts [Anderson 1975]. As an example, the heats of adsorption of O₂ on Pt and Pd are similar in magnitude. Furthermore both materials do not sinter appreciably below 900°C. The primary reason for choosing Pd is that its reactivity with oxygen is established. Pd forms a stable oxide, PdO under well known thermodynamic conditions. Using Pd as an electrode provides therefore an ample opportunity to test the model based on OCS. If PdO is an OCS that affects the oxygen transfer reaction then the current induced effect can be investigated and correlated with the thermodynamic stability of PdO. Chapter 6 discusses the results obtained for the Pd/YSZ interface.

Chapter 6

Palladium-YSZ Interface

The Pd/YSZ interface has not been as extensively studied as Pt. As explained in chapter 2, PdO is stable in air up to 850°C. Pd is therefore seldomly used as an electrode for electrochemical devices where a high exchange reaction kinetics is required at temperatures below 750°C. High temperature fuel cells and oxygen pumps are, in contrast, often operated under conditions where Pd is stable. The Pd/YSZ interface is therefore ideally suited to study the comparative influence of the chemical characteristics of the metal (Pt vs. Pd) on electrode kinetics, when all other parameters are kept the same (T , P_{O_2} , porosity and current). The relation of the polarization shift induced by direct current to the formation of OCS is especially interesting in the case of Pd. This is due to the availability of precise thermodynamic data about PdO (chapter 2). In the case of Pt, a strong connection was made between the impedance of the Pt/YSZ interface and OCS (chapter 5). This hypothesis will now be more directly tested in the case of Pd/YSZ. If the current induced modification of the interfacial impedance is due to the

formation/decomposition of PdO. then the thermodynamic stability of Pd vs. PdO should have an influence on the observed modification.

Initially, steady-state measurements were made in order to construct a reaction model for the oxygen and charge transfer by establishing the oxygen partial pressure and temperature dependence of the impedance. The influence of PdO formed under steady-state conditions was studied. Finally, the influence of direct current was studied as a function of temperature and oxygen partial pressure.

It was recommended by the vendor (Englehard) that the Pd ink should be heated above 600°C in air in order for the binder materials to burn off entirely. Thermogravimetric data on Pd powder supplied by Englehard show that the formation of PdO is unavoidable under these conditions. Thermogravimetric measurements performed on the base Pd powder from which the ink was made, showed that PdO decomposes to Pd when heated above 750°C. In order to standardize the measurements, the samples were heated to 900°C in air and then kept at this temperature in Argon (grade 5) for 24 hrs.

6.1 Steady State Measurements

Figure 6.1 shows the phase diagram for the Pd/PdO when the total pressure is 1 atm. A total of five series of discrete measurements at various P_{O_2} and T were made.

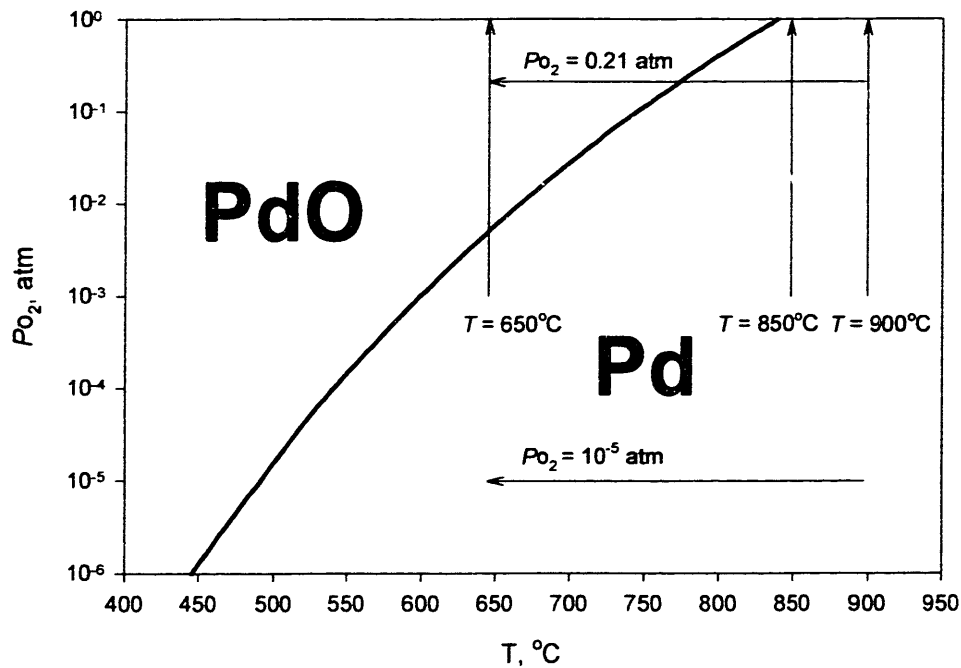


Figure 6.1. The Pd/PdO phase diagram and the 5 sets of steady-state measurements (each set represents discrete measurements in a range indicated by the lines and the general order in which the measurements were made is indicated by the arrows).

Three sets of isothermal measurements (900 , 850 , and 650°C) were made at discrete values of P_{O_2} ranging from 0.02 to 1 atm . All the measurements were carried out from low to high P_{O_2} . As seen in figure 6.1, at 900°C and 850°C Pd is stable in the entire range, whereas at 650°C PdO is stable only at high P_{O_2} . Two sets of isobaric measurements were

made ($P_{O_2} = 10^{-5}$ and 0.21 atm) at discrete values of T , ranging from 900 to 650 °C (measurements were made from high to low temperature).

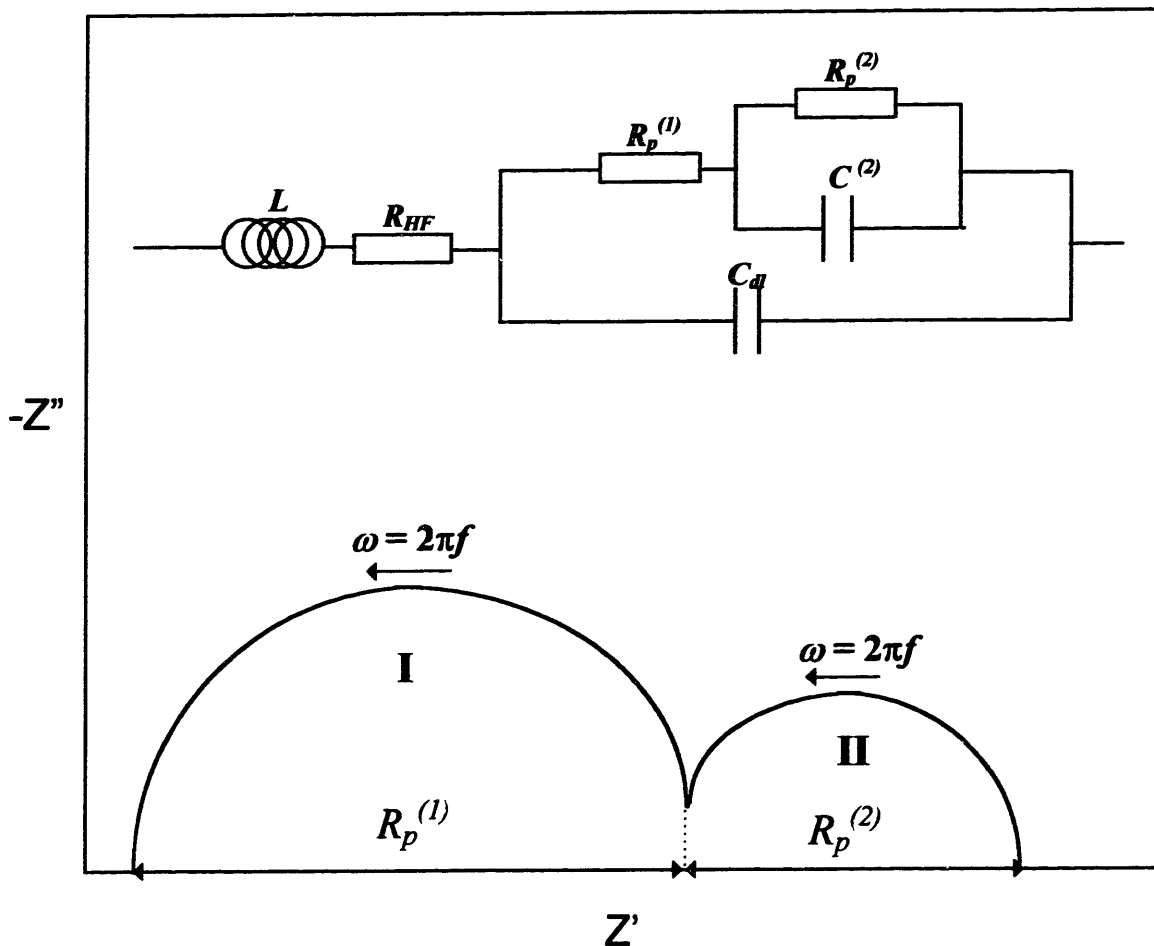


Figure 6.2. Representative impedance spectra of the Pd/YSZ interface.

Apart from a resistive element at high frequencies, the impedance spectra consist of two separated arcs (I and II in figure 6.2). The high frequency intercept is attributed to the ohmic drops and the two arcs are attributed to the electrode processes. At higher temperatures and low oxygen partial pressures, in the absence of PdO, the arcs are well

separated. There is a slight overlap and the intersection is at 62 Hz. The low frequency arcs can be interpreted with the circuit shown in figure 6.2. The magnitude of C_{dl} was in the order of 100 μ F whereas $C^{(2)}$ was between 0.04 and 0.7 F. $R_p^{(2)}$ was therefore dominated by $C^{(2)}$ at the higher frequencies where arc I was observed. The low-frequency real-axis intercept is $R_p^{(1)} + R_p^{(2)}$.

6.1.1 Effect of Oxygen Partial Pressure

In the region where Pd was stable and PdO was absent, the effect of increasing the oxygen partial pressure decreased the radii of both arcs I and II. Spectra taken under isothermal conditions of 900°C at various P_{O_2} are shown in figure 6.3.

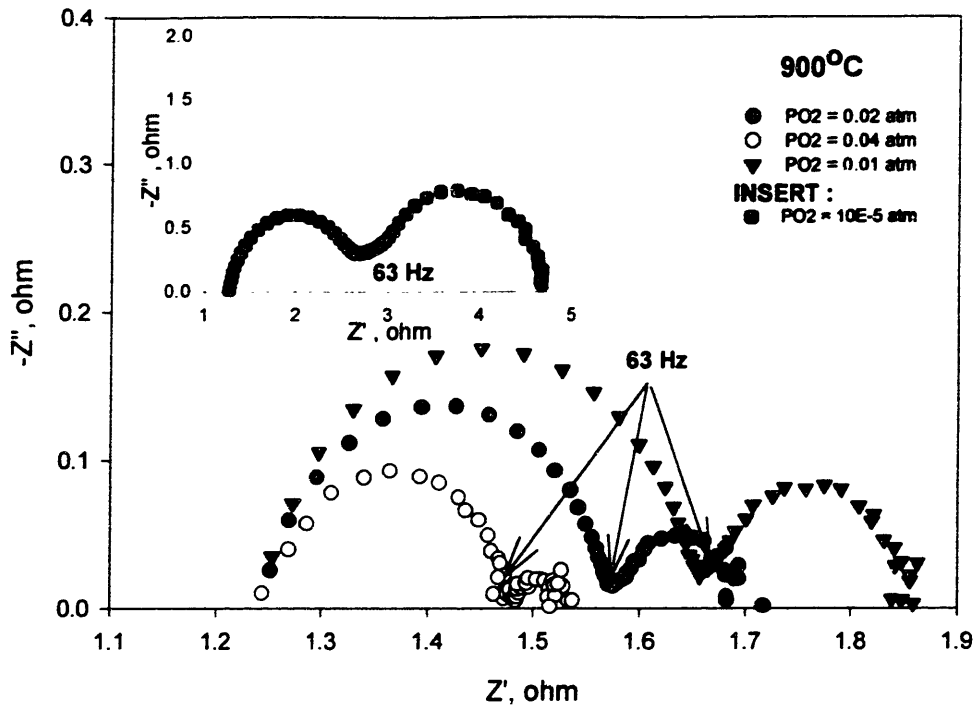


Figure 6.3 Impedance spectra of Pd/YSZ at 900°C under different P_{O_2} .

The initiation of arc II remains constant at 63 Hz, and arc II seems to be more strongly influenced by the partial pressure change than arc I. From the insert in figure 6.3, which shows the spectra at $P_{O_2} = 10^{-5}$ atm, it is seen that arc II is now larger than arc I. Figure 6.4 illustrates the dependence of $\log R_p^{(1)}$ and $\log R_p^{(2)}$ on $\log P_{O_2}$.

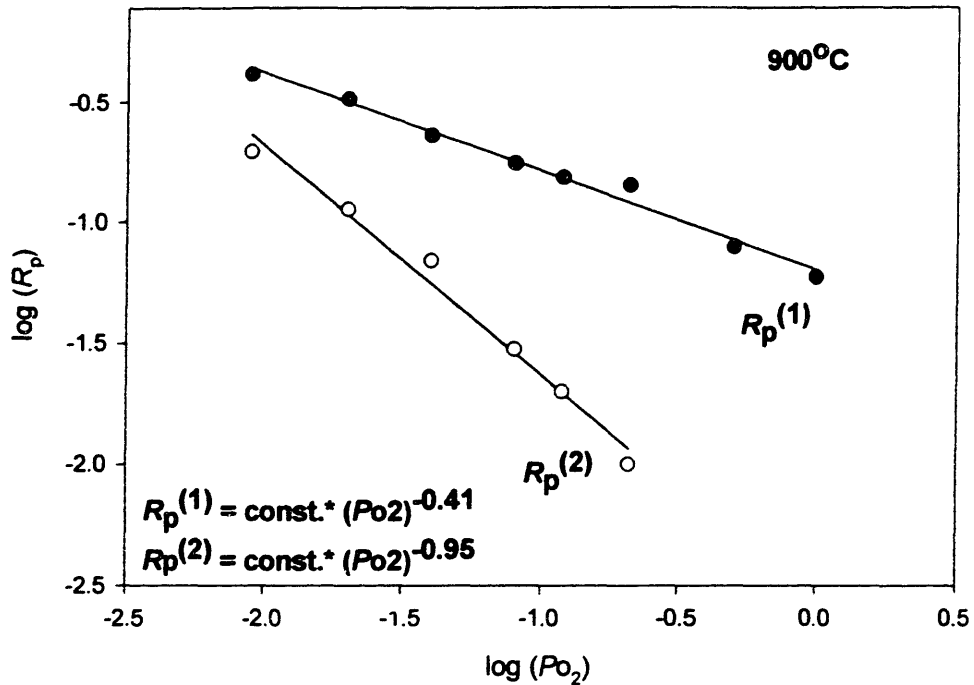


Figure 6.4 The dependence of the polarization on $\log (Po_2)$ at 900°C.

Figure 6.4 demonstrates that both $\log R_p^{(1)}$ and $\log R_p^{(2)}$ adhere to a linear dependence of $\log Po_2$. The slopes resulting from linear regression are given in figure 6.4. C_{dl} was 100 μF and no dependence on Po_2 was found whereas $C^{(2)}$ increased with Po_2 from 0.3 to 0.6 F.

At 850°C the behavior was similar to 900°C, apart from a slight increase in $R_p^{(1)}$ at oxygen partial pressures of 0.5 and 1 atm (figure 6.5). This result could be attributed to the formation of OCS. However, the type of OCS formed would, in this case, not be stoichiometric PdO since it is not stable at 850°C (figure 6.1).

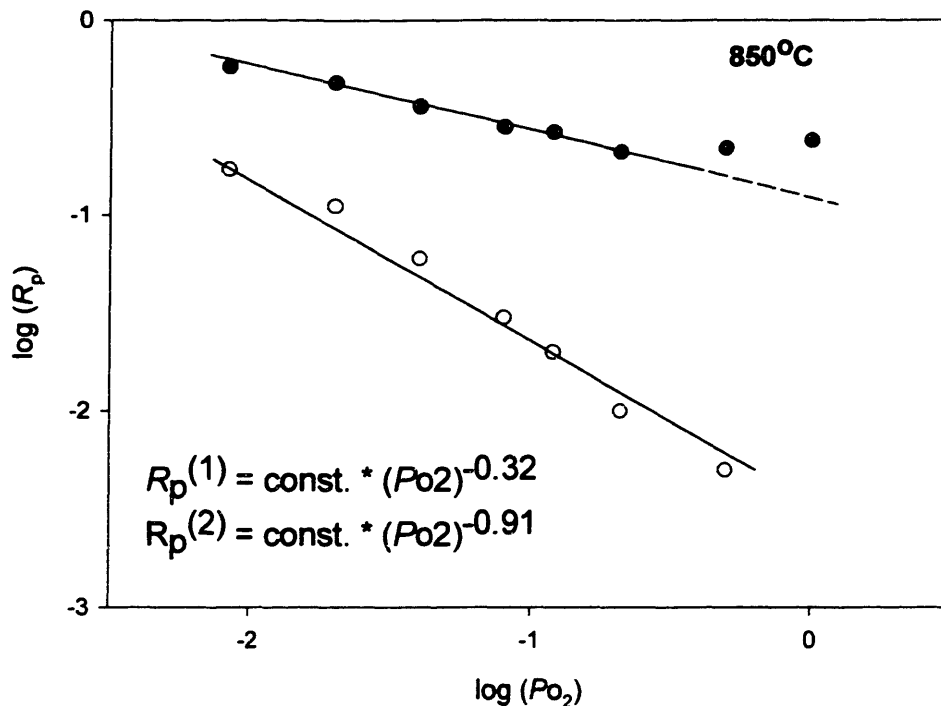


Figure 6.5. The dependence of the polarization on $\log (P_{O_2})$ at 850°C.

C_{dl} was found to be 100 μF and independent of P_{O_2} , which is identical to the results obtained at 900°C. $C^{(2)}$ increased with P_{O_2} from about 0.04 to 0.7 F.

The effect of P_{O_2} on R_p ($R_p = R_p^{(1)} + R_p^{(2)}$) at 650°C is shown in figure 6.6. $R_p^{(1)}$ was found to be strongly dependent on the temperature. It will be shown in the next section that the temperature dependence of $R_p^{(1)}$ is much larger than that of $R_p^{(2)}$. At 650°C, $R_p^{(2)}$ is insignificant in comparison to $R_p^{(1)}$ (thus, $R_p \approx R_p^{(1)}$). From figure 6.1 it can be seen that PdO is thermodynamically stable at P_{O_2} greater than $7 \cdot 10^{-3}$ atm (the entire

range in figure 6.6). Initially, the impedance shrinks with P_{O_2} . At about $P_{O_2} = 0.04$ atm ($\log P_{O_2} = 1.4$), there is a change in the dependence.

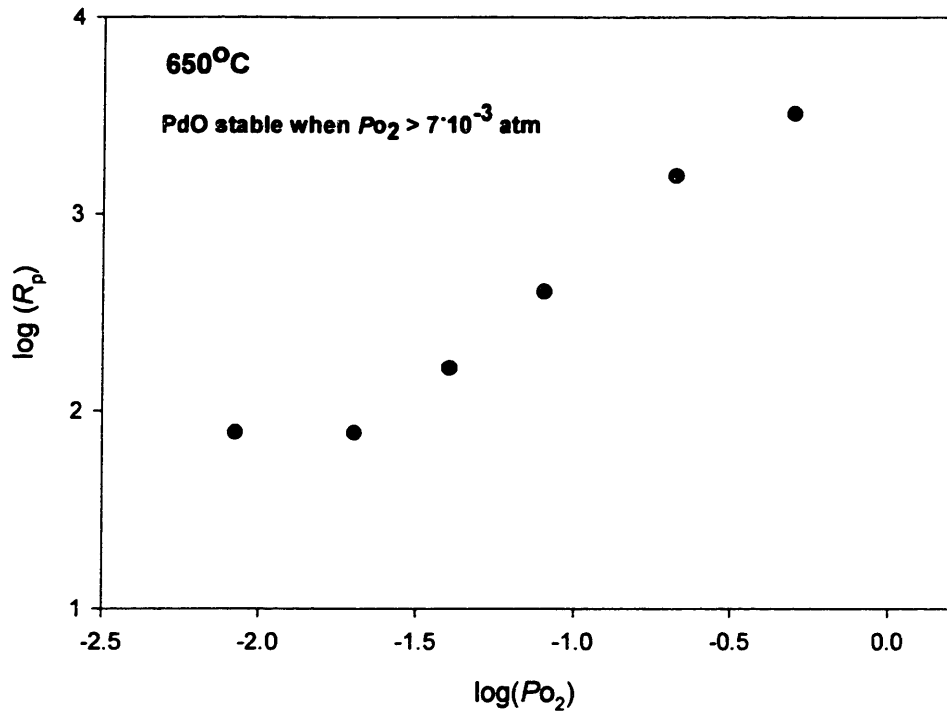


Figure 6.6. The dependence of the polarization on $\log(P_{O_2})$ at 650°C .

The impedance spectra does not stabilize but changes with time as can be seen in figure 6.7. As shown by the insert in figure 6.7, there is an initial decrease during the first 10 minutes. Then the impedance starts to increase. This increase is most probably due to the onset of oxidation. The rate of increase is initially rapid, but then the impedance approaches a quasi-stable state. The initial decrease is due to the decrease in $R_p^{(1)}$ with P_{O_2} . At higher temperatures where PdO is not stable, this decrease is seen in a larger P_{O_2} range (figures 6.4 and 6.5).

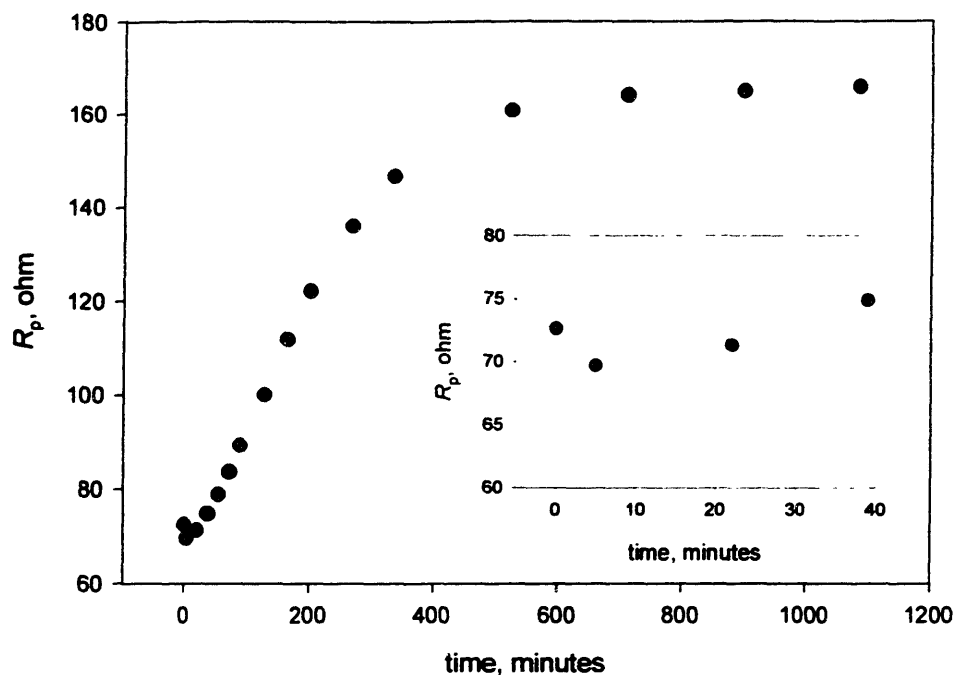


Figure 6.7. The time-dependent change in polarization observed above $P_{O_2} > 0.04$ atm at 650°C .

R_p in figure 6.7 is calculated from the real axis intercepts of the impedance spectra. Four of these spectra from different times during the oxidation are shown in figure 6.8. During the first 30 minutes, the basic shape of the arc remains the same in spite of the increase in radius. It can therefore be assumed that the process responsible for $R_p^{(1)}$ is still the main contribution to the impedance. After about 40 minutes, the arc becomes distinctly asymmetric at the low frequency region (6.8b-d). This indicates that the spectrum is no longer a single arc but rather consists of 2 or more overlapping arcs with close relaxation times.

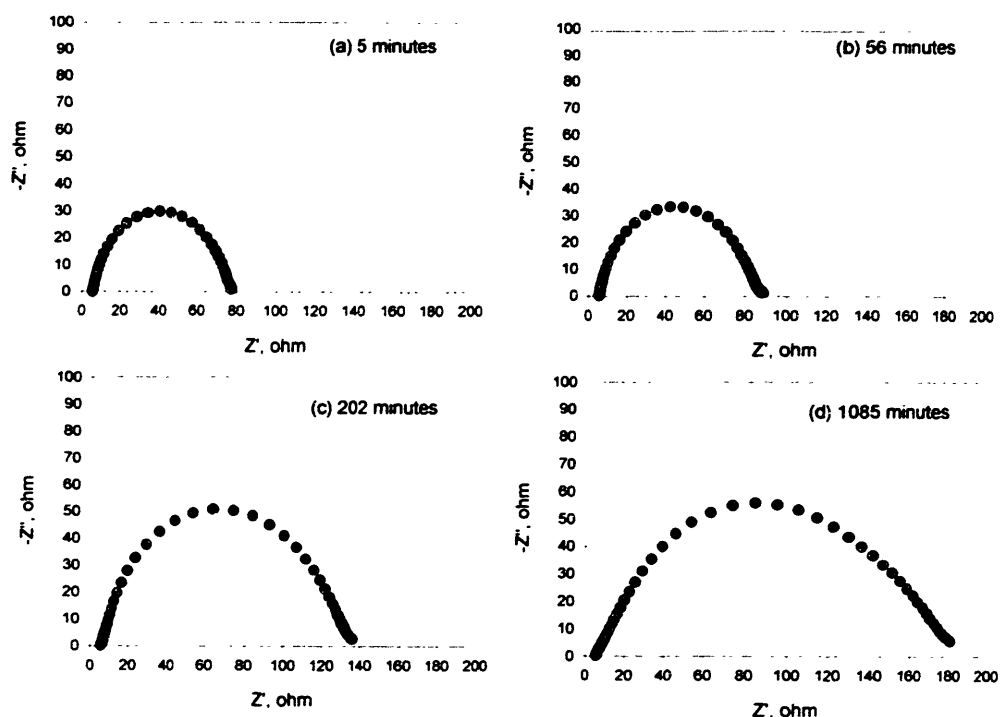


Figure 6.8 The time-dependent change in impedance above $P_{O_2} = 0.04$ atm at 650°C .

There seems to be a change in the mechanism as the oxidation proceeds. However, the two mechanisms are difficult to distinguish since the spectra are taken under dynamic conditions.

In order to compare the two mechanisms, two spectra are needed: one taken prior to any oxidation and the other recorded after the oxidation processes are either completed or have practically halted due to kinetic reasons. In order to create these two situations, the following experiment was carried out. The cell was exposed to pure O_2 until the spectra were stable with time. The system was then brought back to $P_{O_2} = 0.02$ atm

($\log P_{O_2} = -1.7$; $T = 650^\circ\text{C}$). PdO is stable under these conditions; thus no decomposition should have occurred. The impedance of the oxidized electrode was then compared to the state of the interface at $P_{O_2} = 0.02$ atm while coming from lower P_{O_2} where no oxidation was observed (figure 6.6) . Figure 6.9 shows the remarkable difference between the two states.

The two states must be represented with different electrical models (figure 6.10). Before oxidation, the arc is simply modeled as a Randle's circuit. This is possible since $R_p^{(2)}$ is negligible, as described above. After oxidation the impedance can not easily be deconvoluted unless the physical nature of the change induced by oxidation is characterized. This characterization will be described in 6.1.5.

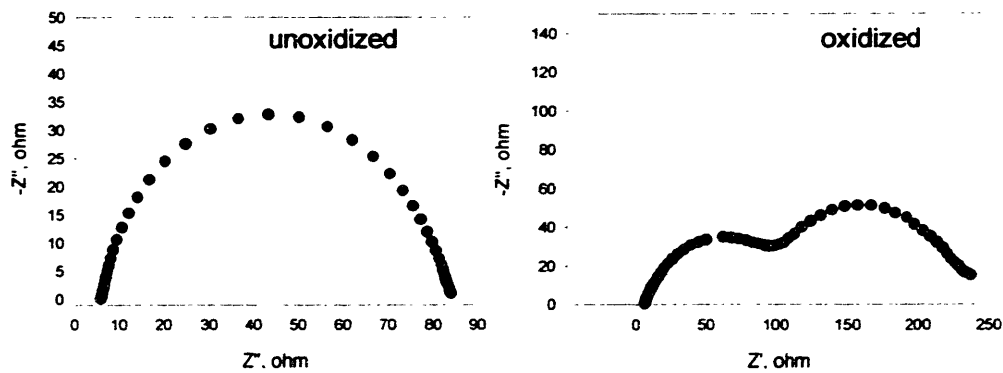


Figure 6.9 Impedance spectra of Pd/YSZ at $P_{O_2}=0.02$ atm and 650°C .

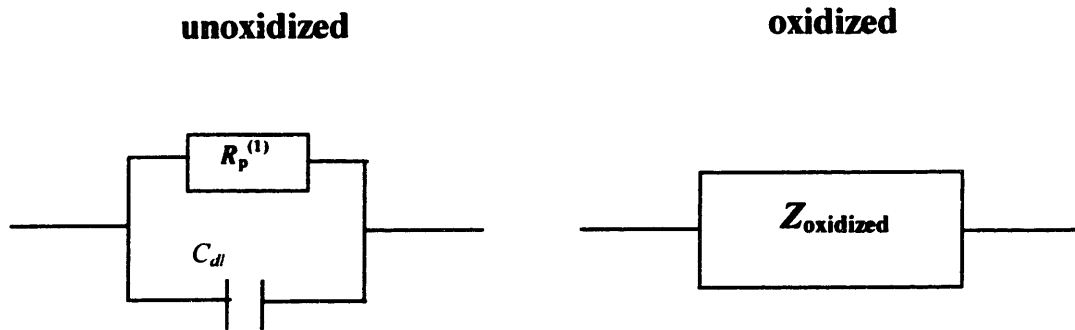


Figure 6.10. Electrical models for the two states in figure 6.9:
(a) unoxidized; (b) oxidized.

6.1.2 Effect of Temperature

A typical temperature dependence of the impedance of the Pd/YSZ interface is shown in figure 6.11. Both arcs increase with decrease in temperature, but arc I is more strongly dependent on the temperature than arc II. As seen in the previous section, $R_p^{(2)}$ is a strong decaying function of P_{O_2} . In order to obtain a wide range of polarization values for $R_p^{(2)}$, a temperature dependence of R_p , under Argon (P_{O_2} was measured to be 10^{-5} atm) was measured. Below 800°C the contribution of arc II becomes insignificant, at P_{O_2} higher than

10^{-5} atm. The results from the two sets of measurements where the temperature was varied under isobaric conditions are shown in figures 6.12 and 6.13.

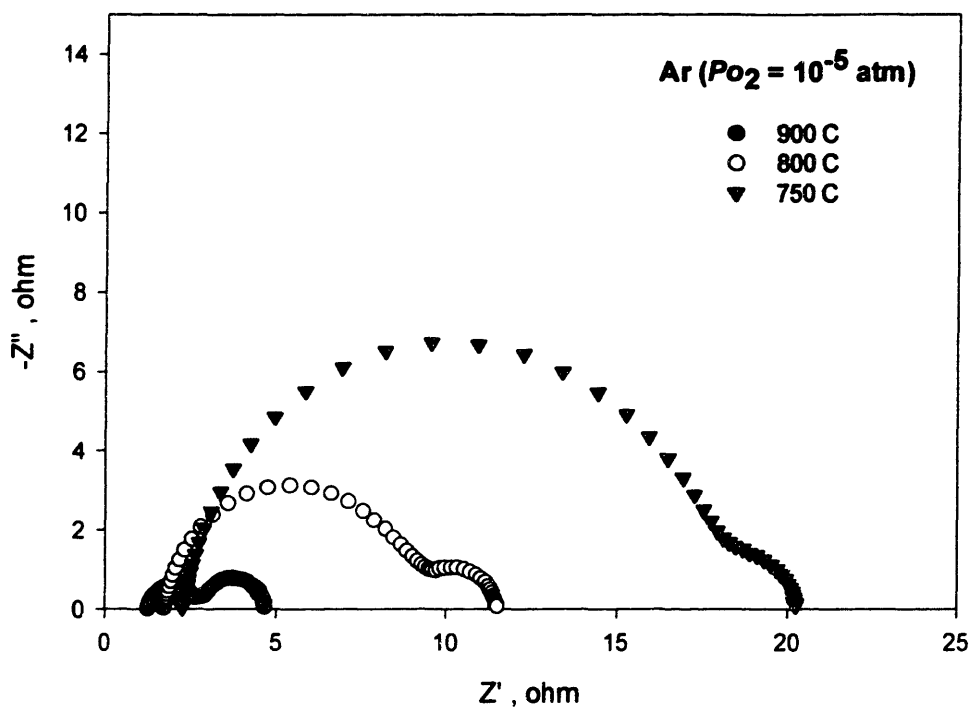


Figure 6.11 Spectra for the Pd/YSZ interface at different temperatures in Argon.

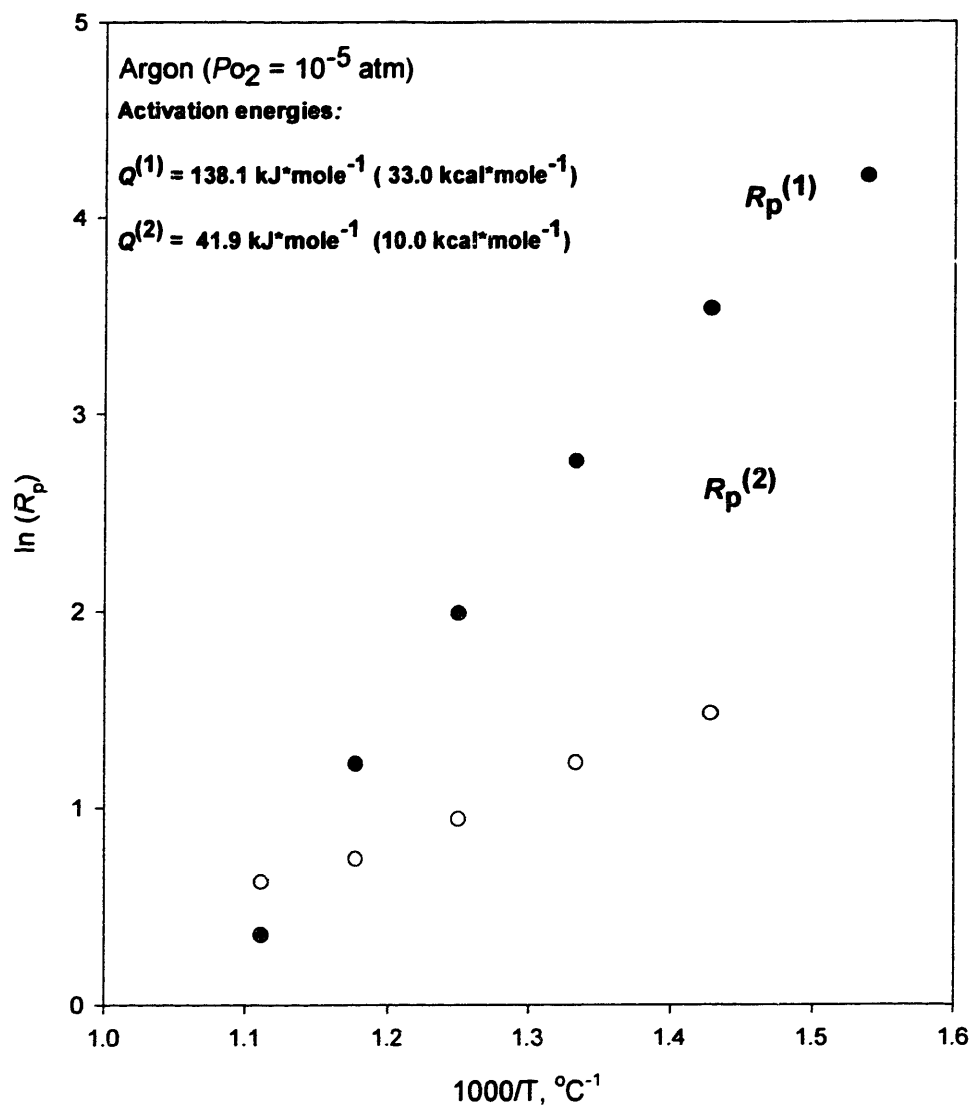


Figure 6.12. Temperature dependence of $\ln(R_p)$ under Argon.

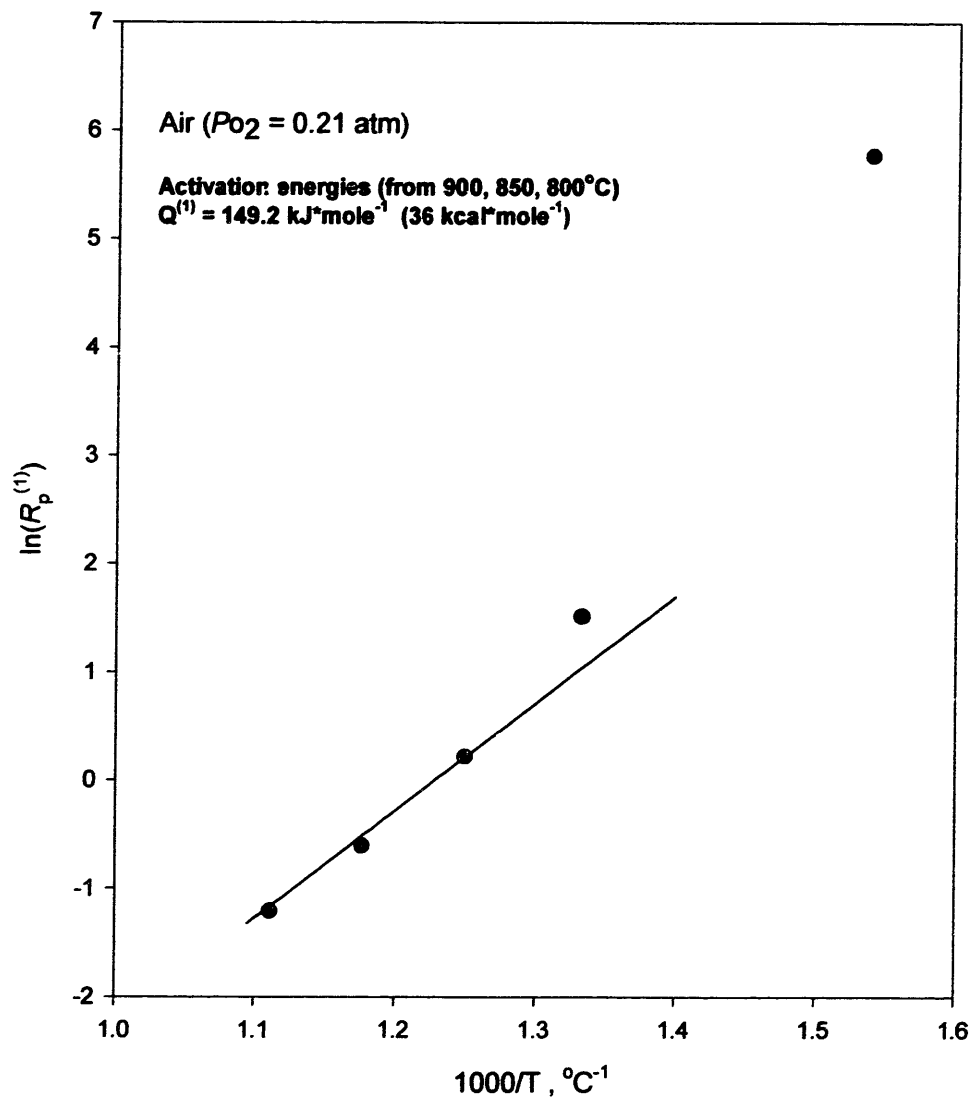


Figure 6.13. Temperature dependency of $\ln(R_p)$ under air.

According to the thermodynamic data (figure 6.1), PdO is stable in air from around 770°C to room temperature. At 750°C and below, the impedance spectra taken in air increased with time. The behavior was similar to that of figure 6.7 (apart from the initial decrease in figure 6.7). This is consistent with the thermodynamic data. In figure 6.13, it can be seen that, above the temperature where oxidation cannot occur, the activation energy is close to that shown in figure 6.12. Below the oxidation temperature, there is a deviation. This can be attributed to the change in the interfacial process, since the chemistry (and possibly also the morphology) of the interface has changed due to oxidation.

6.1.3 Reaction model

Tables 6.1 and 6.2 below summarize the kinetic data in the region where PdO is thermodynamically unstable:

Table 6.1 Resistive elements.

element	Q (kJ / mole)	m , [$R_p=(Po_2)^m$]
$R_p^{(1)}$	144 ± 6	-0.37 ± 0.05
$R_p^{(2)}$	$42 \pm (?)$	-0.93 ± 0.02

Table 6.2 Capacitive elements.

element	Po_2 dependence	T dependence	range
C_{dl}	<i>no dependence</i>	<i>no dependence</i>	100 μ F
$C^{(2)}$	<i>increase with increasing Po_2</i>	<i>increase with decreasing T</i>	0.04-0.7 F

C_{dl} is identified as the double layer capacitance due to its invariance with respect to P_{O_2} . Its magnitude is comparable to the double layer values reported for Pt/YSZ interfaces (chapter 2.2.2). The basis for the analytical fitting was the circuit shown in figure 6.14.

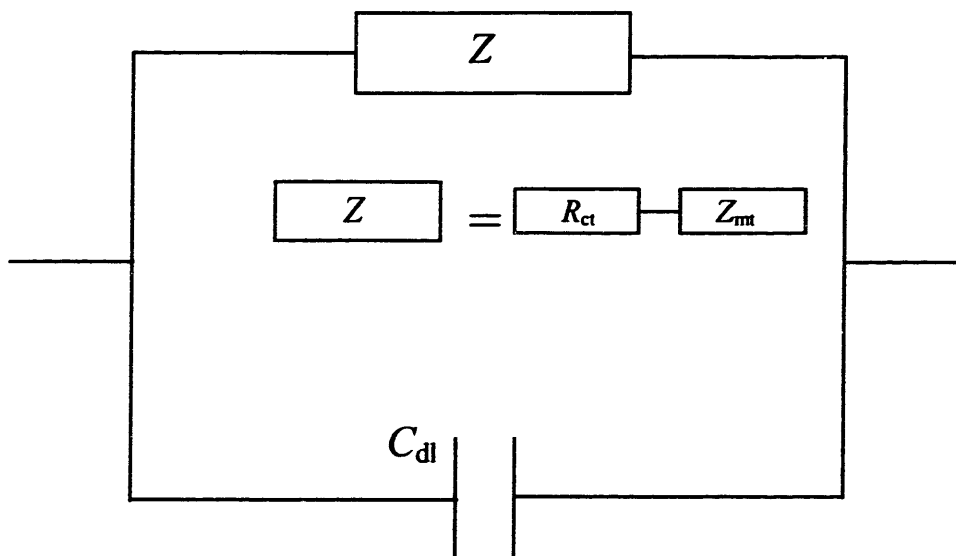


Figure 6.14. Basic equivalent circuit.

The impedance spectra of the Pd/YSZ interface were compared with the reaction models presented in chapter 2.2.2. The faradaic portion could then be decomposed into a purely ohmic part, R_{ct} , and a pseudocapacitive/resistance combination, Z_{mt} . All circuits indicated that the diameter of the high frequency arc equaled R_{ct} . The low frequency capacitive element (related to $C^{(2)}$) was much bigger (3-4 orders of magnitude) and thus all faradaic components, except R_{ct} , were shortened at high frequencies. $R_p^{(1)}$ was thus taken as R_{ct} .

6.1.3.1 Charge transfer

In the frequency region where charge transfer is visible in the impedance spectra, all other processes and reactions are in equilibrium. In chapter 2.2.2.1 it was shown how this would relate R_{ct} to P_{O_2} through an adsorption isotherm. From Table 6.1 it is shown that:

$$R_{ct} = const.(P_{O_2})^{-0.37} \quad (6.1)$$

Equation (6.1) can now be compared to equations (2.16) and (2.17). Since the exponent is negative, one may conclude that the surface coverage is low ($1 - \theta_{eq} = 1$). The activation energy of the charge transfer process can be calculated from the apparent activation energy Q using equation (2.18): E_r (kJ / mole) = $144 + 0.37 * \Delta H_{ads}$. ΔH_{ads} , for dissociative adsorption of oxygen on Palladium, has been reported to be 294 kJ / mole [Anderson 1975]. E_r is then 253 kJ / mole.

6.1.3.2 Mass transport

The three models described in chapter 2.2.2 were fitted to the measured spectra. All the circuit models simulated the two separated arcs I and II well. Therefore, the numerical fit was only taken as a last confirmation. The primary criterion was that the P_{O_2} and temperature dependencies should agree with the physical process. In the following, the three models are discussed with respect to the experimental data.

Adsorption kinetics as a possible mechanism can be discarded on the basis of the following argument: equivalent circuit fitting resulted in $R_p^{(2)}$ being equal to $R_{ads/des}$, which is inversely proportional to the rate of adsorption/desorption kinetics. $R_p^{(2)}$ decreases with increase in P_{O_2} (figures 6.4 and 6.5), demonstrating that the supply of oxygen is rate-

limiting, and thus adsorption kinetics is rate-limiting. One would expect adsorption to increase with lower temperature and, therefore, $R_p^{(2)}$ should decrease as $1/T$ increases. Figure 6.12 shows that this is not the case. In fact, the opposite is true. Thus the disagreement between the temperature and P_{O_2} dependencies allows this model to be discarded.

Surface diffusion qualitatively agrees with the P_{O_2} and temperature dependencies when the supply of oxygen to the TPB through surface diffusion is rate-limiting. However, $R_p^{(2)}$ is taken as R_{D0} (in equation 2.26), the exponent of the P_{O_2} dependency is close to -1 (Table 6.1). This is twice the ideal value for surface diffusion (-1/2) at low coverage. Another observation against surface diffusion is that the 45° phase angle is not encountered for arc II in any of the measured spectra. As an example, figure 6.15 shows the phase angle for the spectra taken at 900°C under Argon (where arc II is dominating).

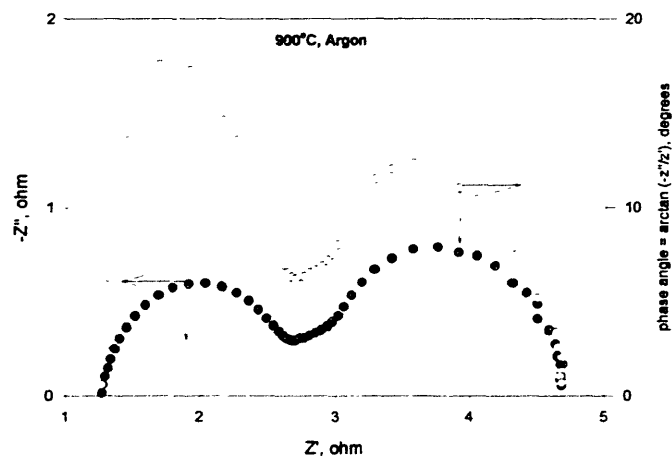


Figure 6.15. Phase angle for arc II in Argon at 900°C .

Lateral diffusion appears to be the most likely process based on the following observations. Although the fit is not excellent, the main features are simulated adequately (figure 6.16). A simple P_{O_2} dependence for $R_p^{(2)}$ can not be derived from equation (2.28). It is possible to predict, however that a higher P_{O_2} will lead to a steeper diffusion gradient in the metal/YSZ interface. It follows that the diffusion rate should increase, and therefore, the impedance associated with diffusion should decrease. If impedance is associated with a diffusion process it should decrease with increasing temperature. This is entirely in agreement with the experimental result shown in figure 6.12.

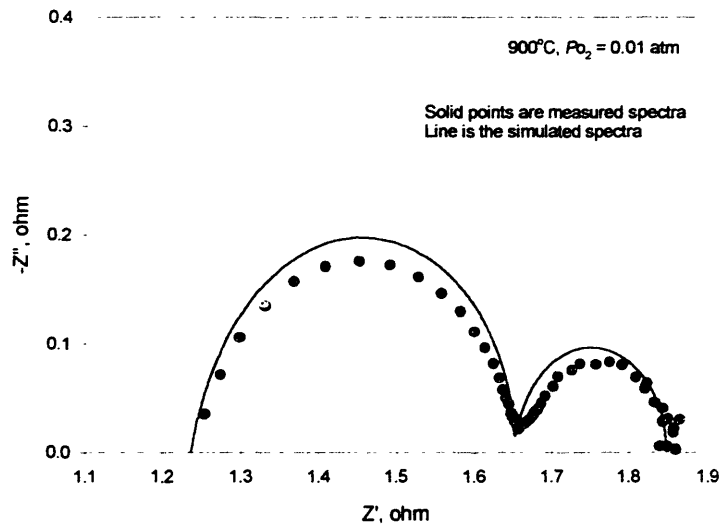


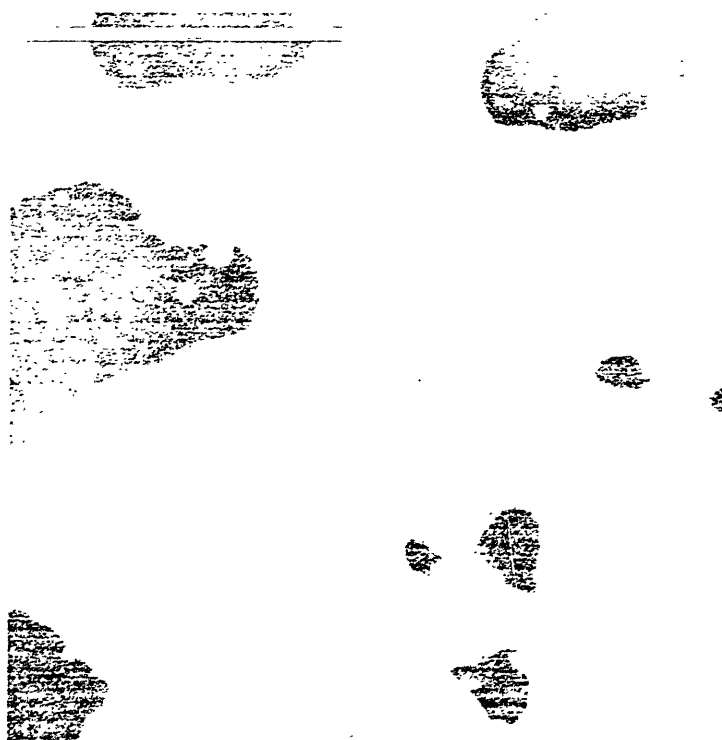
Figure 6.16. Simulated spectrum using equation (2.28) vs. real spectrum.

The choice between lateral and surface diffusion is not absolute, but the results of the microstructural study of the interface (presented in the next section) support interfacial-lateral diffusion over surface diffusion.

6.1.4. Microstructure

Figure 6.17 shows the microstructure of the Pd coating from above, and figure 6.18 shows fractured cross sections of the Pd/YSZ interface. The sample was prepared by first firing it in air to 900°C to remove all the binder material. It was then maintained at this temperature for 12 hours in Argon until all oxide phases decomposed. Finally, the sample was cooled down to room temperature in Argon. The material is representative of the electrodes used in all the electrochemical measurements of the unoxidized Pd electrode. The porous Pd coating was 2-3 μm thick and consisted of a single layer of sintered Pd grains. As seen from figure 6.17, the grains formed a continuous network on the electrolyte surface.

(a) Top view
X 1500
(light grains = Pd)



(b) Top view
X 8000
(light grains = Pd)

Figure 6.17. Top view of the open porosity.

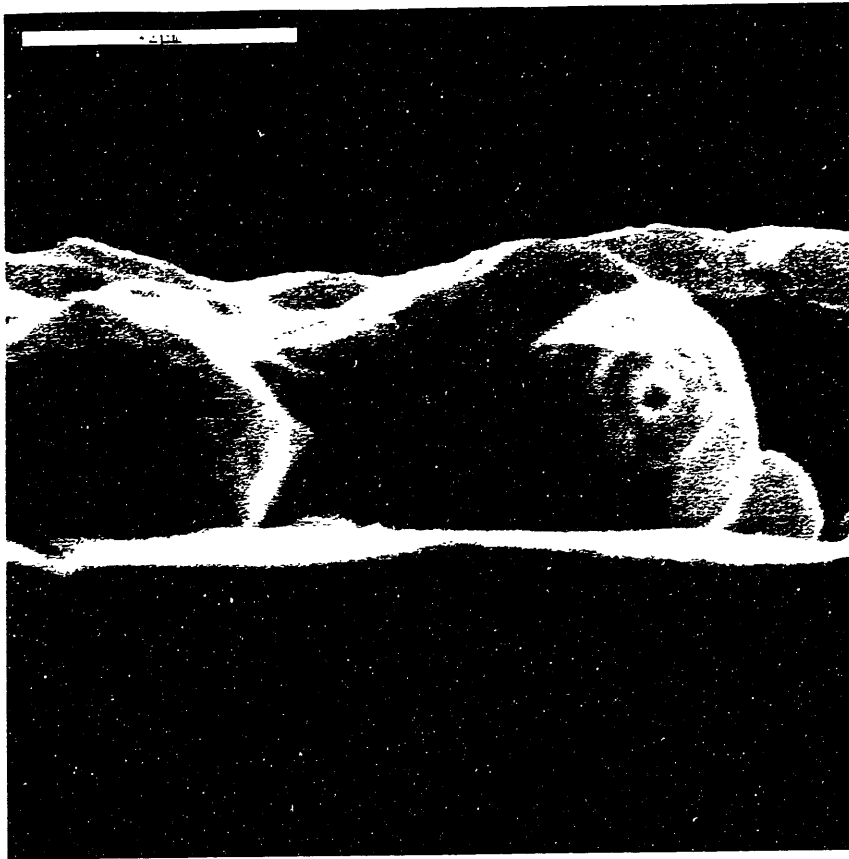


Figure 6.18. Cross section of the Pd/YSZ interface X 15000.

At the fractured interface, no extensive contact points with necks are visible. The Pd grains seem to make only a mechanical contact with the electrolyte. An example of this can be seen in figure 6.18. The open porosity is high so that it is reasonable to assume that the gas has excess everywhere except at the Pd/YSZ interface. It is hard to justify that a surface diffusion process from the adsorption sites to the TPB would be necessary. In addition, the Pd grains did not wet the electrolyte surface. As demonstrated schematically in figure 6.19b, this leads to a minimal total length of the TPB.

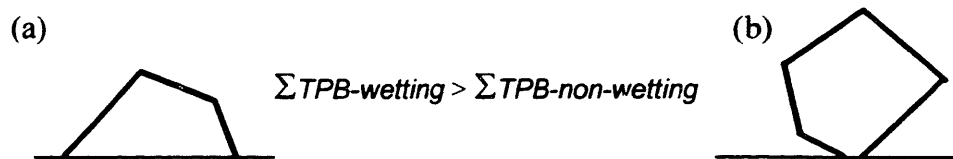


Figure 6.19. Comparison of TPB length between:
(a) a wetting grain and a (b) non-wetting grain.

As seen in figure 6.19b, a non-wetting grain has a large adsorption area but a small TPB length. This could lead to an extension of the charge transfer site by lateral diffusion in the Pd/YSZ interface.

6.1.5 Oxidation in air at 650°C

In order to study the influence of PdO on the exchange reaction, an experiment was done where an unoxidized sample was oxidized in air at 650°C. The evolution of the total overall polarization R_p ($R_p = R_p^{(1)} + R_p^{(2)}$) is shown in figure 6.20 as a function of time in a logarithmic scale.

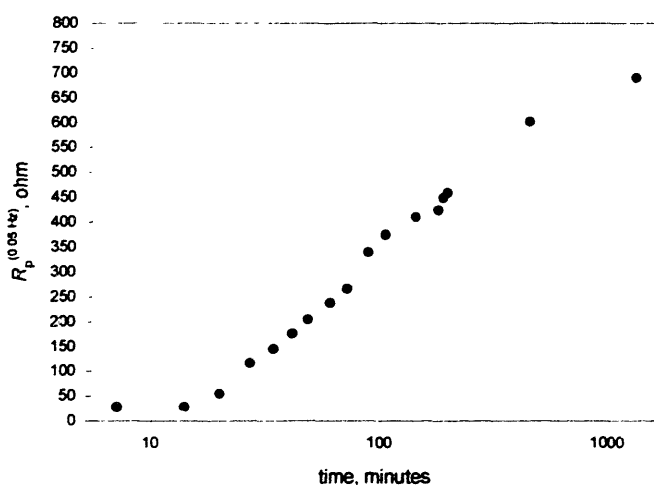


Figure 6.20. Polarization change with time after subjecting the electrode to air at 650°C.

Figure 6.21 shows a thermogravimetric measurement done with the Pd processed under the same conditions as the electrodes. Due to the amount of material needed to get an accurate record of the weight change, the Pd had to be scraped off the substrate. As seen from figure 6.21, after about 1% weight increase, the oxidation becomes very slow. The decay in the diffusion rate could be due to the fact that a diffusion-limited process

becomes rate-limiting after the surface has been covered with an oxide layer. The change in microstructure after 1 hour and after 24 hours of exposure to air at 650°C are shown in figures 6.22 and 6.23 respectively.

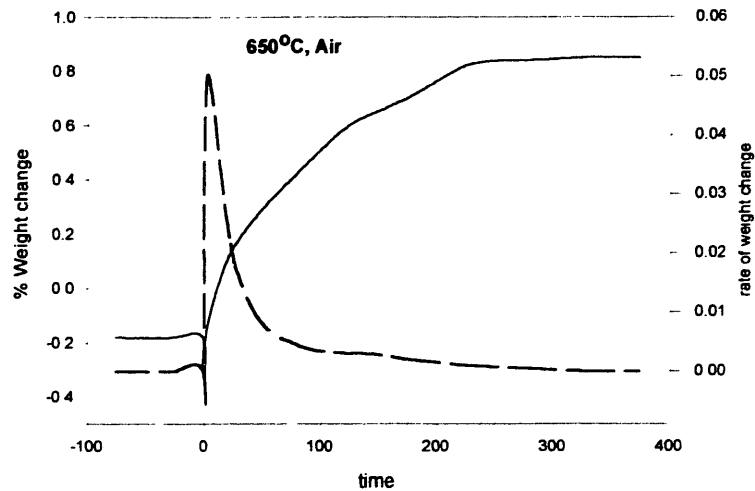


Figure 6.21. Thermogravimetric data of Pd in air at 650°C. The solid line shows weight change with time and the dashed line shows the rate of weight change with time.

The increase in R_p shown in figure 6.20 cannot be caused by an inhibition of gas access, since figures 6.21 and 6.22 show that a high open porosity is maintained even after oxidation. Neither can it be caused by an increase in the sheet resistance since PdO is a good semi-conductor above 227°C [Okamoto 1967]. Using the room temperature resistivity [Rogers 1971], a layer of 2 μm PdO should have a resistance of 0.2 ohm. The activation energy was reported to be only 3.8-9.7 kJ/mol [Rogers 1971]. Considering the high temperatures and the fact that only a small fraction of the Pd coating oxidized, the resistance would be expected to be lower. Furthermore, if there were an increase in the

ohmic resistance, the high frequency real axis intercept of the impedance spectra should also have increased. No such increase was observed during oxidation. The most plausible cause is a drastic change in the electrocatalytic properties of the electrode, caused by the surface layer of PdO.

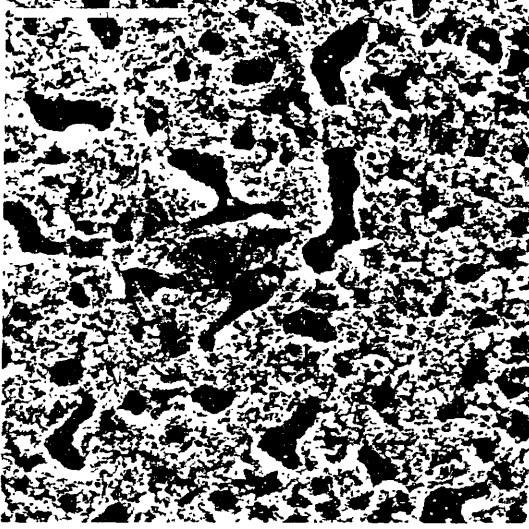
The oxide layer could affect either the adsorption or surface diffusion on the electrode surface or the charge transfer sites. Figure 6.21 shows, however, that the oxidation stops (or becomes very slow) after about 400 minutes. At this stage the surface is probably covered with a PdO layer and further oxidation is controlled by diffusion.

If the effect of PdO on the electrode impedance was solely due to adsorption or surface diffusion inhibition, then R_p vs. time should also stop increasing after 400 minutes. Figure 6.22 shows that R_p continues to rise even after 22 hours (although at a decreasing rate). The difference could be due to the fact that the bottom of the Pd-electrode is covered by the YSZ-electrolyte. This interfacial area may take longer to be covered with PdO. The lateral diffusion model, that was discussed in the previous section, assumes that the interfacial area is used for charge transfer. If, indeed, PdO is less electrocatalytic than Pd, it would be consistent with the fact that the impedance continues to increase as the interface is being covered with PdO.

The electrode surface in figures 6.22 and 6.23 seems to be covered with a growing crystalline phase resulting from the oxidation (compare with the unoxidized microstructure of figures 6.17-6.18). At the cross section (figures 6.22c and 6.23c), there appear a number of small but pronounced contacts between the Pd-PdO coating and the YSZ electrolyte. Higher magnification revealed possible neck formations at these contact

points, but due to the lack of contrast as a result of the high magnification, the image is not very clear. However, comparing the interfaces of figures 6.18 and 6.23, it is certain that the oxidation has affected the contact between the electrode and the electrolyte severely. It is likely that this affects the rate of lateral diffusion of oxygen along the Pd/YSZ interface. This could be the primary cause for the impedance increase in figure 6.20.

(a) Top view
X 1500



(b) Top view
X 8000



(c) Cross section (Pd/YSZ interface)
X 15000



(d) Cross section (Pd/YSZ interface)
X 1500

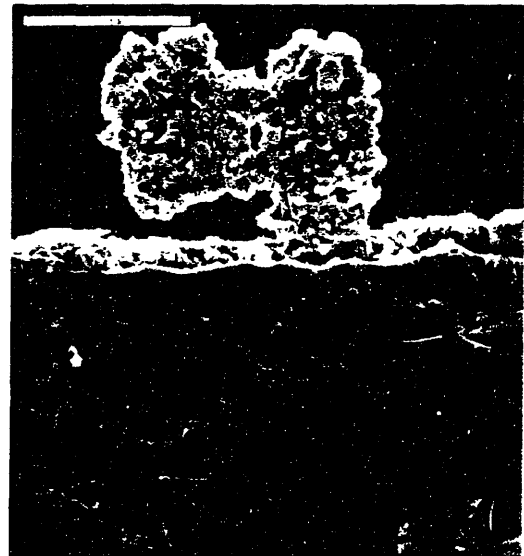
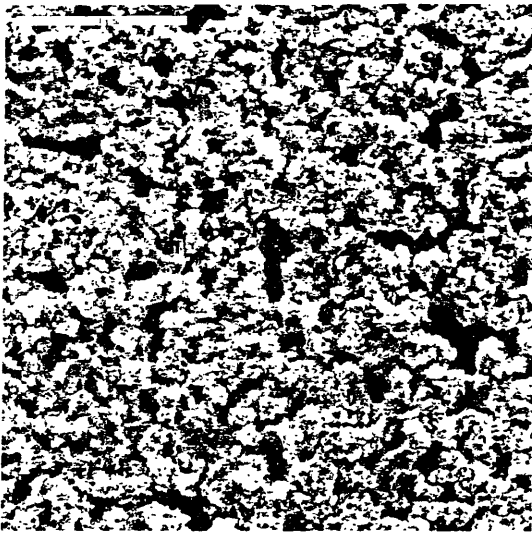


Figure 6.22. Pd coating subjected to air at 650°C for 1 hour.

(a) Top view
X 1500



(b) Top view
X 8000



(c) Cross section (Pd/YSZ interface)
X 15000

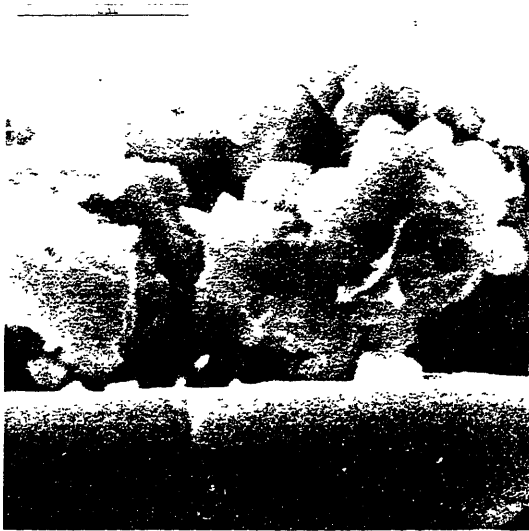


Figure 6.23. Pd coating subjected to air at 650°C for 24 hours.

6.2 Effect of Direct Current

The influence of direct current on the interfacial impedance spectrum was investigated in two ways: under isobaric conditions in air from 900 to 650°C, and under isothermal conditions at 700°C. The rationale for varying the temperature and P_{O_2} is the following: if the current effect is related to the formation/decomposition of Pd-O compounds, then the stability of PdO should influence the magnitude of the effect. According to figure 6.1, an anodic current should have a larger effect at higher P_{O_2} and/or lower temperature.

6.2.1 Effect of Temperature

Anodic currents of 10 mA were passed for 5 minutes to study the possible effects on the interfacial impedance after current interruption. At 900°C there was no effect on the impedance. At 850°C and 800°C the electrode impedance increased slightly after current interruption (figure 6.24). The magnitude of the change was larger at 800°C than at 850°C. No recovery was observed. An anodic current supplies oxygen at the electrode. Following the arguments of chapter 5, the local increase in P_{O_2} could cause the formation of oxygen containing species (OCS) that partially block the electrode reaction. The previous section has shown how the formation of PdO from oxygen supplied by the atmosphere increases the electrode impedance by affecting the electrocatalytic properties of the Pd/YSZ interface. An anodic current supplies oxygen directly to the charge transfer sites and thus a profound effect is expected upon the formation of any OCS.

At 700°C the current-induced change increased dramatically (figure 6.25 a). After current interruption there was a recovery period in which the impedance shrank. The final steady state spectrum was much larger than the original spectrum. From figure 6.1 it can be seen that PdO is thermodynamically stable in air at 700°C. It is therefore conceivable that the large effect of the anodic current at this temperature is associated with the formation of PdO.

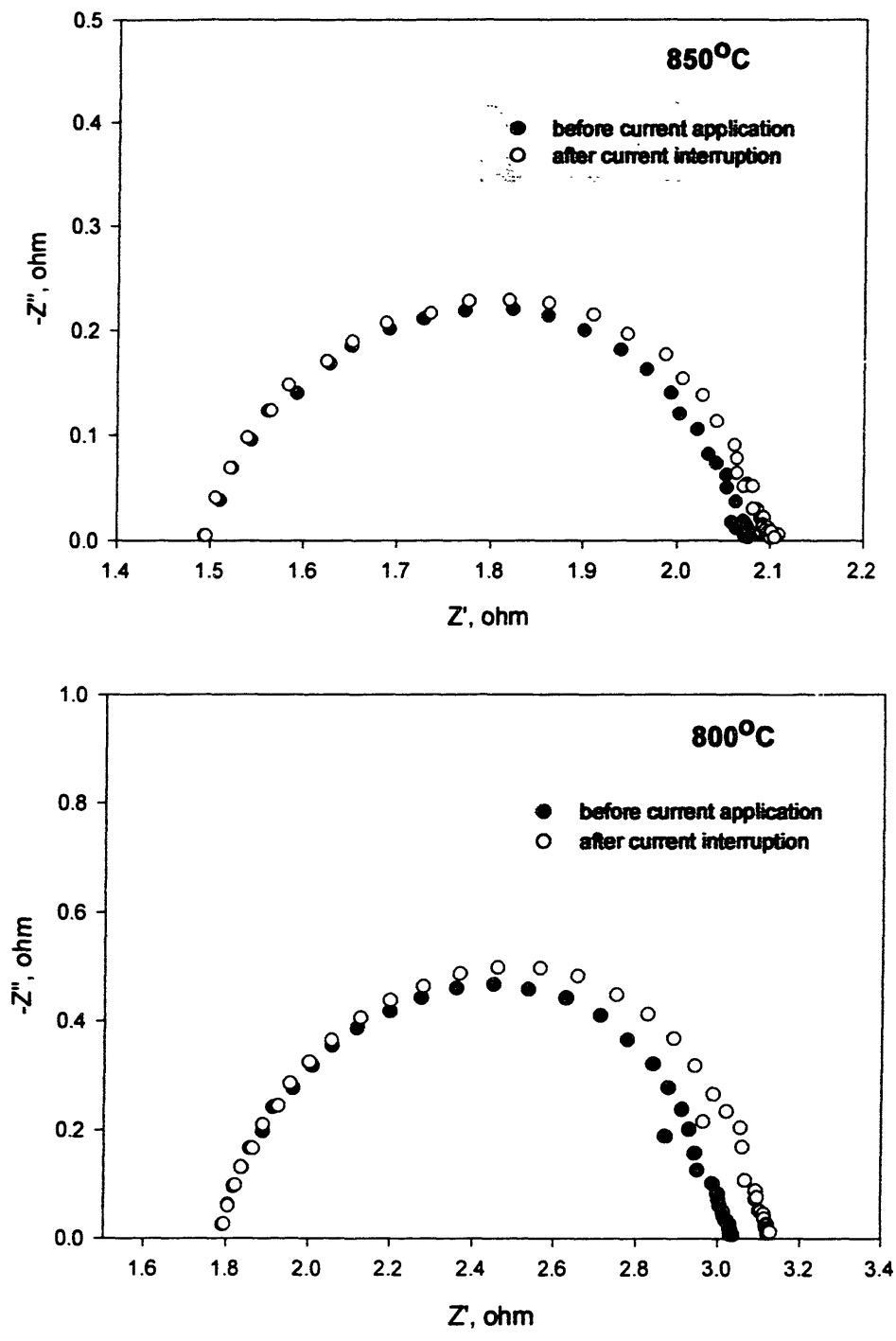


Figure 6.24. Effect of an anodic current of 10 mA passed for 5 minutes on the impedance spectra of the Pd/YSZ interface in air: (a) 850°C; (b) 800°C.

6.2.2 Effect of Oxygen Partial Pressure at 700°C

The current-induced change in the interfacial impedance is shown for 4 different P_{O_2} conditions in figure 6.25. At $P_{O_2} > 0.05$ atm, PdO is thermodynamically stable. In order to separate the effect on the impedance, due to oxidation from the gas phase, and the effect induced by current, the electrodes were equilibrated before passing current. Between each P_{O_2} , the electrodes were heated to 900°C under Argon in order to decompose all OCS formed during the previous run.

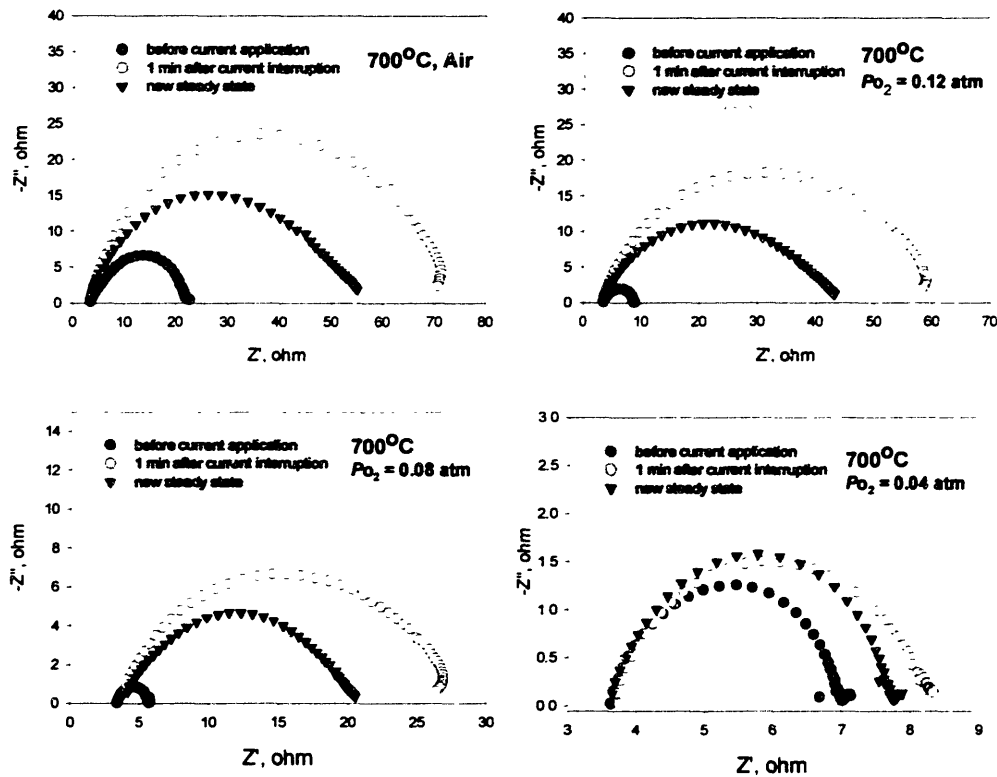


Figure 6.25. Effect of an anodic current of 10 mA passed for 5 minutes on the impedance spectra of the Pd/YSZ interface.

At $P_{O_2} = 0.21$ and 0.12 , the magnitude of the increase and the remnant hysteresis were comparable. At lower P_{O_2} , however, the current-induced effect decreased. This is reasonable since the OCS formation is expected to be favored under more oxidizing conditions. For example, it can be seen in figure 6.1 that the driving force for PdO formation would, for a given temperature and current, be higher at a higher P_{O_2} .

6.3. Summary of the Results on the Pd/YSZ Interface

When PdO is thermodynamically unstable, the oxygen exchange at the Pd/YSZ interface proceeds according to a mixed mechanism of charge transfer and lateral diffusion across the Pd/YSZ interface. When PdO is thermodynamically stable and the electrode surface oxidized, the oxygen exchange across Pd/YSZ is partially blocked. The polarization shift due to anodic currents increases with decrease in temperature and increase in P_{O_2} due to OCS formation at the charge-transfer sites. The current-induced effect on the oxygen-exchange reaction is observable under the conditions when PdO is thermodynamically stable. The model presented in chapter 5 stated that the current induced impedance change is due to the formation/depletion of OCS at the charge transfer sites. The presence of OCS lowers the rate of the oxygen-exchange reaction. If PdO is part of the OCS that contributes in blocking the reaction sites then the model predicts that the current-induced modification on the interfacial impedance should be more prevalent when PdO is thermodynamically stable. The results on Pd/YSZ show that the impedance increase due to OCS formation is mainly present in the T and P_{O_2} regimes where PdO is stable. The experiments thus confirm the model.

Chapter 7

Conclusions

The effect of temperature, oxygen partial pressure, current and electrode microstructure on the interfacial impedance of $\text{Pt}/(\text{Y}_2\text{O}_3)_{0.08}(\text{ZrO}_2)_{0.92}$ and $\text{Pd}/(\text{Y}_2\text{O}_3)_{0.08}(\text{ZrO}_2)_{0.92}$ has been studied. The change in oxygen concentration due to oxygen supply/depletion induced by direct current was studied by monitoring the impedance in the time domain after current interruption. For the first time it is shown that the kinetics of the charge-transfer reaction is influenced by variations in the oxygen potential at the charge transfer sites. The reason for this is that the metal (Pt or Pd) at the charge transfer sites (triple phase boundaries between gas/YSZ/metal) react with oxygen to form oxygen-containing species (OCS). As a result of this reaction, the electrocatalytic properties that govern the kinetics of the exchange reaction are altered.

Near-equilibrium experiments show that at the $\text{Pt}/(\text{Y}_2\text{O}_3)_{0.08}(\text{ZrO}_2)_{0.92}$ interface, the charge-transfer reaction obeys a P_{O_2} dependence in agreement with a Langmuir adsorption isotherm when the system is heated from room temperature.

Distinctly different behaviors were observed for the Pt/(Y₂O₃)_{0.08}(ZrO₂)_{0.92} interfacial impedance in the temperature range 800°C < T < 1050°C when heated from room temperature compared to when cooled from 1050°C. When heating from room temperature, the impedance spectra are modified after passing direct currents. Anodic currents increase the size of the impedance spectra and cathodic currents decrease the size of the impedance spectra. At 1050°C, the impedance decreases with time. Upon cooling the impedance spectra are smaller than the ones at the same temperature when heating from room temperature. Furthermore, the current induced effect was not observable until the system was cooled below 850°C.

A two-path model is proposed for the transfer of oxygen at gas/Pt/(Y₂O₃)_{0.08}(ZrO₂)_{0.92} (TPB) interfaces. One of them is a fast path that involves clean TPB sites. The other path involves the participation of oxygen-containing species (OCS) at the TPB sites. The OCS partially block the oxygen-exchange reaction. The concentration of OCS is related to the thermal, current and gas exposure history of the interface. Anodic currents increase the OCS concentration by supplying oxygen to the TPB. Therefore, the interfacial impedance increases after anodic currents. Cathodic currents deplete oxygen from the TPB and thereby lower the OCS concentration. This results in a decrease in the interfacial impedance. An analysis of the current-induced modification suggests that at least two types of OCS are present: a loosely bonded type, (Pt)_n–O and a stable, oxide-like OCS, (Pt)_n–O. The observed decrease in impedance with time at 1050°C is linked to the decomposition and stripping of the OCS. Due to the OCS-stripped state of the Pt/YSZ interface the interfacial impedance is smaller when the cell is cooled from 1050°C

compared to when it is heated from room temperature. Upon cooling the current-induced modification of the impedance for the OCS-stripped interface is absent until the system is cooled below 850°C.

The impedance for the Pd/(Y₂O₃)_{0.08}(ZrO₂)_{0.92} interface, near equilibrium conditions, consists of two semi-circles. An analysis of the *P*O₂ and temperature dependencies show that the first one is related to the charge-transfer at the TPB and the second arc to lateral diffusion and charge transfer at the Pd/YSZ two-phase boundary. The charge transfer is calculated from the high-frequency region and has an activation energy of 253 kJ/mole. The *P*O₂ dependency of the charge-transfer resistance show that dissociative Langmuir adsorption is obeyed. When PdO is thermodynamically stable, the impedance increases with time due to PdO formation leading to a lowering of the electrocatalytic properties of the electrode. In this region, the shape of the impedance spectra changes suggesting that the charge transfer mechanism no longer remains the same. The current-induced impedance change is observable only near and within the stability region of PdO suggesting that PdO may be a major constituent of the OCS at the Pd/(Y₂O₃)_{0.08}(ZrO₂)_{0.92} interface.

Chapter 8

Implications for Electrochemical Devices and Future Work

8.1. Implications

The results of this thesis show that the rate of the oxygen-exchange reaction across the YSZ/metal interface is modified after passing direct currents. When oxygen-containing species (OCS) are present at the charge-transfer sites, the oxygen transfer is partially inhibited. The presence of the OCS is determined by their thermodynamic stability. Direct currents, depending on the direction, supply or deplete oxygen at the charge-transfer sites and can thereby alter the thermodynamic stability of the OCS. Thus, under certain temperature and oxygen-partial-pressure regimes, the impedance associated with the mechanism of oxygen transfer changes depending on the history of current passage. This has important consequences on the operation and processing of the YSZ-based devices that are described in chapter 1.

The electrocatalytic sites at the anode in SOFC are the Ni-YSZ contact points. Based on the results observed for the Pt/YSZ interfaces, and Pd/YSZ interfaces it is very likely that, Ni being less noble than Pt and Pd will interact with oxygen when the SOFC draws a certain current. Since the anode is exposed to a highly reducing atmosphere it is possible that the triple phase boundaries, Ni/YSZ/gas, is not affected. However, the two-phase boundaries Ni/YSZ are likely to be affected by the oxygen supply. This may happen at the region near the triple-phase contact line as shown in figure 8.1.

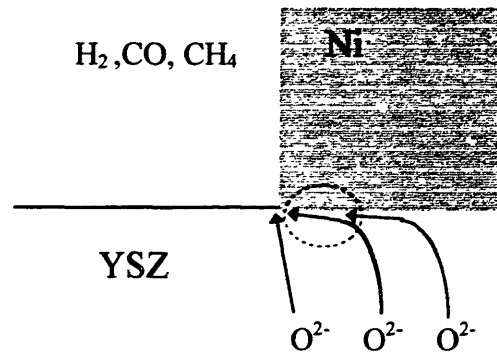


Figure 8.1 NiO formation near at the Ni/YSZ interface within the dotted region.

If NiO forms at the interface, it is likely that the contact between Ni and YSZ grains will change. This would change the pore geometry which could affect the electrocatalytic properties of the reaction site. It would be interesting to investigate the change in the interfacial impedance of the Ni-YSZ/YSZ interface after current interruption. If this could be done *in situ* in an environmental SEM equipped with a hot stage, then the contact between Ni-grains and the electrolyte substrate could be monitored before, after and while the current is passed.

State of the art SOFC use LMN (Doped Lanthanum Manganite) which is an electron-conducting-ceramic-perovskite oxide as cathode. Unlike metal electrodes such as Pt, Pd or Ni, that do not dissolve oxygen, these perovskites exhibit under certain P_{O_2} and temperature ranges some ionic-oxygen conductivity. If a direct current results in a local P_{O_2} change it is very likely that the charge-transfer region as well as the conductivity is affected. A similar study to the present one, where the interfacial impedance is monitored in the time domain after passing currents, would be an interesting research topic to pursue as future work. The effect of current at various oxygen partial pressures and temperatures would reveal the source of a current induced effect. In the case of LMN, the cathodic conditions could induce mixed-ionic/electronic conductivity near the LMN/YSZ interface. The extent of the affected region (the dark-gray region in figure 8.2b) would depend on the cathodic current density. The oxygen atoms could then find an alternative path to reach the reaction sites via the bulk LMN. The driving force for this is the oxygen ion gradient that exists in the LMN due to the depletion of oxygen by the cathodic current.

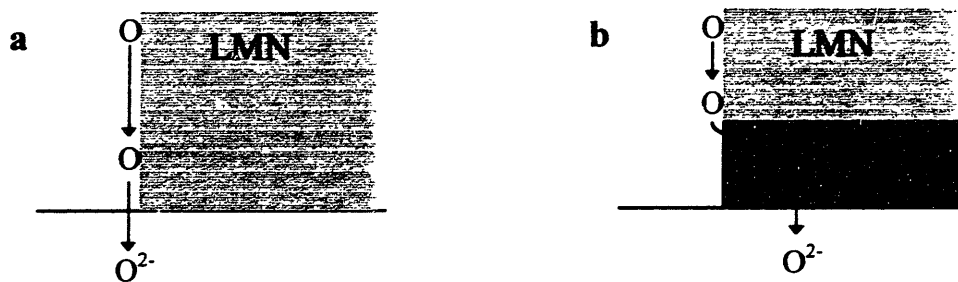


Figure 8.2. Exchange reaction at the LMN electrode (a) near-equilibrium conditions (b) dynamic (cathodic) conditions.

A similar experimental procedure as the one used in this work could be used to measure the effect of direct currents on the interfacial impedance of the LMN/YSZ interface.

The use of Pt-YSZ amperometric sensors necessitates a precise knowledge of the kinetic conditions near the Pt/YSZ/gas interface. In amperometric sensors, the concentration of species is calculated from the limiting current I_L . If the effective reaction zone is influenced by the current, data analysis will be difficult. The impedance at the diffusion-limited-current regime will not be stable with time if the effective reaction area keeps changing. As a result the limiting current may not be observed.

Pt-YSZ amperometric sensors are best operated above 850°C after a heat treatment at 1050°C. In this regime, the influence of current on the oxygen-transfer reaction, due to OCS formation/depletion, is not observed. It should be cautioned however that as the local P_{O_2} becomes higher the OCS becomes more stable. Hence, although the current-induced modification (due to OCS formation) was not observed between 1050°C and 850°C upon cooling for the anodic currents used in this work, higher currents may increase the local P_{O_2} to such an extent that OCS may form. Pd-based sensors may be an alternative since the current-induced polarization shift is absent when PdO is unstable. The thermodynamic conditions of PdO is more well known than the Pt-O compounds. Hence, as long as PdO is unstable it may be safer to use Pd-based electrodes in amperometric sensors.

In the present work, it was not possible to obtain the local P_{O_2} at the charge-transfer sites. If one could deposit micro electrodes at different locations, along the

metal/YSZ interface, then the local P_{O_2} could be measured. If the local P_{O_2} and impedance could be monitored simultaneously, then the OCS formation/decay could be followed along with the change in P_{O_2} . The thermodynamic data for the OCS can then be directly correlated with the change in P_{O_2} and the impedance.

8.2. Future Work

This work has shown that the oxygen-transfer kinetics across Pt/YSZ and Pd/YSZ is modified by direct currents. The temperature and P_{O_2} regimes where this modification is encountered suggest that the reason for the phenomenon is that oxygen reacts with the metal near the charge transfer sites. The dependency of the extent of the current-induced modification on current direction and magnitude supports this explanation. In the case of Pd there is sufficient thermodynamic data to support that formation/depletion of PdO is at least partially responsible for the current-induced effect on charge transfer kinetics. Microstructural studies confirm the formation of PdO scales under appropriate thermodynamic and kinetic conditions. Pt is more resistant to oxidation than Pd and it is hard to identify what types of oxygen-containing species are responsible for the current-induced effect. A logical continuation of this project would be to physically identify compounds that oxygen forms with Pt at the charge-transfer sites when anodic current is passed. This would require an experimental setup that enables the use of spectroscopic techniques at high temperature. If this was possible, then the Pt-surface at the TPB in an electrochemical cell could be monitored while current was being passed. A possible

spectroscopic technique would be XPS which could be used to monitor the oxidation state of Pt.

Both Pd and Pt adsorb oxygen whereas Au does not. It would therefore be interesting to see if the transient-reversible part of the current-induced modification is absent in cells where Au constitutes the metal electrode. For this purpose, identical experiments as those that are presented here for Pt/YSZ and Pd/YSZ could be performed for the Au/YSZ system.

Appendix

I. Processing of Ni-YSZ Cermets

The following section outlines the slurry-coating process through which the Ni-YSZ cermets were processed. Rheological characterization of the slurries were made in order to control the cermet structure. Details on the rheological measurements are published in: Sridhar and U.B. Pal, *Powder Technology*, **88** (1996) 173.

The viscosity of the slurry was altered by varying different powder to liquid ratios. The ideal ratio was found to be between 0.12 and 0.13 vol% powder (figure A1).

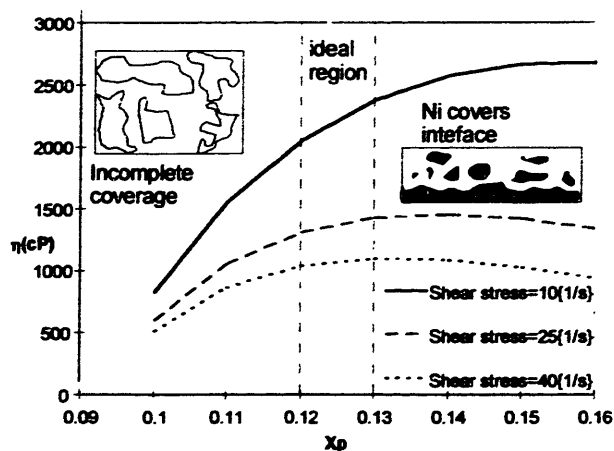


Figure A1. The viscosity and powder/liquid ratio region were final cermet structure was optimized with respect to the electrolyte coverage and adherence.

Higher powder concentrations resulted in that most of the Ni settled and there was a dense Ni layer next to the electrolyte in the final cermet structure. Due to the thermal mismatch between Ni and YSZ the cermet would then easily peel off from the electrolyte substrate. When powder concentration was lower than 12% there would appear large patches on the electrolyte that were uncovered with cermet.

The PVA (Polyvinyl alcohol) solution was prepared by heating a solution of deionized water with 6 weight% PVA powder (Dupont, Elvanol 75-15) to 80°C while continuously stirring the solution. The slurry solutions were prepared by dispersing known mixtures of Ni and YSZ powders in a known volume of PVA solution. The powder was added in 4 batches. Between each addition the dispersion was milled in a SWECO-Vibromill for 5 minutes. After all the powder was added, the dispersion was milled for 60 minutes. Milling for longer times did not result in any change in the rheological properties. Dispersion by stirring manually required much longer times to achieve the same rheological properties. No grinding media was used since this would cause the soft filamentary Ni particles to break.

After milling, the slurry was immediately coated on one side of a YSZ electrolyte substrate. The coating was then passed through a blade, adjusted at a constant height to achieve an even coating after which it was left to dry for 24 hours. The coated substrate was then sintered at 1100°C for 17 hours under an atmosphere of forming gas (N₂ with 5%H₂) with 5% H₂O followed by cooling under an atmosphere of pure forming gas. To increase the YSZ content especially at the electrolyte/cermet interface and obtain long time adherence, the substrate was then placed inside a vacuum chamber and infiltrated

with a solution containing 30 vol.% YSZ, and 70 vol.% of a deionized water and 4N HNO₃ mixture. Finally the coating was sintered at 1200°C for 7 hours in forming gas. The final cermet structure after this operation typically had 60 vol.% Ni which is above the limit (30 vol.%) required according to the percolation theory for the cermet electronic conductivity to be close to that of Ni.

The YSZ in the initial powder and more so the YSZ in the infiltration solution contributes to the stability of the cermet and its adherence to the electrolyte. Due to incompatible thermal expansion, Ni will not by itself adhere to YSZ substrates at high operating temperatures of the SOFC (800°C-1000°C).

II. Temperature Dependency of R_p for the Pt/YSZ Interface

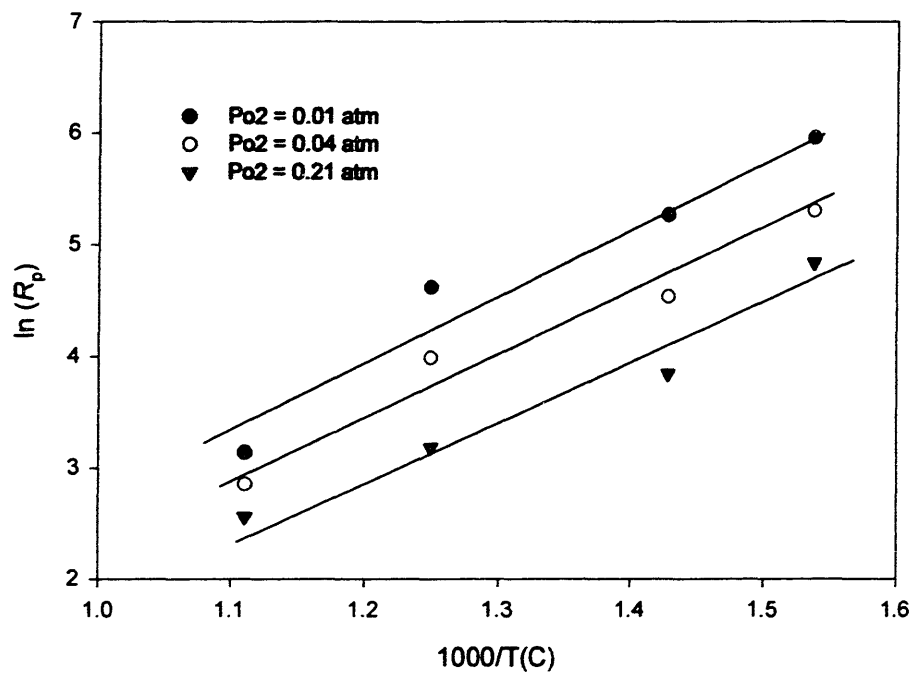


Figure A2. The temperature-dependency of R_p for the Pt/YSZ interface.

References

- J.R. Anderson. *Structure of Metallic Catalysts*, AP press, NY, 13, (1975).
- G.B.Barbi. *Ber. Bunsenges. Phys. Chem.*, **99**, 741 (1995).
- A.J. Bard and L.R. Faulkner, *Electrochemical Methods*, John Wiley & Sons, chapter 9. (1980)
- Ihsan Barin, *Thermodynamic Data of pure Substances*, VCH,1168., (1993)
- J.E. Bauerle. *J. Phys. Chem. Solids*, **30**, 2657 (1969)
- J.Baumard and P. Abelard, *Science and Technology of Zirconia II*, edited by: N. Claussen, M. Ruhe and A.H. Heuer, Acer, Columbus, OH, 555 (1984)
- B.J. Berry, *Surface Science*, **120**, 409 (1982).
- J. Bockris and A.K.N. Reddy, *Modern Electrochemistry*, Vol. 2, Chapter 9 (1977).
- B.A. Boukamp, B.A. Van Hassel, I.C. Virke, K.J. De Vries and A.J. Burggraaf, *Electrochimica Acta* **38**, 1817 (1993).
- D. Braunshtein, D.S. Tannhauser and I. Reiss, *J. Electrochem. Soc.*, **128**, 82 (1981).
- P.G. Bruce, *Solid State Electrochemistry*, Cambridge University Press, (1995)
- B.J. Christensen, R.T. Coverdale, R.A. Olson, S.J. Ford, E.J. Garboczi, H.M. Jennings and T.O. Mason, *J. Am. Ceram. Soc.*, **77**, 2789, (1994)
- C.I. Duval, *Inorganic Thermogravimetric Analysis*, 2nd edition, Amsterdam, Elsevier Pub. Co., 586. (1963)
- T.H. Etsell and S.N. Flengas, *J. Electrochem. Soc.*, **11**, 1890 (1971).
- D.R. Franceschetti and A.P. Ross, *Appl. Phys. A* **49**, 111 (1989).
- C. Gabrielli, Identification of Electrochemical Processes by Frequency Response Analysis (Solatron Instruments Technical Report # 004/83, Issue 2, 15 (1984).
- J.L. Gland, *Surface Science*, **93**, 487 (1980A).
- J.L. Gland, B.A. Sexton and G.B. Fisher, *Surface Science*, **95**, 587 (1980B).

- W. Gopel, H.-D. Wiemhofer, *Ber. Bunsenges. Phys. Chem.*, **94**, 981 (1990).
- T.M. Gür, I.D. Raistrick and D. A. Huggins, *J. Electrochem. Soc.*, **127**, 2620 (1980).
- A. Hammouche, E. Siebert and M. Kleitz and A. Hamman, 1st International Symposium on SOFC, edited by S.C. Singhal, The Electrochemical Society Inc., Pennington, NJ, 265. (1984)
- B.A. van Hassel, B.A. Boukamp and A.J. Burggraaf, *Solid State Ionics*, **48**, 139 (1991).
- F.Hund, *Z. Electrochem. Angew. Physik. Chem.*, **55**, 365 (1951)
- H.S. Isaacs, L.J. Hurer, E.J.L Schouler and C.Y. Yang, *Solid State Ionics* **3/4**, 503 (1981).
- S. Jain, T.T. Kodas and M. Hampden-Smith, *J. Electrochem. Soc.*, **144**, 1222 (1997).
- K. Kinoshita, F.R. McLarnon and E.J. Cairns, *Fuel Cell Handbook*. DOE/METC-8816096 (DE88010252) Distribution Category UC-110 (1988).
- M. Kleitz, *Solid State Ionics* **3/4**, 513 (1981).
- F.A. Kröger, *The Chemistry of Imperfect Crystals*, 2nd edition, North-Holland Publ. Co., Amsterdam (1974)
- T. Kudo and K. Fueki, *Solid State Ionics*, VCH/Kodansha, 67 (1990)
- B.L. Kuzin and M.A. Komarov, *Solid State Ionics*, **39**, 163 (1990).
- S. Ladas, S. Kennou, S. Bebelis, C. G. Vayenas, *J. Phys. Chem.*, **97**, 8845 (1993).
- J.R Macdonald, *Impedance Spectroscopy - Emphasizing Solid Materials and Systems*, John Wiley, 74, 71 (1987).
- N.Q. Minh and T.Takahashi, *Science and Technology of Ceramic Fuel Cells*, Elsevier, Chapter 1, (1995)
- J. Mizusaki, K. Amano, S. Yamauchi and K. Fueki, *Solid State Ionics*, **22**, 323 (1987).
- J. Mizusaki, *J. Electrochem. Soc.*, **141**, 2129 (1994)
- F.K. Moghadam and D.A. Stevenson, *J. Electrochem. Soc.*, **133**, 1329, (1986).
- J.R. Rostrup-Nielsen and D.L. Trimm, *J. Catal.*, **24**, 352, (1977)

- J.R. Rostrup-Nielsen, *J. Catal*, **85**, 31, (1984)
- I. Samsonov and G. Valentinovich, *The Oxide Handbook*, Plenum press, NY, 30 (1982).
- E. Siebert, *Electrochimica Acta*, **39**, 1621 (1994).
- P. Singh, R.J. Ruka, R.A. George, Direct Utilization of Hydrocarbon Fuels in High Temperature Solid Oxide Fuel Cells, R&D Paper 89-9V11-GRIN-P1, Westinghouse, PA. (1989)
- B. C. H. Steele. *Solid State Ionics*, **75**, 157 (1995).
- H.-D. Wiemhofer, *Ber. Bunsenges. Phys. Chem.*, **97**, 461 (1993).
- H.-D. Wiemhofer. *Solid State Ionics*, **75**, 167 (1995).
- H. Okamoto and T. Aso, *Jpn. J. Appl. Phys.*, **6**, 779 (1967)
- S. Pizzini, *Fast Ionic Transport in Solids*, ed. by W. van Gool, North Holland press, Amsterdam, 461, (1973).
- G.S. Popkirov, *Electrochimica Acta*, **4**, 1023 (1996)
- N.L. Robertson and J.N. Michaels, *J. Electrochem. Soc.*, **138**, 1494 (1991)
- D.B. Rogers, R.D. Shannon and J.L. Gillson, *J. Solid State Chem.*, **3**, 314 (1971)
- H. Schmalzried, *Solid State Reactions*, 2nd edition, (1981)
- P. Shewmon, *Diffusion in Solids*. 2nd edition, chapter 5 (1989)
- G.A Somorjai, *Chemistry in Two Dimensions - Surfaces*, p. 500, Cornell University Press, Ithaca and London (1981)
- S. Sridhar and U.B. Pal, *Powder Technology*, **88**, 173, (1996)
- D.L. Trimm, *Mathane Conversion, Studies in Surface Science and Catalysis 36*, edited by D.M. Bibby, C.D. Chang, R.F. Howe and S. Yurchak, Elsevier Publ. Co. 352, (1988)
- J. Van herle and A.J. McCoy, *Ber. Bunsenges. Phys. Chem.*, **97**, 470, (1993)
- C.G. Vayenas and N. Michaels, *Surface Science*, **120**, 405, (1982).

- C. G. Vayenas, I. V. Entekakis, S. Bebelis, S. Neophytides, *Ber. Bunsenges. Phys. Chem.*, **99**, 1393 (1995).
- O.J. Velle, T. Norby and P. Kofstad, *Solid State Ionics*, **47**, 161 (1991).
- M.J. Ververk and A.J. Burggraaf, *J. Electrochem. Soc.*, **130**, 76 (1983).
- D.Y. Wang and A.S. Nowick, *J. Electrochem. Soc.*, **128**, 55, (1981).
- D.Y Wang and A.S. Nowick, *J. Electrochem. Soc.*, **126**, 1166 (1979).
- W. Weppner, *J. Solid State Chem.*, **20**, 305 (1977)
- H.-D. Wiemhofer, *Ber. Bunsenges. Phys. Chem.*, **97**, 461 (1993).
- H.-D. Wiemhofer, *Solid State Ionics*, **75**, 167 (1995).
- A.J. Winnubst, A.H.A. Scharenborg and A.J. Burggraaf, *Solid State Ionics*, **14**, 319 (1984).
- E. Yeager and A. J. Salkind, *Techniques of Electrochemistry*, Vol 1, John Wiley & Sons , 177 (1973)
- D. Yuan and F.A. Kroger, *J. Electrochem. Soc.*, **116**, 594 (1969)
- W. Zipprich, H.-D. Wiemhofer, U. Vohrer, W. Gopel, *Ber. Bunsenges. Phys. Chem.*, **99**, 1406 (1995).

Biographical Note

The author was born in Calcutta, India on March 5, 1971. He moved to Stockholm, Sweden in 1973 together with his parents. He attended the Royal Institute of Technology where he received the degree of Master of Science in Metallurgy and Materials Technology in 1994. He entered the graduate school of the Massachusetts Institute of Technology in September, 1994.

The author is a member of Sigma Xi, the Electrochemical Society and the American Association for the Advancement of Science.